Cover Page



Universiteit Leiden



The handle http://hdl.handle.net/1887/26921 holds various files of this Leiden University dissertation

Author: Doan, Nhat Trung
Title: Quantitative analysis of human brain MR images at ultrahigh field strength
Issue Date: 2014-06-17

Quantitative Analysis of Human Brain MR Images at Ultrahigh Field Strength

Nhat Trung Doan

Quantitative Analysis of Human Brain MR Images at Ultrahigh Field Strength
Nhat Trung Doan

ISBN: 978-90-5335-870-2
Printed by Ridderprint BV

The covers show T_2^*-weighted magnitude image (back cover) and phase image (front cover) of an elderly subject acquired with a 7 Tesla MR scanner. Among other brain structures, the cerebral cortex is segmented and shown at the bottom right of the phase image.

© 2014 Nhat Trung Doan, Leiden, the Netherlands
All rights reserved. No part of this publication may be reproduced or transmitted in any form or by any means, electronic or mechanical, including photocopying, recording, or any information storage and retrieval system, without permission in writing from the copyright owner.

Quantitative Analysis of Human Brain MR Images at Ultrahigh Field Strength

Proefschrift

ter verkrijging van

de graad van Doctor aan de Universiteit Leiden,

op gezag van Rector Magnificus prof. mr. C.J.J.M. Stolker,

volgens besluit van het College voor Promoties

te verdedigen op dinsdag 17 juni 2014

klokke 11:15 uur

door

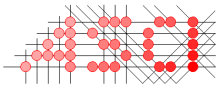
Nhat Trung Doan

geboren te Vietnam

in 1983

Promotiecommissie

Promotores:	Prof. dr. ir. B. P. F. Lelieveldt Prof. dr. M. A. van Buchem
Co-promotor:	Dr. ir. J. R. Milles
Overige leden:	Prof. dr. S. Ourselin *University College London, London* Dr. M. Barth *Radboud University Nijmegen, Nijmegen* Prof. dr. G. J. Blauw



This work was carried out in the ASCI graduate school.
ASCI dissertation series number 306.

This research was performed within the framework of CTMM, the Center for Translational Molecular Medicine (www.ctmm.nl), project LeARN (grant 02N-101).

Financial support for the publication of this thesis was kindly provided by:

- ASCI research school,
- Bontius Stichting inz. Doelfonds beeldverwerking,
- Library of the University of Leiden,
- Philips Healthcare, Best.

Contents

Contents **i**

1 Introduction **1**
1.1 Neurodegenerative diseases . . . 1
1.1.1 Alzheimer's disease . . . 1
1.1.2 Huntington's disease . . . 1
1.1.3 Magnetic resonance imaging as a biomarker . . . 1
1.2 T_2^*-weighted imaging at ultrahigh field strength . . . 2
1.2.1 T_2^*-weighted sequence . . . 2
1.2.2 MR phase contrast . . . 2
1.2.3 Ultrahigh field MR imaging . . . 3
1.3 Texture analysis . . . 3
1.3.1 Feature extraction . . . 4
1.3.2 Feature selection . . . 4
1.3.3 Texture analysis of brain MR images . . . 5
1.4 Problem statement . . . 5
1.5 Goals and contributions of the thesis . . . 6

2 Texture analysis of ultrahigh field T_2^*-weighted MR images of the brain: application to Huntington's disease **9**
2.1 Introduction . . . 11
2.2 Materials and methods . . . 12
2.2.1 Subjects . . . 12
2.2.2 MR acquisition . . . 12
2.2.3 Overall framework . . . 13
2.2.4 Image processing . . . 13
2.2.5 Texture computation . . . 14
2.2.6 Statistical testing . . . 16
2.3 Results . . . 17
2.3.1 Premanifest HD versus Controls . . . 17
2.3.2 Manifest HD versus Controls . . . 18
2.4 Discussion . . . 19
2.5 Acknowledgement . . . 21

3 Combined magnitude and phase-based segmentation of the cerebral cortex in 7T MR images of the elderly **23**

3.1 Introduction . . . 25
3.2 Materials and methods . . . 26
3.2.1 Segmentation algorithm . . . 26
3.2.2 Validation data . . . 31
3.2.3 Validation approach . . . 32
3.2.4 Validation measurements . . . 32
3.2.5 Robustness with regard to initial inner boundary positioning . . . 33
3.2.6 Accuracy of the segmentation method . . . 33
3.2.7 Added value of combining phase and magnitude . . . 33
3.2.8 Comparison with T_1-based segmentation . . . 34
3.3 Results . . . 34
3.3.1 Sensitivity to the initial inner boundary position . . . 34
3.3.2 Accuracy of the segmentation method . . . 34
3.3.3 Added value of combining phase and magnitude . . . 36
3.3.4 Comparison with T_1-based segmentation . . . 37
3.4 Discussion . . . 37
3.5 Acknowledgement . . . 39

4 Group-wise cortical feature analysis using high field T_2^*-weighted MR images highlights local differences between young and elderly healthy subjects 41
4.1 Introduction . . . 43
4.2 Materials and methods . . . 43
4.2.1 Subjects . . . 43
4.2.2 MR imaging . . . 44
4.2.3 Overview . . . 44
4.2.4 Pre-processing . . . 45
4.2.5 Cortex segmentation . . . 45
4.2.6 Registration . . . 45
4.2.7 Parcellation . . . 45
4.2.8 Computation of local cortical measures . . . 46
4.2.9 Statistical testing . . . 47
4.3 Results . . . 48
4.4 Discussion . . . 53
4.5 Conclusions . . . 55
4.6 Acknowledgements . . . 56

5 Cortical analysis using 7T MR phase images reveals regional differences between early and late onset Alzheimer's disease 57
5.1 Introduction . . . 59
5.2 Materials and methods . . . 59
5.2.1 Participants . . . 59
5.2.2 MR acquisition . . . 60
5.2.3 Image analysis . . . 60
5.2.4 Statistics . . . 61
5.3 Results . . . 62
5.4 Discussion . . . 66
5.5 Acknowledgement . . . 67

6 Deformation texture-based features for classification in Alzheimer's disease 69
6.1 Introduction . . . 71
6.2 Materials and methods . . . 71
6.2.1 Materials . . . 71
6.2.2 Methods . . . 72
6.3 Results and discussion . . . 74
6.3.1 Performance of the proposed approach . . . 77
6.3.2 Our approach *versus* Klein's approach and the hybrid approach . . . 77
6.3.3 Pairwise registration *versus* registration to a single template . . . 77
6.3.4 Global dissimilarity feature *versus* global and local textural features 77
6.3.5 *k*-NN classifier *versus* linear SVM . . . 78
6.4 Conclusions . . . 78

7 Summary and conclusion 79
7.1 Summary and conclusion . . . 79
7.2 Future work . . . 81

Samenvatting en conclusie 83

References 89

Acknowledgements 107

Curriculum Vitae 109

1

Introduction

1.1 Neurodegenerative diseases

Neurodegenerative diseases such as Alzheimer's, Huntington's and Parkinson's diseases are among the most devastating and costly diseases. They are characterized by a progressive and selective loss of anatomically and functionally related neuronal systems. Finding effective treatments and biomarkers for early detection of neurodegenerative diseases has been a longstanding research goal of neuro-scientists. In this section, we will briefly introduce Alzheimer's disease and Huntington's disease as well as the role of Magnetic Resonance Imaging (MRI) in the development of biomarkers for these diseases.

1.1.1 Alzheimer's disease

Alzheimer's disease (AD) is the most common cause of dementia [1]. It is characterized by impairment of memory and disturbances in reasoning, planning, language and perception. The disease prevalence was approximately 33.9 million people worldwide in 2011 and expected to triple in the next 40 years [2]. It is the sixth leading cause of death in the United States and the only one among the top 10 which currently cannot be prevented or cured [3]. Related neurobiological changes such as the progressive accumulation of the amyloid-β protein occur years before symptom onset [4] and the mean life expectancy after diagnosis is between 8 and 10 years [5].

1.1.2 Huntington's disease

Huntington's disease (HD) is a slowly progressive neurodegenerative disease. It is caused by a genetic defect on chromosome 4, with a disease onset at middle age and it is clinically characterized by symptoms of motor, behavioral and cognitive dysfunctioning [6]. The mean age of symptom onset is 40 years [7]. Currently no cure exists for this disease, although many therapeutic strategies have been investigated [8]. Besides therapeutic agents, much research focuses on the establishment of robust and sensitive biomarkers for the onset of the disease [9, 10]. This is essential to assess effectively potential therapeutic agents.

1.1.3 Magnetic resonance imaging as a biomarker

Despite advances in medicine and in our knowledge of the disease's biological processes, AD can only be diagnosed as "probable" using neuropsychological examinations, neu-

roimaging and patient clinical data with a sensitivity ranging from 70.9% to 87.3% and specificity from 44.3% to 70.8% [11]. The definitive diagnosis is still based on the combination of clinical features and post-mortem data [5, 12]. Due to the enormous expected increase of AD prevalence as well as the associated social cost, there is a need for biomarkers which can be used not only for early detection of the disease but also for monitoring disease progression and evaluating the effects of drug therapies.

In addition to non-imaging clinical biomarkers, research has focused on the use of MRI to provide in vivo imaging-based biomarkers. Structural MRI-based biomarkers for instance have been shown to reach an accuracy of 80% in predicting the conversion of mild cognitive impairment (MCI) to AD [5]. Even though encouraging, this performance is not sufficient and additional biomarkers need to be developed to increase the prediction accuracy. Another active aspect of MRI-based research in AD is the detection and quantification of abnormal iron accumulation in the brain. Studies have suggested that AD is associated with abnormal iron deposition within the cortex and basal ganglia [13, 14], possibly due to amyloid-β plaques associating with iron. T_2^*-weighted images can potentially be used for non-invasive investigation of both focal and diffuse iron deposition in the brain in vivo [15].

Regarding HD, MRI has been shown to be sensitive to the alteration of brain structures of individuals with premanifest or early HD [9, 16]. Multiple MRI-based studies have reported progressive atrophy in subcortical structures. Among others, it is well established that in the caudate nucleus and the putamen, atrophy occurs long before disease onset [17–19]. Early atrophy of the pallidum and accumbens nucleus has also been reported [20]. In addition to global volume reduction, localized and non-uniform patterns of atrophy were shown in subcortical structures using shape analysis [21]. Additionally, evidence of increased iron levels in the caudate and the putamen in manifest stage of the disease was also reported in an MRI study [22]. T_2^*-weighted imaging at ultrahigh field is increasingly used as a tool for assessing tissue magnetic susceptibility changes such as those caused by alternations in iron content.

1.2 T_2^*-weighted imaging at ultrahigh field strength

1.2.1 T_2^*-weighted sequence

T_2^*-weighted sequence is typically a gradient echo (GRE) sequence that is made more sensitive to T_2^* relaxation by tuning its parameters such as the repetition time (TR) and echo time (TE). In a GRE sequence, T_2^* relaxation refers to the decay of the transverse magnetization and is composed of two components: T_2 relaxation caused by the loss of phase coherence among spins and T_2' relaxation caused by local magnetic field inhomogeneities [23].

Data acquired with T_2^*-weighted sequence, like with other MR sequences, is a complex image from which the magnitude and phase components can be extracted. The T_2^*-weighted image is reconstructed using the magnitude component. The phase component, on the other hand, is usually discarded. However, it has been shown that the phase images offer sensitive indirect measures of changes in tissue magnetic susceptibility.

1.2.2 MR phase contrast

Local field inhomogeneity induced by tissue susceptibility produces local variations, resulting in decreased intensity on the magnitude images and increased phase shifts

[24]. This effect opens up possibilities for a new type of contrast based on the phase images. The phase component of the acquired complex data is bound to the interval of $[-\pi;\pi]$. Because of the inhomogeneity of the static field, its actual range is much larger, resulting in discontinuities or phase wraps. A common way to perform phase unwrapping is high-pass filtering in the *k*-space [25]. This method is based on the observation that the frequencies characterizing unwanted slow variations belong to lower frequency ranges than those characterizing anatomical information. It should be mentioned however that this filtering technique may lead a loss of anatomical information.

Image phase has been demonstrated as a rich source of information and useful for improved visualization of the brain structures. For instance, it has been shown that the phase images exhibit enhanced contrast within the basal ganglia [26] and hippocampus [27]. The relative contrast between cortical grey and subcortical white matter is more profound on phase images as compared to the magnitude images [28, 29]. Furthermore, phase shift has been demonstrated to vary linearly with iron concentration in regions with high iron content [30]. Image phase can be used as an indirect measure of iron in the brain.

1.2.3 Ultrahigh field MR imaging

Since the introduction of the first MRI machine in the early 70s, MRI has received much attention and it has undergone vast technological developments. Continuous effort has been made to develop new scanners, particularly to increase the magnetic field strength. An increase in field strength will lead to an increase in spatial image resolution, signal to noise ratio, contrast to noise ratio and sensitivity to tissue susceptibility [31], from which several clinical applications can benefit. Besides potential improvements in image quality, a number of challenges are faced at ultrahigh field such as an increase of inhomogeneity, geometric distortion, tissue heating, and signal loss due to intravoxel dephasing [31, 32]. Currently, while clinical scanners operate at a standard static field of 1.5 or 3 Tesla (T), an increasing number of human scanners operating at ultrahigh field strengths (7T or 9.4T) are used in clinical research.

Since susceptibility-induced changes in the magnetic field scale linearly with field strength, T_2^*-weighted images show a higher sensitivity to changes in substances such as iron and myelin at higher field strengths [26]. Image processing techniques need to be developed to enable quantitative studies making use of the information offered in ultrahigh field T_2^*-weighted magnitude and phase images. To this end, texture analysis could be a useful tool as it could allow the extraction of several relevant textural features from those images.

1.3 Texture analysis

Image texture refers to a group of image properties that describe spatial arrangements of visual patterns and relates to the intuitive notions such as contrast, coarseness and smoothness [33]. Textures can be recognized qualitatively by means of visual observation. Nevertheless, the ability of our vision system in detecting and discriminating complex textures is limited [34]. Texture analysis allows the mathematical description of image textures that are both perceptible and imperceptible to human eyes. Texture analysis techniques initially were proposed for 2D images and subsequently extended for 3D datasets. A texture analysis framework is often composed of the following steps: image pre-processing, feature extraction, feature selection, statistical comparison or classification

[35]. Several approaches have been proposed in the literature for feature extraction and selection.

1.3.1 Feature extraction

In this section, we will briefly review transform-based and statistical approaches, which are among the most commonly used approaches in texture analysis of neuro-MR images [35].

In transform-based approaches, image textural features are described as parameters obtained from signal processing transformations such as Fourier, Wavelet, Gabor and Stockwell transforms. These approaches represent the image in a new space whose co-ordinate system, e.g. frequency and size, has an interpretation closely related to image textural characteristics [36]. Fourier transform-based approaches provide textural features as measurements in a spatial frequency spectrum. A disadvantage of this approach is that it cannot reflect any spatial localization in the frequency domain [35]. The Gabor transform, also referred to as short-time Fourier transform, allows the quantification of changes in texture in different parts of the image. Textural features extracted using Gabor transform are invariant with respect to illumination, rotation, and translation [37]. The Wavelet transform provides a multi-scale representation of the image [38]. The energy of Haar Wavelet sub-bands, for instance, can be calculated as a textural feature [39]. The Stockwell transform provides a unique time-frequency representation of the image [40]. Since its feature is a combination of the localization feature of the Gabor transform and the multi-scale feature of the Wavelet transform, this transform enables capturing subtle textural changes in the image.

Among other approaches, statistical approaches, particularly Gray-Level Co-occurrence Matrix (GLCM) approach [41], have been widely used in MRI studies because of its ability to characterize image properties based on voxel spatial correspondence. A GLCM tabulates the frequency of every pair of image intensity over the whole image or ROI at a given spatial offset. Based on this approach, 2D GLCMs or 3D GLCMs can be computed. It has been shown that 3D GLCM yields features with higher discriminative power compared to 2D GLCM [42]. Additionally, textural features derived from GLCMs are superior compared to features of other categories regarding their ability to distinguish different patterns for datasets that are heterogeneous to imaging parameters, including spatial resolution [43]. The run-length matrix has also been used in the literature. This approach allows one to evaluate the coarseness of a texture in a predetermined direction. A run length matrix is constructed by tabulating the number of gray-level runs for each gray level at the given direction. The performance of this approach, compared to the GLCM-based approach, is subject to some debate [35].

1.3.2 Feature selection

In texture analysis, a large number of features are often extracted. This results in redundant or correlated features. The selection of relevant features is needed to reduce the dimensionality. A wide range of techniques has been used in the literature for feature selection. For example, scatters plots and linear regression can be used to assess the relation between feature pairs and thereby identify redundant features. Principle Component Analysis (PCA) was applied to convert a set of possibly correlated features into an equal or smaller set of uncorrelated features based on eigenvalue decomposition [44–47]. Useful features were selected based on their sensitivity and specificity using ROC

analysis [48]. Sequential forward feature selection method based on the Mahalanobis distance was applied in an iterative framework. The selection procedure iterated until none of the remaining features would significantly increase the Mahalabonis distance [49]. Linear discriminant analysis was applied in conjunction with augmented variance ratio for feature ranking [50]. In [51], a pre-selection step was introduced for improving the effectiveness in searching the feature subsets and ROC analysis was applied characterize the performance of individual features and feature subsets. In [52], a subset of features derived from different approaches was selected based on greatest difference between different tissue types.

1.3.3 Texture analysis of brain MR images

Texture analysis has been shown to be a useful tool in numerous MR-based studies of the human brain. Texture analysis can be carried out on the entire brain or a region of interest that is manually delineated or on a structure automatically segmented. It has been applied to different structures of the brain in the context of several neuronal diseases. For instance, 3D textures were extracted from T_1-weighted images of the hippocampus and entorhinal cortex for the differentiation between AD patients and normal controls. The textural features used were extracted based on image histogram, gradient, GLCM, and run-length matrix [53]. Textural features derived using the GLCM approach was used in combination with computational models for automated detection of focal cortical dysplasia lesion on T_1-weighted images [54]. 3D textural features computed based on image histogram, GLCM and run-length matrix were used to discriminate benign, malignant and metastatic brain tissues on T_1 post contrast MR images [55]. Features computed from GLCM and run-length matrix were used for the discrimination of multiple sclerosis from cerebral microangiopathy lesions [56]. GLCM-based features extracted from postcontrast T_1-weighted images were used for the prediction of hemorrhagic transformation in acute ischemic stroke. Gradient magnitude and entropy were computed from T_1 MR images for quantifying changes in the temporopolar cortex and white mater in temporal lobe epilepsy [57]. Wavelet-based textural features, the mean and standard deviation of FLAIR images of the hippocampus were investigated in a study of mesial temporal lobe epilepsy [58]. Textural features of T2 MR images extracted using the polar Stockwell transform was demonstrated as a sensitive measure of tissue injury and recovery resulting from acute inflammatory lesions in multiple sclerosis [59]. GLCM-based texture analysis of high resolution MR images showed the ability to discriminate between febrile and afebrile initial precipitating injury in mesial temporal sclerosis [60]. The added value of texture analysis in disease monitoring has also been demonstrated in studies of neurodegenerative diseases such as Alzheimer's disease [33, 49, 53] and Parkinson's disease [61].

1.4 Problem statement

In neuro-imaging, texture analysis has been widely applied to T_1-weighted MR images. Texture analysis of T_2^*-weighted images however has not yet been explored. The ability to quantitatively capture macro and micro changes in the form of texture makes texture analysis a potential tool for investigating neuro-tissue alterations such as those related to tissue magnetic susceptibility as reflected in T_2^*-weighted images. The main part of this thesis is inspired by the need to develop methods for quantitative analysis, including texture analysis, of T_2^*-weighted images acquired at 7T.

Additionally, as a potential application, texture analysis can be employed to explore the

informational content of the deformation field obtained from non-rigid image registration. The Jacobian determinant map of the deformation field can be used to characterize local volumetric changes. In AD, studies based on volumetric and shape analysis have reported abnormalities in multiple structures such as the hippocampus, cortex [62], thalamus, putamen [63], amygdala [64] and ventricle [65]. Several techniques have been developed for deformation-based morphometry studies of brain changes in AD [45, 66, 67]. However, the textural aspects of the deformation field have not been investigated. We hypothesize that the deformation field contains information about the overall patterns of volumetric changes in the entire brain and this information can be extracted and incorporated in a classification framework by means of texture analysis.

1.5 Goals and contributions of the thesis

The primary goal of this thesis is to develop methodologies for quantitative analysis of human brain MR images at ultrahigh field strength. In particular, we aim to develop methods for:

- Detection of between-group textural differences in 7T T_2^*-weighted images of subcortical structures.
- Segmentation and quantification of local changes in the cerebral cortex in 7T T_2^*-weighted images.

In addition, we also aim to investigate the possibility to extract and use the textural information from whole brain deformation field for classification purpose.

The contributions of the thesis are summarized as following:

Chapter 2: approaches for the extraction and usage of quantitative information from T_2^*-weighted images at ultrahigh field have not been fully explored. We propose a quantitative framework to explore textural information available on T_2^*-weighted images acquired at 7T based on a second-order texture analysis approach. We apply the proposed framework to study textural differences in subcortical structures between premanifest HD, manifest HD and controls. Our results provide the first evidence of textural heterogeneity of subcortical structures in HD.

Chapter 3: accurate quantitative analysis of the cerebral cortex using T_2^*-weighted images requires accurate depiction of the structure from these images. Manual segmentation is tedious and subject to inter-subject variability. Segmentation based on T_1-weighted images suffers from the decreased GM/WM contrast due to aging and pathology as well as global and local inaccuracy caused by acquisition artefacts between T_1 and T_2^* data. In this chapter, we describe a new method that performs cortical segmentation directly on T_2^*-weighted images using the combined magnitude and phase information. The segmentations obtained using the method are evaluated against manual segmentations and T_1-based segmentations on a group of elderly subjects. The results show that the proposed method is an accurate and robust approach for cortex segmentation in datasets presenting low GM/WM contrast.

Chapter 4: T_2^*-weighted segmentation of the cortex once obtained enables subsequent automatic analysis steps. We develop a framework for group-wise analysis of the cortical features based on the segmented cortex and an anatomical atlas. The proposed framework allows for computing GM/WM contrast and cortical profiles at local cortical regions on T_2^*-weighted magnitude and phase images, and perform group-wise comparison using the

computed measures. Differences in terms of local GM/WM contrast are evaluated using the Mann-Whitney U-test. By using a local comparison of the regional cortical profile, differences at each cortical depth can be highlighted. We demonstrate the application of the framework using data of young and elderly healthy subjects.

Chapter 5: Previous studies indicate that early onset AD (EOAD) patients have different AD pathology compared to patients with late onset AD (LOAD). In this chapter, we explore regional iron related differences, possibly indicative for AD pathology, in the cerebral cortex between EOAD and LOAD patients using 7T MR phase images. Based on the method presented in chapter 4, we assess the differences between these groups of patients in terms of lobar phase shift, cortical phase contrast and phase profile at local cortical regions.

Chapter 6: we develop a novel method for exploiting the information contained in the Jacobian determinant map of the deformation field. In particular, we study the textural aspects of the Jacobian determinant map. By means of texture analysis, the developed method captures the overall patterns of the Jacobian determinant map over the entire brain, thereby incorporating information about volumetric changes of all structures in the brain in classification of AD subjects. Classification results using support vector machine in a bootstrapping procedure demonstrate the potential of texture analysis on entire brain Jacobian determinant map for diagnosis of AD subjects.

In **Chapter 7**, we present a summary and conclusion of the thesis.

2

Texture analysis of ultrahigh field T_2^*-weighted MR images of the brain: application to Huntington's disease

This chapter was adapted from:

N. T. Doan, S. J. A. van den Bogaard, E. M. Dumas, A. G. Webb, M. A. van Buchem, R. A. C. Roos, J. van der Grond, J. H. C. Reiber, and J. Milles, "Texture analysis of ultrahigh field T_2^*-weighted MR images of the brain: application to Huntington's disease," *Journal of Magnetic Resonance Imaging*, vol. 39, no. 3, pp. 633–640, 2014.

Abstract

Purpose: To develop a framework for quantitative detection of between-group textural differences in ultrahigh field T_2^*-weighted MR images of the brain.

Materials and methods: MR images were acquired using a three-dimensional (3D) T_2^*-weighted gradient echo sequence on a 7 Tesla MRI system. The phase images were high-pass filtered to remove phase wraps. Thirteen textural features were computed for both the magnitude and phase images of a region of interest based on 3D Gray-Level Co-occurrence Matrix, and subsequently evaluated to detect between-group differences using a Mann-Whitney U-test. We applied the framework to study textural differences in subcortical structures between premanifest Huntington's disease (HD), manifest HD patients, and controls.

Results: In premanifest HD, four phase-based features showed a difference in the caudate nucleus. In manifest HD, 7 magnitude-based features showed a difference in the pallidum, 6 phase-based features in the caudate nucleus, and 10 phase-based features in the putamen. After multiple comparison correction, significant differences were shown in the putamen in manifest HD by two phase-based features (both adjusted p values = 0.04).

Conclusion: This study provides the first evidence of textural heterogeneity of subcortical structures in HD. Texture analysis of ultrahigh field T_2^*-weighted MR images can be useful for noninvasive monitoring of neurodegenerative diseases.

2.1 Introduction

Recent technological developments of clinical ultrahigh field MR scanners have enabled the acquisition of data with increased image resolution, signal-to-noise ratio and contrast-to-noise ratio [31]. In particular, T_2^*-weighted imaging has recently received much attention due to its capability to characterize tissue magnetic susceptibility [26, 68, 69] and phase images showing an increased sensitivity to small differences in tissue susceptibility with higher field strengths [26]. T_2^*-weighted images have been used in quantitative studies of the brain at lower fields, e.g. as an indirect means to study iron in subcortical structures of patients with multiple sclerosis and clinically isolated syndromes [70, 71]). With ultrahigh field MRI, T_2^*-weighted images have been examined qualitatively for improved visualization of anatomical structures such as the cerebral cortex [72] and the hippocampus [27]. However, approaches for the extraction and utilization of quantitative information from these images have not yet been fully explored. In phase-based studies [70, 71, 73], the mean phase value of a region of interest (ROI) is often used. This measure does not consider any spatial relationships between phase voxels and as a result does not reflect local spatial differences. Apart from global phase shifts, additional local changes among image voxels such as focal or distributed alterations within the ROI cannot be captured by the mean phase value. This limitation can be overcome by means of texture analysis.

Image texture describes the spatial arrangement of visual patterns that relate to intuitive notions such as coarseness, contrast and smoothness. Texture analysis techniques allow one to mathematically quantify the textural aspect of images independently of the way they are perceived by the human eye. In the literature, several texture analysis approaches have been proposed such as transform-based approaches, signal processing approaches and statistical approaches [35]. Gray-Level Co-occurrence Matrix (GLCM) [41] is one of the most widely used approaches because of its ability to characterize image properties based on voxel spatial correspondence. Based on this approach, 3D GLCMs, which yield features with higher discriminative power compared to 2D GLCMs [42], can be computed and subsequently used to derive second-order textural features. The added value of texture analysis in disease monitoring has been demonstrated in MR-based studies of neurodegenerative diseases such as Alzheimer's disease [49] and Parkinson's disease [61]. This tool can potentially be used to quantitatively study changes reflected on ultrahigh field T_2^*-weighted images.

Huntington's disease (HD) is a slowly progressive neurodegenerative disease clinically characterized by symptoms of motor, behavioral, psychiatric and cognitive dysfunction [6]. Global and localized atrophy in subcortical structures has been reported in HD [18, 21]. Additionally, studies have shown profound cellular deterioration in the putamen and caudate nucleus based on histological data [74–76] and increased iron accumulation in the same structures using MRI [22]. Abnormal iron levels in the basal ganglia have been demonstrated both post mortem [77] and in vivo using T_2 relaxometry [78–80]. We hypothesized that indications of change at tissue level in subcortical structures in HD, possibly related to iron accumulation, can be captured using texture analysis of ultrahigh field T_2^*-weighted images.

In this work, we propose a quantitative framework composed of 7 Tesla (T) T_2^*-weighted imaging and the GLCM texture analysis approach which allows one to capture between-group differences. We apply the proposed framework to study textural hetero-

TABLE 2.1: Subject characteristics.

	Premanifest HD	Manifest HD	Controls
Age	43.7 ± 9.9	51.5 ± 12.2	48.1 ± 1.3
CAG repeat	43.7 ± 3	43.8 ± 3.2	n/e
Gender (male/female)	3/4	5/3	3/2

n/e = not examined

geneity in subcortical structures of subjects with premanifest and manifest HD and healthy controls. Furthermore, by means of texture analysis, we aim to study the quantitative values of ultrahigh field T_2^*-weighted images.

2.2 Materials and methods

2.2.1 Subjects

Twenty participants were recruited from our institution's neurology outpatient clinic, of which 7 were premanifest HD gene carriers, 8 manifest HD patients and 5 controls. Inclusion criteria for the premanifest HD consisted of a positive genetic test for a CAG-repeat expansion of > 39 in the Htt-gene, an absence of motor abnormalities defined as a score of ≤ 5 on the Unified Huntington's Disease Rating Scale (UHDRS), total motor score (TMS) and a diagnostic confidence level of 0 or 1 on the UHDRS. Inclusion criteria for manifest HD consisted of a positive genetic test for a CAG-repeat expansion of > 39 in the Htt-gene, a presence of motor abnormalities defined as a score of > 5 on the UHDRS-TMS and a diagnostic confidence level of 4 on the UHDRS. Healthy gene negative family members or spouses were recruited as controls. Exclusion criteria for all participants consisted of significant (neurological) comorbidity, claustrophobia and MRI incompatibility. The study was approved by the Medical Ethical Committee. All participants gave written informed consent. Characteristics of the participants are presented in Table 2.1.

2.2.2 MR acquisition

The participants underwent MRI scanning on a 3T and a 7T Philips whole body systems (Philips Healthcare, Best, the Netherlands) within 24 h. T_1-weighted images were acquired on both scanners and a T_2^*-weighted imaging sequence was performed on the 7T scanner. Texture analysis was performed on the 7T T_2^*-weighted images. The 3T T_1-weighted images were used for automated segmentation of subcortical structures while the 7T T_1-weighted images were only used for registration purpose. The following scan parameters were applied:

3T T_1-weighted MRI

T_1-weighted image volumes were acquired using a 3D gradient echo acquisition sequence with the following imaging parameters: repetition time (TR) = 7.7 ms, echo time (TE) = 3.5 ms, flip angle (FA) = 8^o, field-of-view (FOV) = 240 x 224 x 224 mm^3, 164 sagittal slices to cover the entire brain, voxel size 1.1 x 1.0 x 1.0 mm^3.

7T T_1-weighted MRI

A 3D gradient echo sequence was applied with the following parameters: TR = 18 ms, TE = 8.9 ms, FA = 8^o, FOV 210 x 169 x 120 mm^3, voxel size 0.3 x 0.3 x 2.0 mm^3.

7T T_2^*-weighted MRI

A high-resolution 3D heavily T_2^*-weighted gradient echo sequence was used with the following parameters: TR = 24 ms, TE = 15 ms, FA = 45°, FOV 220 x 182 x 142 mm^3, voxel size 0.25 x 0.25 x 0.5 mm^3.

Examples of the acquired images are shown in Figure 2.1.

2.2.3 Overall framework

Image analysis was performed as follows. First, preprocessing included intensity inhomogeneity correction for the magnitude images, phase unwrapping for the phase images, and segmentation of the subcortical structures using the 3T T_1-weighted images. After preprocessing, rigid registration was applied to align all images of each subject to the subject 3T T_1-weighted space. Subcortical segmentations were performed using the 3T T_1-weighted images and the segmentation masks were then used to identify subcortical structures in the 7T T_2^*-weighted magnitude and phase images. Subsequently, thirteen Haralick features [41] were computed for both 7T T_2^*-weighted magnitude and phase images of each structure based on a GLCM. A nonparametric statistical testing was then performed on each Haralick feature to compare the premanifest and manifest groups with a control group.

2.2.4 Image processing

2.2.4.1 Intensity inhomogeneity correction

Intensity non-uniformity is a common artifact in MR imaging characterized by anatomically independent intensity variation throughout the data. Correction for this artifact is crucial as it degrades the performance of quantitative MRI analysis [81]. In this study, we applied the N3 algorithm [82] for the correction of the 7T T_1-weighted and 7T T_2^*-weighted magnitude images using its implementation in MIPAV software [83].

2.2.4.2 Phase unwrapping

The phase of each pixel in the MR image, reconstructed on the scanner, is bound to the interval of $[-\pi, \pi]$. However, its actual range is much larger due to the intrinsic inhomogeneity of the magnetic field, resulting in phase wraps in the images. In this study, phase wrap removal, also referred to as phase unwrapping, was performed based on high-pass filtering in the *k*-space as implemented in Wang et al. [25].

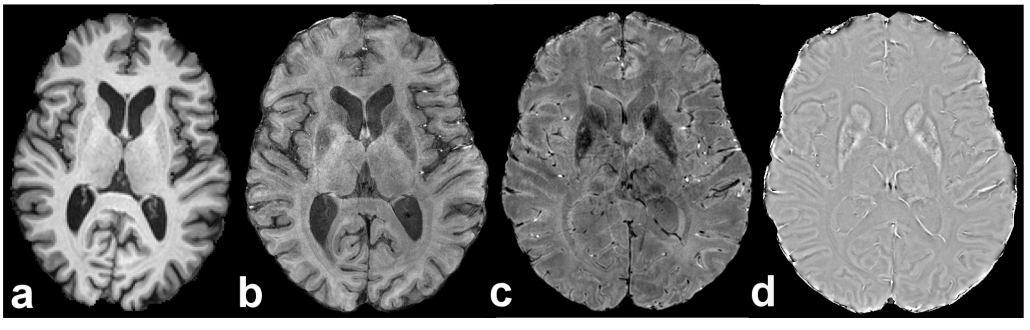


FIGURE 2.1: Examples of 3T T_1-weighted magnitude (a), 7T T_1-weighted magnitude (b), 7T T_2^*-weighted magnitude (c), and 7T T_2^*-weighted (unwrapped) phase (d) images.

2.2.4.3 Segmentation of subcortical structures

Texture analysis on subcortical nuclei requires segmentation of these structures. To obtain segmentation of the subcortical nuclei, we applied FIRST [84], part of the FSL package, on the 3T T_1-weighted images. The software has also been successfully applied in recent HD studies [20–22]. The resulting subcortical masks were used to segment subcortical structures on the 7T T_2^*-weighted magnitude and phase images. In the present work, we studied the following structures: amygdala, caudate nucleus, hippocampus, pallidum, putamen and thalamus.

2.2.4.4 Registration

Subcortical segmentation on 7T T_2^*-weighted magnitude and phase images using the 3T T_1-based subcortical masks required registration to transform 7T T_2^*-weighted images to the 3T T_1-weighted space. Since the accuracy of direct registration between 7T T_2^*-weighted and 3T T_1-weighted images suffered from the differences in type of MR sequences and field strengths, the 7T T_1-weighted images were used in an intermediate step during the registration to improve the overall performance of registration. The registration was done using the *elastix* registration package [85] in two steps: rigid body registration of 7T T_2^*-weighted images to 7T T_1-weighted images using mutual information as the similarity measure and a B-spline interpolator, followed by rigid body registration of 7T T_1-weighted images to 3T T_1-weighted images using correlation ratio and a B-spline interpolator.

After registration, since the computation of 3D textural features in this study required isotropic data, all subcortical segmentations were resampled from 1.1 x 1.0 x 1.0 mm^3 to 1.0 x 1.0 x 1.0 mm^3.

2.2.5 Texture computation

2.2.5.1 3D Gray-Level Co-occurrence Matrix

In this study, the textural features were computed based on 3D Gray-Level Co-occurrence Matrix (GLCM). A GLCM $\boldsymbol{M}$ of an image $\boldsymbol{I}$ represents how often every combination of gray scale values occurs in the image at a given spatial offset. The matrix is constructed by systematically searching the whole image and tabulating the frequency of different gray level combinations. Each entry $M(i,j)$ of the matrix is equal to the number of times voxel $I(x,y,z)$, with value i, and voxel $I\left(x+\Delta_x, y+\Delta_y, z+\Delta_z\right)$, with value j, occur in the image. $I(x,y,z)$ and $I\left(x+\Delta_x, y+\Delta_y, z+\Delta_z\right)$ are termed neighboring voxels. The coordinate of the neighbor of a voxel being considered is identified by a displacement vector (or offset) $\vec{\boldsymbol{\Delta}}\left(\Delta_x, \Delta_y, \Delta_z\right)$. This displacement vector is composed of the distance between the voxels and the direction in which they are searched for.

Mathematically, $M(i,j)$ is computed as:

$$M(i,j) = \sum_{x=1}^{P}\sum_{y=1}^{Q}\sum_{z=1}^{L}\begin{cases}1, & \text{if } I(x,y,z)=i \text{ and } I(x+\Delta_x, y+\Delta_y, z+\Delta_z)=j\\ 0, & \text{otherwise}\end{cases} \tag{2.1}$$

where P, Q, and L are the image dimensions. To avoid obtaining a sparse GLCM, image intensity is often quantized to a smaller range of N gray levels. In this study, we used a global intensity quantization scheme to preserve the relative difference in dynamic range between subjects. For each structure of interest, the global maximum intensity I_{max} and global minimum intensity I_{min} over all studied subjects were computed and the quantization step defined as $q = \frac{I_{max}-I_{min}}{N-1}$. Quantization of the data pertaining to the

structure of interest was performed for every subject using the resulting global dynamic range and quantization step. All GLCMs were square matrices of dimension N computed from the quantized images. This global scheme has been reported to be optimal compared to a local scheme that scales each individual dynamic range to the same range of $[1;N]$ [42]. In this work, we chose a commonly used value of N of 32 gray levels [35] for intensity quantization. Prior to this intensity quantization step, the dynamic range of the whole-brain magnitude images was scaled to the same range of $[0;1023]$ (10 bits) for intensity normalization.

Since there is no evidence for pathological differences between the different hemispheres in HD, we did not investigate the left and right sub-structures separately, but rather combined them together. The GLCM for the whole structure was computed as follows. Prior to the computation of GLCM, the 3D volume of each structure was oriented such that it was symmetrical with respect to the y = 0 plane. At a given offset specified by the displacement vector of $(\Delta_x, \Delta_y, \Delta_z)$, one GLCM was computed for the left structure using this vector and another GLCM was computed for the right structure using a modified version of the displacement vector $(\Delta_x, -\Delta_y, \Delta_z)$. The sum of the two GLCMs was the GLCM computed for the whole structure.

In this 3D computation of GLCM, we considered 13 directions and a distance of 1 voxel. For each structure, one GLCM was computed for each direction, resulting in 13 GLCMs. These 13 GLCMs were then averaged to obtain a non-directional GLCM.

2.2.5.2 Haralick features

Thirteen Haralick features [41] were derived from each GLCM after its normalization. One GLCM was computed for each structure, resulting in 13 features being computed for each structure. These features included: angular second moment (f_1), contrast (f_2), correlation (f_3), sum of squares (f_4), inverse difference moment (f_5), sum average (f_6), sum variance (f_7), sum entropy (f_8), entropy (f_9), difference variance (f_{10}), difference entropy (f_{11}), information measure of correlation 1 (f_{12}) and information measure of correlation 2 (f_{13}). Some of the features intuitively represent image texture properties. Figure 2.2 presents an illustrative example which shows the values of 4 Haralick features computed from simple synthetic textures. *Angular second moment* measures the uniformity of the image. A higher value of angular second moment indicates less variation in the image intensity. Its value ranges from 0 (image D with randomly-distributed intensity) to 1 (image A with constant intensity). *Contrast* quantifies the local variations in the image with a higher value of contrast indicating higher intensity differences between a voxel and its neighbors over the whole image. For example, image C shows very sharp local black-white transitions which are represented by a very high value of contrast of this texture compared to other textures which show less local intensity variation. *Correlation*, ranging from -1 to 1, measures linear dependencies of image gray-levels. Image C for example shows a high linear dependence which is not present in image D. Such differences are captured by the difference in the computed values of correlation feature (note that the correlation of a constant image (image A) is not defined). *Entropy* is a measure of disorder or randomness. It takes higher values for more complex images, for instance, image B and D have higher entropy compared to image A and C. For details about the formulae used to compute each Haralick feature, we refer the readers to the original reference in the field [41].

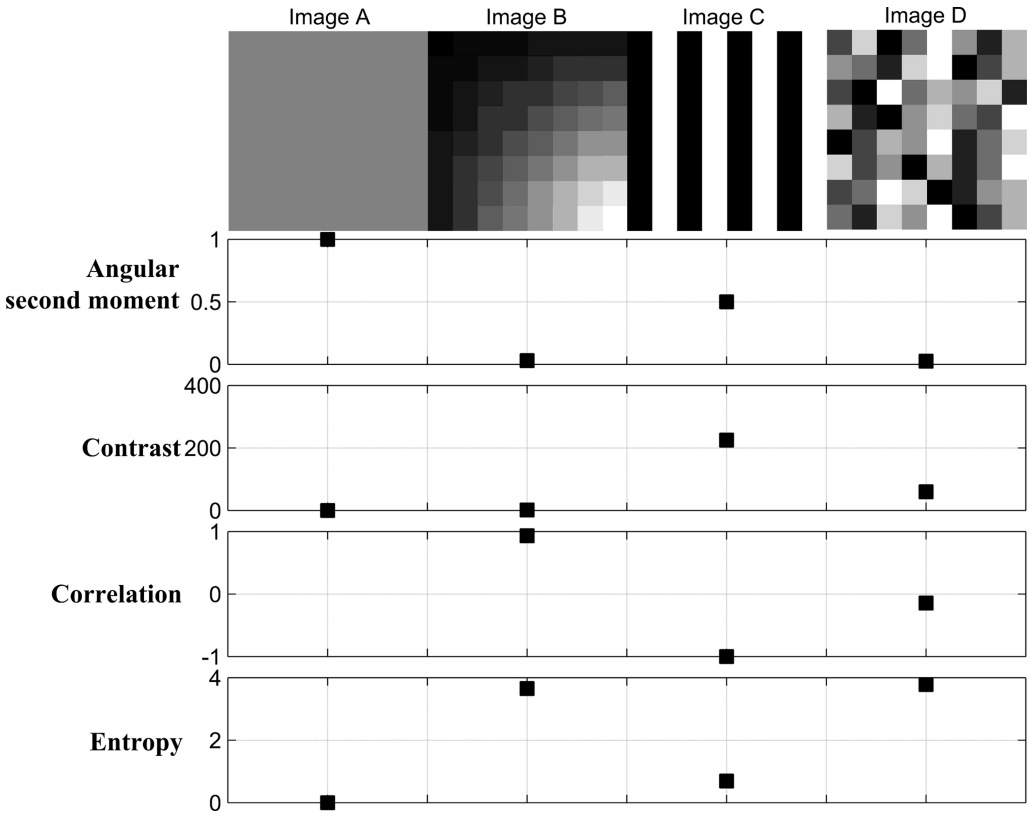


FIGURE 2.2: Illustrative example of 4 Haralick features (angular second moment, contrast, correlation and entropy) computed from synthetic images. Each image (**A-D**) presents a simple texture. A GLCM was computed for each image using a displacement vector of $\pm(0,1)$ pixel and a quantization level N of 16.

2.2.6 Statistical testing

After feature computation, a Mann-Whitney U-test [86] was applied in the following two comparisons: premanifest HD versus controls, and manifest HD versus controls. The Mann-Whitney U-test, a non-parametric test which makes no assumption about normal distribution of the data, was used to determine whether the mean of two groups are significantly different from each other. In each of the aforementioned comparisons, for each structure, 13 Mann-Whitney U-tests were carried out for the 13 Haralick features. Subsequently, to check whether the differences shown by the Mann-Whitney U-tests were significant, we performed a correction for multiple comparisons as follows. The Bonferroni procedure was applied to adjust the resulting 13 p values. The adjusted p values were then compared to the significance level to accept or reject the null hypothesis of equal means between groups. Both feature computation and statistical tests, with significance level of 0.05, were carried out in Matlab (Mathworks, Natick, MA, version 7.13).

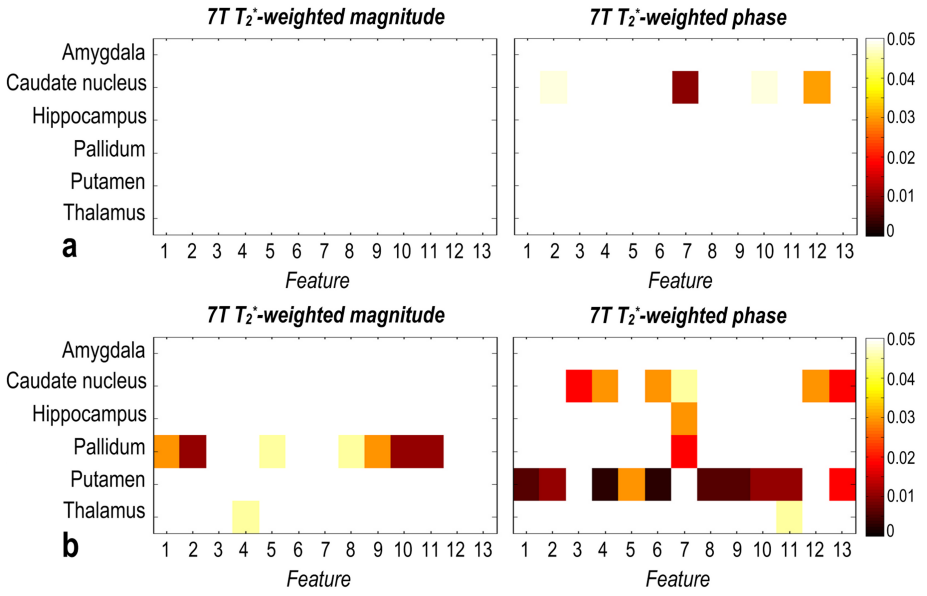


FIGURE 2.3: p values of the Mann-Whitney U-tests before correction for multiple comparisons: premanifest HD versus controls (a); manifest HD versus controls (b). In each case, the results of the tests performed for each studied structure using either 7T T_2^*-weighted magnitude features or 7T T_2^*-weighted phase features are presented. p values smaller or equal to 0.05 were color-coded such that the darker the color, the smaller the value.

2.3 Results

This section presents the results of the statistical tests performed to compare the premanifest HD group and manifest HD group with the control group. For each subcortical structure, a total of 26 features were computed from 7T T_2^*-weighted data, 13 using the magnitude images and 13 using the phase images. In each comparison, the results obtained before and after correcting the p values for 13 features are presented. For the differences revealed by the Mann-Whitney U-tests before the correction, Figure 2.3 presents the resulting p values and Table 2.2 provides a detailed list of the discriminative features. After correction for multiple comparisons, statistically significant differences were found in the putamen between manifest HD and controls. Further details are presented as follows.

2.3.1 Premanifest HD versus Controls

When evaluating the discriminative power of each feature individually, no correction for multiple comparisons was applied. The magnitude-based features did not show statistically significant differences. Four phase-based features including the sum variance, information measure of correlation 1, contrast, and difference variance showed differences in the caudate nucleus (p = 0.01, 0.03, 0.048, and 0.048 respectively). When a more stringent significance level was applied using the Bonferroni procedure, none of the differences shown by the phase-based features were significant.

TABLE 2.2: List of features showing differences when comparing premanifest and manifest HD groups with the control group. The listed features were found based on the p values obtained before the correction for multiple comparisons. Asterisks indicate features that showed significant difference after correction for multiple comparisons.

	Comparison	Structure	Discriminative feature
T_2^*-weighted magnitude	Manifest HD vs. Controls	Pallidum	Angular second moment (f_1)
		Pallidum	Contrast (f_2)
		Pallidum	Inverse difference moment (f_5)
		Pallidum	Sum entropy (f_8)
		Pallidum	Entropy (f_9)
		Pallidum	Difference variance (f_{10})
		Pallidum	Difference entropy (f_{11})
		Thalamus	Sum of squares (f_4)
T_2^*-weighted phase	Premanifest HD vs. Controls	Caudate nucleus	Contrast (f_2)
		Caudate nucleus	Sum variance (f_7)
		Caudate nucleus	Difference variance (f_{10})
		Caudate nucleus	Information measure of correlation 1 (f_{12})
	Manifest HD vs. Controls	Caudate nucleus	Correlation (f_3)
		Caudate nucleus	Sum of squares (f_4)
		Caudate nucleus	Sum average (f_6)
		Caudate nucleus	Sum variance (f_7)
		Caudate nucleus	Information measure of correlation 1 (f_{12})
		Caudate nucleus	Information measure of correlation 2 (f_{13})
		Hippocampus	Sum variance (f_7)
		Pallidum	Sum variance (f_7)
		Putamen	Angular second moment (f_1)
		Putamen	Contrast (f_2)
		Putamen	Sum of squares (f_4)*
		Putamen	Inverse difference moment (f_5)
		Putamen	Sum average (f_6)*
		Putamen	Sum entropy (f_8)
		Putamen	Entropy (f_9)
		Putamen	Difference variance (f_{10})
		Putamen	Difference entropy (f_{11})
		Putamen	Information measure of correlation 2 (f_{13})
		Thalamus	Difference entropy (f_{11})

2.3.2 Manifest HD versus Controls

As illustrated in Figure 2.3, before correction for multiple comparisons, 7 of 13 T_2^*-weighted magnitude-based features showed a difference in the pallidum ($0.011 \leq p \leq 0.045$). Six of 13 and 10 of 13 T_2^*-weighted phase-based features showed a difference in the caudate nucleus ($0.019 \leq p \leq 0.045$) and the putamen ($0.003 \leq p \leq 0.03$), respectively. The magnitude-based features are mainly discriminative in the pallidum, whereas the phase-based features are mainly discriminative in the caudate nucleus and the putamen. In addition, one magnitude-based feature and one phase-based feature showed a difference in the thalamus (sum of squares with $p = 0.045$ for magnitude and difference entropy with $p = 0.045$ for phase). The sum variance computed from the phase images showed a difference in the hippocampus ($p = 0.03$) and the pallidum ($p = 0.019$). No features showed differences in the amygdala. After correction for multiple comparisons, significant differences were shown in the putamen by two phase-based features (sum of squares and sum average, both with adjusted p value of 0.04).

2.4 Discussion

We have presented a novel framework for quantitative detection of textural heterogeneity in subcortical structures and between-group differences using 7T T_2^*-weighted images and a second-order texture analysis approach. We evaluated the framework on in vivo data of premanifest HD gene carriers, manifest HD patients and control subjects. The results provide the first evidence of textural heterogeneity of subcortical structures in HD. Importantly, the regional specific textural differences are in line with structural deficits previously reported in vivo and ex vivo in both premanifest and manifest HD [16, 87].

In the presented framework, several preprocessing steps were performed prior to textural computation. Two of them, inhomogeneity correction and phase unwrapping, were a prerequisite to further analysis and performed on different data, the former on 7T magnitude images and the latter on phase images. Two other steps were due to the need to identify regions of interest on 7T T_2^*-weighted images: subcortical structure segmentation on 3T T_1-weighted images and registration from 7T T_2^*-weighted space to 3T space. Textural computation itself involved two steps, GLCM computation and derivation of Haralick features, which are standard steps in GLCM-based texture analysis. The only steps that may affect texture analysis are the registration of T_2^*-weighted images to 3T space and resampling to $1mm^3$ isotropic voxels for computation of 3D textural features. In our view, these particular two steps may tend to reduce textural differences with data presenting other contrasts rather than exacerbating them. Finally, this type of processing is in line with existing literature on texture analysis.

Resolutions of the 3T T_1-weighted images and the 7T images were different, which may constrain the outcome results to a lower resolution than that of original T_2^*-weighted image data. However, it should be noted that the different data were used for different purposes. First, 3T T_1-weighted data were used for automated segmentation of regions of interest. Both 3T and 7T T_1-weighted data were used to align the 3T-based regions of interest on 7T T_2^*-weighted data in 3T space. A high order B-Spline interpolator was used during the transformation to minimize the effect of image interpolation. Second, T_2^*-weighted image data were used for texture analysis in the aligned regions of interest. For the computation of 3D textural features, those data were resampled to isotropic data of 1 x 1 x 1 mm^3, a resolution at which texture analysis of brain MR images is typically performed. The GLCM-based approach we used, which is solely based on voxel pairs, is not likely to be affected by the variation in spatial resolution during processing since it captures many different aspects of texture, and thus enabling the derived features to reflect image textures across different resolutions.

Textural features were computed based on GLCMs. In this computation, a GLCM matrix is normalized by dividing it by the sum of all entries [41], effectively normalizing the matrix for volume differences. Due to this normalization, differences in volume between the groups due to atrophy are not expected to cause a confounding effect in the findings of this study. Moreover, the magnitude-based features and phase-based features, computed from the same structures, yielded statistical differences for different structures, which would not be the case if structure size were a confounder.

GLCMs of each structure were averaged across directions. In general, one may consider treating GLCMs computed from different directions separately. However, in this work, we evaluated the framework using images of subcortical structures and assumed that textures would be approximately isotropic in these structures. We carried out experiments

to compare the features computed from GLCMs following different directions. A similar pattern of p values was obtained, empirically confirming our assumption. In addition, this pattern was similar to that obtained using the averaged GLCM. Based on this result, we chose to use the averaged GLCMs in computing the Haralick features.

The proposed framework revealed differences in subcortical structures in HD. Differences were found, before correcting the p values for multiple comparisons, mostly in the caudate, the putamen, and the pallidum in the manifest stage. Four phase-based features showed differences in the caudate nucleus in the premanifest stage. Among these four discriminative features, sum variance and information measure of correlation 1 showed differences in both premanifest and manifest stages. This signifies a possibility of using them to track textural changes in the caudate nucleus. Contrast and difference variance did not show a difference when comparing manifest HD with controls, which might be explained by the cross-sectional characteristic of the study. When considering Haralick features as a whole, significant differences were found after correction for multiple comparisons in the putamen between manifest and control groups using phase-based features. This supports the hypothesis that there is a textural change in the putamen observed in the manifest stage of the disease and this change could be detected using 7T T_2^*-weighted phase images. Investigators have reported atrophy in the caudate nucleus, the putamen [88, 89], the pallidum [20] in both premanifest and manifest stages, and the thalamus in the manifest stage of HD [90]. The textural findings of our study concur with existing findings on structural changes in these structures in the manifest stage, especially the putamen where significant differences were found.

It is known that the contrast on T_2^*-weighted images is induced by magnetic susceptibility of paramagnetic substances such as iron-containing ferritin [91]. This contrast is dominated by the tissue susceptibility effects at high field strengths [31]. There is increasing evidence that iron is involved in pathomechanisms that underlie many neurodegenerative diseases [14]. We speculate that the differences in texture shown in this study are related to abnormal iron deposition patterns which could be linked to altered axonal transport of iron and the effects of possible myelin breakdown [78]. Further evidence of increased iron in HD, especially in the putamen, comes from another study using asymmetric spin echo sequences [22] which reported increased iron content in the manifest and not in the premanifest stage. If iron is the main contributor to textural differences, then significant results are more likely to be found in manifest HD than in premanifest HD. The significant differences found in the comparison between manifest HD and controls provide supportive data for a causal role of iron in the textural changes reflected by 7T T_2^*-weighted phase images.

In the context of this study, 7T T_2^*-weighted features are sensitive to between-group differences with the phase-based features being more sensitive than the magnitude-based features. This indicates that 7T T_2^*-weighted images could be used for quantitative studies of textural changes inside structures. In addition, the results obtained using the 7T T_2^*-weighted phase images are different from those using the 7T T_2^*-weighted magnitude images, suggesting that they may have different information content. Finally, although the proposed texture analysis framework uses 7T T_2^*-weighted scans, it could also be applied to T_2^*-weighted scans obtained with a clinical 3T MRI system.

In conclusion, we have developed an automated framework for detecting between-group textural differences using 7T T_2^*-weighted imaging and a second-order texture analysis approach. The results obtained from in vivo HD data show that textural

differences can be detected using the proposed framework. We report the first evidence of textural heterogeneity of subcortical structures in HD and we show that the phase-based features are more sensitive than the magnitude-based features. Texture analysis of ultrahigh field T_2^*-weighted MR images could provide useful textural measures for noninvasive disease monitoring.

2.5 Acknowledgement

The 3D T_1-weighted MRI Images were acquired via the TRACK-HD study. We would like to thank the TRACK-HD study team for their support. TRACK-HD is supported by the CHDI/High Q Foundation, a not for profit organization dedicated to finding treatments for Huntington's disease.

3

Combined magnitude and phase-based segmentation of the cerebral cortex in 7T MR images of the elderly

This chapter was adapted from:

N. T. Doan, S. van Rooden, M. J. Versluis, A. G. Webb, J. van der Grond, M. A. van Buchem, J. H. C. Reiber, and J. Milles, "Combined magnitude and phase-based segmentation of the cerebral cortex in 7T MR images of the elderly," *Journal of Magnetic Resonance Imaging*, vol. 36, no. 1, pp. 99–109, 2012.

Abstract

Purpose: To propose a new method that integrates both magnitude and phase information obtained from magnetic resonance (MR) T_2^*-weighted scans for cerebral cortex segmentation of the elderly.

Materials and methods: This method makes use of K-means clustering on magnitude and phase images to compute an initial segmentation, which is further refined by means of transformation with reconstruction criteria. The method is evaluated against the manual segmentation of 7T in vivo MR data of 20 elderly subjects (age = 67.7 ± 10.9). The added value of combining magnitude and phase is also evaluated by comparing the performance of the proposed method with the results obtained when limiting the available data to either magnitude or phase.

Results: The proposed method shows good overlap agreement, as quantified by the Dice Index (0.79 ± 0.04), limited bias (average relative volume difference = 2.94%) and reasonable volumetric correlation ($R = 0.555$, $p = 0.011$). Using the combined magnitude and phase information significantly improves the segmentation accuracy compared with using either magnitude or phase.

Conclusion: This study suggests that the proposed method is an accurate and robust approach for cerebral cortex segmentation in datasets presenting low gray/white matter contrast.

3.1 Introduction

The cerebral cortex is the thin folded outermost layer of the brain, bordered by cerebrospinal fluid (CSF)/gray matter (GM) and GM/white matter (WM) interfaces. It has become an area of great interest for neuroscientists as its geometry and texture have been shown to provide relevant information about the disease stage in various forms of dementia [92–94], schizophrenia [95, 96] and attention deficit hyperactivity disorder (ADHD) [97]. More specifically, studies have suggested that Alzheimer's disease (AD) is associated with abnormal iron deposition within the cortex and basal ganglia [13, 14, 98–100], possibly due to amyloid-beta plaques associating with iron. MRI, through the use of T_2^*-weighted images, enables the noninvasive investigation of both focal and diffuse iron deposition in the brain in vivo [15, 101].

Accurate in vivo analysis of cortical iron deposition requires an accurate depiction of the cerebral cortex. A first approach would be to use existing cortical segmentation techniques based on T_1-weighted data and apply the obtained cortical mask to the T_2^* data. A large amount of research [102–104] has been carried out over the past several decades to develop automated cortex segmentation methods making use of T_1-weighted data, which often show good GM/WM contrast [105]. Such contrast can, however, be influenced by aging and pathological phenomena [29], hampering the final accuracy. Moreover, this approach requires the additional acquisition of T_1-weighted data and the resulting segmentation may suffer from global and local inaccuracies due to registration errors and acquisition artifacts between T_1 and T_2^* data. A second approach is to segment the cerebral cortex directly using T_2^*-weighted data, taking advantage of the more consistent GM/WM contrast offered by phase data compared with magnitude data [28, 72], as illustrated in Figure 3.1.

To the best of our knowledge, MR phase information has seldom been used for

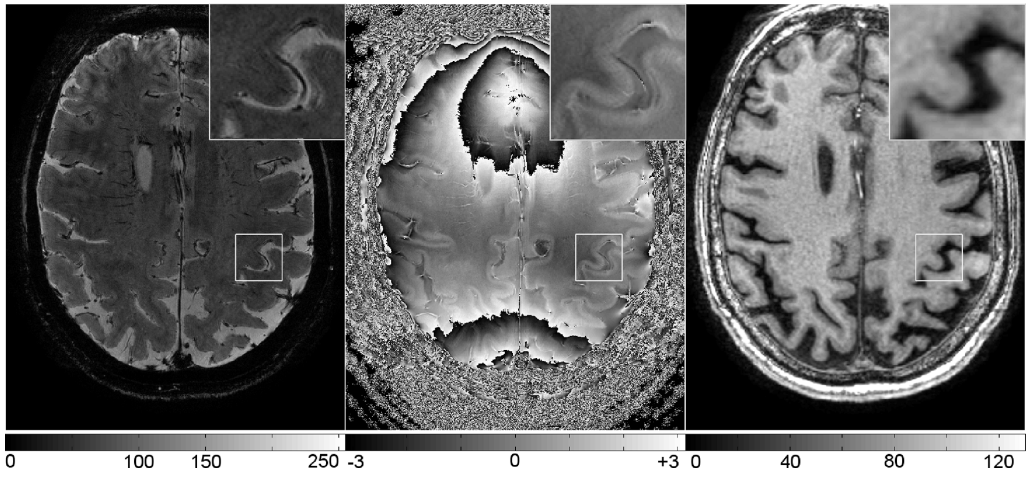


FIGURE 3.1: Example of GM/WM contrast in T_2^*-weighted magnitude (left), phase (middle) and T_1-weighted (right) images. The magnified region shows the lack of observable GM/WM contrast in T_2^* and T_1 magnitude images compared to phase images.

segmentation purposes. Bourgeat et al [106] have described a method using this information to complement traditional magnitude data to segment cartilage and bones in the knee. Within that application, they have shown that combining both magnitude and phase yields a significant increase in segmentation accuracy. This paper presents a novel approach using both MR magnitude and phase data to segment the cerebral cortex. The performance of the method as well as the added value of combining magnitude and phase data was evaluated using manual segmentations on 7T in vivo MR T_2^*-weighted data. In addition, the results of the presented method are also compared with those obtained by T_1-based approaches.

3.2 Materials and methods

3.2.1 Segmentation algorithm

The proposed algorithm performs the segmentation of the human brain cortex using T_2^*-weighted magnitude and phase data acquired at 7T. The algorithm follows the steps depicted in Figure 3.2.

3.2.1.1 Preprocessing

Preprocessing of the data consists of four steps: intensity inhomogeneity correction, phase unwrapping, nonbrain tissue removal, and ventricle segmentation.

Intensity inhomogeneity from the transmit and receive radiofrequency (RF) fields is a common artifact in high-field MRI characterized by slow nonanatomical intensity variation that degrades the performance of most image-based quantitative analysis methods [81]. Correction for such an artifact has now become a fixture of automated image analysis pipelines. In this study, the N3 algorithm [82] was applied for the correction using its implementation in the MIPAV software package [83].

Phase data originating from the MR scanner is bound to the $[-\pi, \pi]$ interval. Due to the inhomogeneity of the static magnetic field, its actual range is much larger than this interval, resulting in phase wraps, i.e. local and rapid transitions from -π to π and vice versa. These phase wraps have to be removed before any further processing steps take place. For this purpose, we implemented a Fourier-based approach based on filtering of

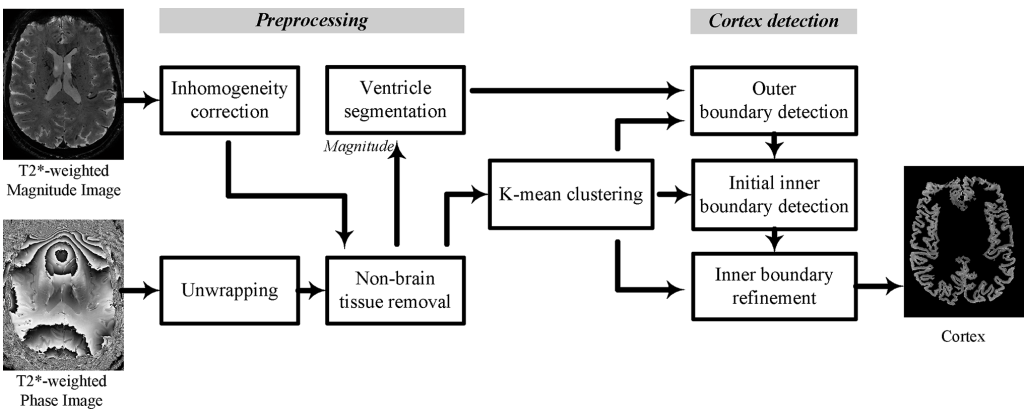


FIGURE 3.2: Flowchart of the presented method.

the *k*-space data as proposed by Wang et al. [25]. This method is based on the fact that unwanted phase variations are of lower spatial frequency than anatomical information. The central part of *k*-space was isolated using a Hanning filter with a filter size of [128 128] and the low spatial frequency information obtained was used to correct the original *k*-space data.

Nonbrain tissue removal was performed by a combination of thresholding and connected component analysis on both the magnitude and unwrapped phase data and was implemented according to Pandian et al. [107]. Two binary masks were derived by thresholding magnitude and unwrapped phase images based on their respective standard deviations. Connected component analysis was used to identify the largest component common to magnitude and phase data, providing a satisfactory intracranial mask. This mask was subsequently used to remove nonbrain tissues from both magnitude and phase images.

Finally, segmentation of the ventricle was performed on the T_2^*-weighted magnitude images using a 3D region-growing method with a manually selected seed point. Selection of the seed point is the only user interaction needed in the whole segmentation pipeline.

3.2.1.2 *K*-means clustering

After preprocessing of the data, a *K*-means clustering method [108] was used to extract the CSF/GM and GM/WM contrast information from the data. The magnitude image was clustered into 4 classes: GM, WM, CSF, and veins. The unwrapped phase image was clustered into 3 classes: GM, WM or CSF, and veins.

3.2.1.3 Outer boundary detection

In this step, the cortical outer boundary was detected using *K*-means clustering obtained from the magnitude image, as it contained good CSF/GM contrast information. The CSF and vein clusters were used as geometric markers of the cerebral cortex. In particular, the input image B_m to this step was computed as the brain mask from which the clusters of CSF and vein were removed, such that:

$$B_{\text{CSF,veins}} = \text{Kmeans}^{\text{CSF}}_{\text{magnitude}} \cup \text{Kmeans}^{\text{veins}}_{\text{magnitude}} \tag{3.1}$$

$$B_m = B_{\text{brain mask}} \cap \overline{B_{\text{CSF, veins}}} \tag{3.2}$$

where $\text{Kmeans}^{\text{CSF}}_{\text{magnitude}}$ denotes the CSF cluster, $\text{Kmeans}^{\text{veins}}_{\text{magnitude}}$ the vein cluster, $B_{\text{CSF,veins}}$ the binary mask of CSF cluster and vein cluster, and $B_{\text{brain mask}}$ the brain mask.

The outer boundary was detected based on connected component analysis of the boundaries of B_m. Prior to the analysis, an area closing was applied on B_m to remove noise introduced by *K*-means clustering while preserving fine details of the cortical boundaries. Subsequently, the boundaries of this mask were traced based on the Moore-neighbor tracing algorithm [109]. The resulting boundaries consisted of cortical and noncortical contours. 3D connected component labeling was then carried out on the binary map of the computed contours, such that each contour geometrically disconnected from the others was assigned a label. The CSF cluster and the ventricle segmentation obtained from the magnitude image were used as indicators to retain relevant contours as follows. Considering that the cerebral cortex is bordered by the outer CSF, contours that were geometrically connected to the CSF cluster and not connected to the ventricle segmentation were considered as cortical contours and retained. The retained contours

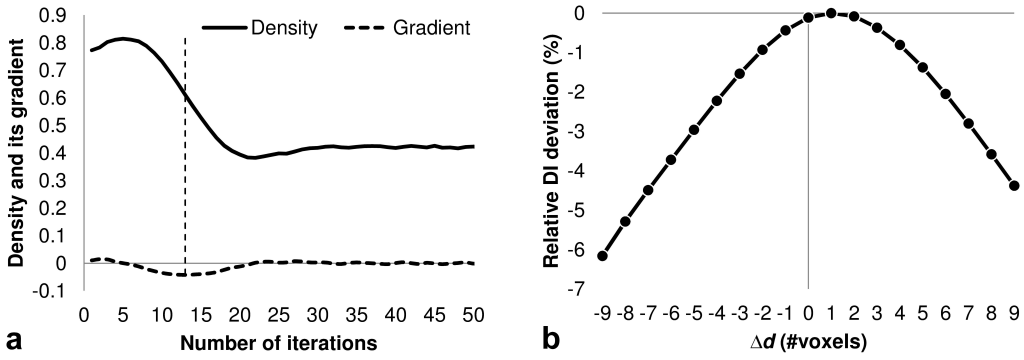


FIGURE 3.3: a: Example of the evolution of GM voxel density (solid curve) and the cost function associated to initial inner boundary (dashed curve) as a function of the distance to the outer contour. Each iteration corresponds to an erosion of the outer mask using a unit ball structuring element. b: Relative deviation of the Dice Index when the position of the initial inner boundary is shifted.

were further refined to obtain the outer boundary. This refinement was done by computing the region residing inside the contours using connected component analysis, keeping the largest component. The outer boundary was identified as the contour of the computed region.

3.2.1.4 Inner boundary detection

The inner boundary was detected based on GM/WM contrast extracted from both magnitude and phase images. The subject of this detection step was therefore the union of the GM clusters from magnitude and phase images, denoted as B_{GM}. The following operations were carried out to preprocess B_{GM}: noise removal using area closing, ventricle removal using the segmented ventricle mask, and masking using the mask that was bordered by the outer boundary (outer mask).

Initial inner boundary detection

This step aimed at obtaining an approximation of the inner boundary by means of a minimum cost approach. The cost function was computed as follows. The outer mask was iteratively eroded using morphological erosion with a unit ball structuring element. In each iteration, the contour of the eroded mask was detected. Subsequently, the density of GM-labeled voxels on this contour was computed as the total number of GM-labeled voxels located on the contour divided by the length of the contour. The cost function was defined as the gradient of the density.

In the first iterations, the density increased. In the middle of the cortical layer, the density started to decrease. At the global GM/WM interface, the density function decreased at its maximum rate and the cost function reached its minimum, as shown in Figure 3.3a. The distance between this global GM/WM boundary and the outer contour was computed as:

$$\begin{aligned} d &= \arg \min_{n \in [1;N]} \nabla D(n) \\ D &= [D_1, D_2, ..., D_n, ..., D_N] \end{aligned} \tag{3.3}$$

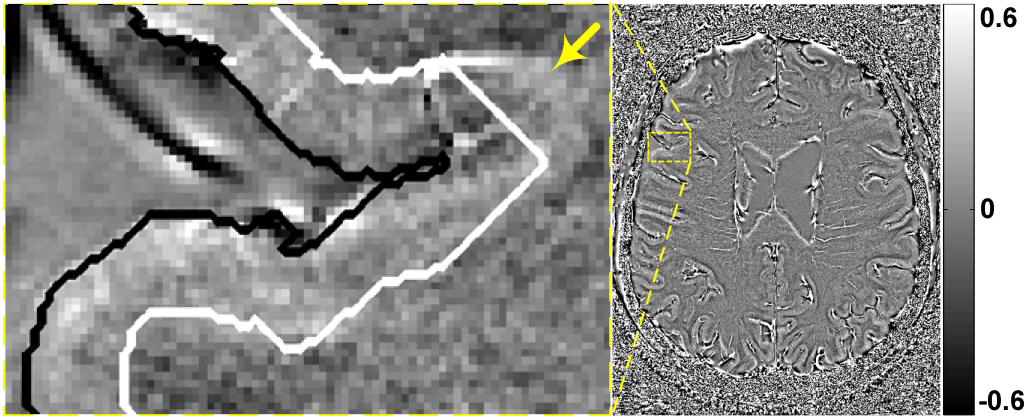


FIGURE 3.4: Outer boundary (black) and initial inner boundary (white) overlaid on a region of interest of an unwrapped phase image. The arrow indicates a cortical segment to be recovered in the refinement step.

where N denotes the maximum number of iterations and was chosen as an arbitrarily large number.

Vector D contained the density of GM-labeled voxels at different iterations:

$$D_n = \frac{1}{\text{length}(\mathbf{C}_\text{n})} \sum_{x,y,z \in \mathbf{C}_\text{n}} B_{GM}(x,y,z) \tag{3.4}$$

n being the number of iterations, B_{GM} the binary mask of the combined GM clusters, and $\mathbf{C}_n$ the contour of the eroded mask at iteration n.

The initial inner boundary and the outer boundary were the boundaries of the initial segmentation $S_{initial}$. An example of the detected boundaries overlaid on a magnified region of an unwrapped phase image is presented in Figure 3.4. Once this initial segmentation was obtained, it was further refined to segment cortical regions which had not been captured in previous steps due to the lack of CSF/GM contrast. The refinement was carried out based on the following transformation with reconstruction criteria.

Transformation with reconstruction criteria

Reconstruction, in the binary case, consists of extracting connected regions of a mask image f that are "marked" by an image g (marker) contained in f [110]. Reconstruction transformation of marker g in image f ($g \subseteq f$) using geodesic dilations is defined by:

$$R(f,g) = \lim_{n \to \infty} \delta_f^n(g) = \underbrace{\delta_f^1 \delta_f^1 ... \delta_f^1(g)}_{\text{until stability}} \tag{3.5}$$

where $\delta_f^1(g)$ is a geodesic dilation, computed as: $\delta_f^1(g) = f \wedge \delta(g)$, $\wedge$ the infimum operator, and $\delta(g)$ the dilation of g using an elementary ball (a ball with unit radius). $R(f,g)$ is an iterative process in which the geodesic dilation is repeated until the process is stable.

One of the most interesting characteristics of reconstruction transformations is that they enable the complete extraction of the marked objects by preserving the edges.

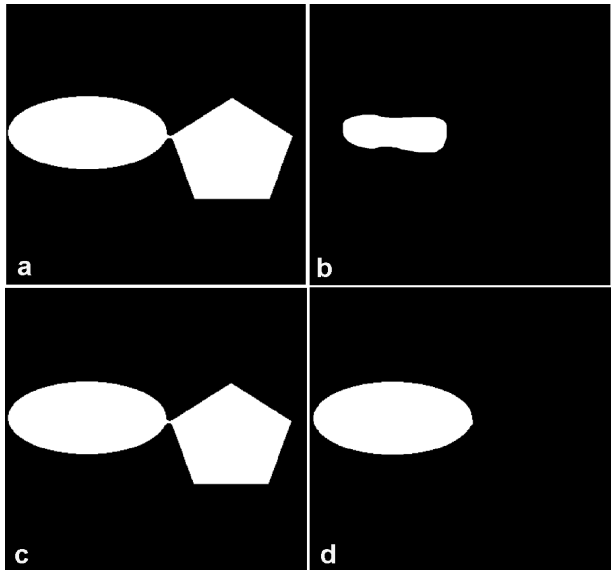


FIGURE 3.5: Example of transformation with reconstruction criteria: (a) mask image f, (b) marker image g aiming at selecting the ellipse, (c) results of reconstruction transformation $R(f,g)$, and (d) results of transformation with reconstruction criteria $R_{\lambda,f}(g)$ with λ =1. In contrast to reconstruction transformation, transformation with reconstruction criteria could correctly extract the ellipse despite the presence of the narrow link that connects the ellipse and the pentagon.

However, since they reconstruct all connected regions, undesirable regions connected to the marked regions by narrow links are also reconstructed. This issue is referred to as a leakage problem: wide flat regions joined by narrow links cannot be treated in a separated way [111]. Transformation with reconstruction criteria was proposed to solve this problem.

For binary images, reconstruction transformation can be viewed as a region-growing algorithm with the marker image used as seed points, and transformation with reconstruction criteria can be viewed as an extension of the region-growing algorithm with an opening operator used to separate thin connected sections. Transformation with reconstruction criteria is built based on reconstruction transformation by introducing a size criterion to stop the reconstruction process. A morphological opening is used to stop the reconstruction of the regions where the criterion is not verified. Reconstruction criteria transformation of marker g in image f is formulated as:

$$R_{\lambda,f}(g) = \gamma_\lambda \lim_{n\to\infty} \omega^n_{\lambda,f} = \underbrace{\gamma_\lambda \delta^1_f \gamma_\lambda \delta^1_f \gamma_\lambda ... \delta^1_f \gamma_\lambda \delta^1_f(g)}_{\text{until stability}} \tag{3.6}$$

where γ_λ denotes an opening using a structuring element size λ.

Figure 3.5 demonstrates the ability to deal with leakage problems of transformation with reconstruction criteria. For further details on transformation with reconstruction criteria, we refer the readers to the works by Terol-Villalobos et al [112, 113].

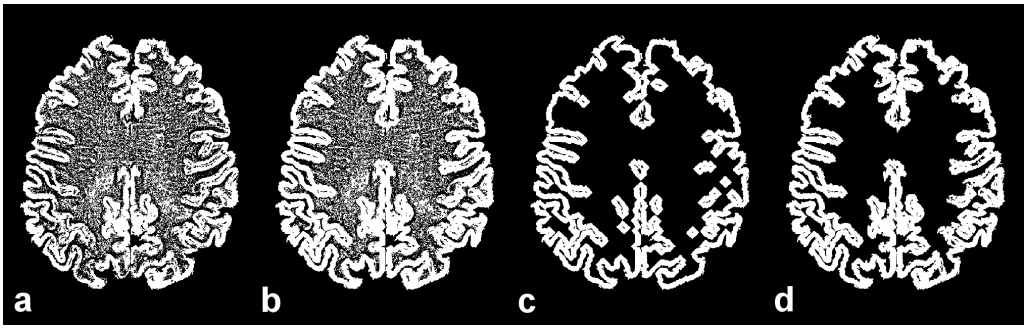


FIGURE 3.6: Refinement of the initial segmentation using transformation with reconstruction criteria: (a) B_{GM}, (b) mask image f combining B_{GM} and $S_{initial}$, (c) initial segmentation $S_{initial}$ (marker image g), and (d) final segmentation S_{final}.

Inner boundary refinement

The refinement was performed by means of transformation with reconstruction criteria based on the initial segmentation $S_{initial}$ and the combined mask B_{GM} of GM clusters. Using $S_{initial}$ as an approximation of the cortex segmentation, regions connected to this initial segmentation by wide links were considered likely to be cortical segments. During the reconstruction process, morphological opening was applied to impose a constraint on the width of geometrical connections between regions in marker g such that noncortical regions connected to the initial segmentation by narrow links would not be captured.

The mask image f was derived from $S_{initial}$ and B_{GM}, such that:

$$f = S_{initial} \cup B_{GM} \tag{3.7}$$

Choosing $S_{initial}$ as marker g, the final segmentation S_{final} was computed as:

$$S_{final} = R_{\lambda,f}(S_{initial}) \tag{3.8}$$

where:

$$R_{\lambda,f}(S_{initial}) = \underbrace{\gamma_\lambda \delta_f^1 \gamma_\lambda \delta_f^1 \gamma_\lambda ... \delta_f^1 \gamma_\lambda \delta_f^1 (S_{initial})}_{\text{until stability}} \tag{3.9}$$

A disk-shaped structuring element with radius λ equal to 1 was used. Due to the high GM/WM contrast on the phase image, the undesired links associated with the noncortical segments were narrow and most likely caused by noise from the K-means clustering results. Choosing λ equal to 1 not only enabled sufficient suppression of those links during the reconstruction but also maximized the ability to capture cortical segments. A demonstration of the refinement step is given in Figure 3.6.

3.2.2 Validation data

The presented cortical segmentation algorithm was evaluated using in vivo data obtained from 20 elderly participants (mean age = 67.7 ± 10.9, female/male = 7/13). These participants were recruited from the Memory Clinic (Leiden University Medical Center,

Leiden, The Netherlands). This study was approved by the Center's Committee on Medical Ethics. Written informed consent was obtained from all subjects.

MRI was performed with a whole body human 7T MR system (Philips Medical Systems, Best, the Netherlands) using a quadrature transmit, 16-channel receive head coil (Nova Medical, Wilmington, MA). Participants were scanned using a flow compensated transverse 2D T_2^*-weighted gradient-echo scan including the frontal and parietal regions with a scan duration of 9.59 minutes (TR/TE/flip angle = 794ms/25ms/45^o , voxel size = 0.24 x 0.24 x 1 mm^3, field of view [FOV] = 240 x 180 mm^2), acquiring 20 slices. This technique was adapted from Duyn et al [72]. To minimize magnetic field inhomogeneity and reduce the number of phase wraps, third order shimming was performed using a manufacturer supplied image based approach. A navigator echo correction technique (TE = 9.5ms) was used to correct for resonance frequency fluctuations [114]. Within the same session, a T_1-weighted gradient echo sequence was applied to obtain a whole brain scan with scan duration of 9 minutes (TR/TE = 5.6ms/2.6ms, TI = 1300ms, voxel size = 0.7 x 0.7 x 0.7 mm^3, 248 sagittal slices).

3.2.3 Validation approach

The validation aimed at evaluating the robustness and performance of the presented method, as well as the added value of combining magnitude and phase data. For those purposes, we investigated the following aspects:

- *Robustness* with regard to initialization, by evaluating the influence of the initial inner boundary estimate on the final segmentation.
- *Accuracy*, by comparing the obtained segmentation masks with manual segmentations.
- *Added value* of combining phase and magnitude, by comparing the obtained segmentation masks with those obtained using only the magnitude or phase information.

Additionally, to compare the performance of the presented method with that of T_1-based approaches, we compared our segmentations with the segmentations obtained by applying two commonly used methods, FreeSurfer and FSL, on the T_1-weighted images.

3.2.4 Validation measurements

3.2.4.1 Overlap agreement

The overlap agreement between our segmentations and the manual segmentations was quantified using the Dice Index (DI) [115]. The DI, being proportional to the ratio between the overlap and the sum of two volumes, measures the degree of overlap between the volumes.

$$DI = \frac{2V_{A\cap B}}{V_A + V_B} \tag{3.10}$$

The DI is bounded by 0, no overlap, and 1, perfect overlap.

3.2.4.2 Volumetric agreement

Since the DI does not provide information on the accuracy of the measured absolute volumes, we also compared volumes of the segmentations by means of Bland-Altman and correlation analysis.

Bland-Altman analysis [116] was carried out to assess the agreement in terms of volumetric measurement and whether the difference in volume tended to change with the size of the measurements. The correlation between the volumes obtained using the presented method and manual segmentation was assessed using Pearson correlation analysis. Additionally, a paired t-test was performed to compare the mean of the obtained volumes. The statistical analysis was performed using the SPSS software (v. 17.0, Chicago, IL) with a significance level of 0.05.

Finally, the relative volume difference (VD) between two segmentations, indicative of potential bias within the quantitative results, was computed as following:

$$VD(\%) = \frac{V_A - V_B}{V_B} * 100 \tag{3.11}$$

The DI measures the agreement of the segmentations in terms of spatial overlap but not volumetric agreement. Conversely, relative VD measures the degree of volume matching but not spatial matching. Therefore, DI and relative VD, when used together, quantify both spatial and volumetric agreement. A high DI together with a low relative VD is an indicator for a good boundary match between the segmentations.

3.2.5 Robustness with regard to initial inner boundary positioning

The initial inner boundary was positioned by computing its global distance d to the outer boundary. In this section, we studied how sensitive the segmentation accuracy was to the placement of this boundary. The presented method was applied on every subject with the initial inner boundary not located at the position identified based on Eq. 3.3 but instead shifted with respect to that position. Deviation of the distance (Δd) was computed as following: $\Delta d = d_{shifted} - d$; where $d_{shifted}$ was the distance between the shifted boundary and the outer boundary and d, computed from Eq. 3.3, the distance between the original boundary and the outer boundary. The more negative or positive Δd, the more shifted the boundary. Negative values of Δd correspond to the boundary being shifted outwards towards the outer boundary, and vice versa. For each value of Δd, the average DI across all subjects was computed. The relative DI deviation was computed as the difference in percentage of the resulting DI and its maximum value.

3.2.6 Accuracy of the segmentation method

For the purpose of evaluating the accuracy of our segmentation method, we chose to use manually drawn contours as the gold standard. For each subject, the outer boundary was traced on the magnitude image and the inner boundary was traced on the phase image. This manual contour tracing task was performed by a trained human observer on each axial slice of the 3D volume to obtain the final segmentation of the cortex using the ITK-SNAP software [117]. Accuracy was evaluated both in terms of overlap and volumetric agreement.

3.2.7 Added value of combining phase and magnitude

To demonstrate the added value of combining the magnitude and phase information, we compared the performance of the presented method with the results obtained when limiting the available data to either MR magnitude or (unwrapped) phase. For that purpose, the segmentation results obtained by each of those three methods were compared with manual segmentations using overlap and volumetric agreement measures as described previously.

3.2.8 Comparison with T_1-based segmentation

In this section we performed a quantitative comparison between our segmentations, the segmentations obtained by applying FreeSurfer/FSL on T_1-weighted images and the manual segmentations. FreeSurfer and FSL were applied on T_1-weighted images of all datasets. This resulted in 20 T_1-based cortical segmentations from FSL and 11 from FreeSurfer. The latter did not produce a result from 9 out of 20 datasets most likely because of low contrast T_1-weighted scans. To avoid possible bias for the comparison with these T_1-based techniques, we chose to limit this comparison to the 11 subjects on which both FreeSurfer and FSL produced the segmentations.

The T_1-weighted segmentation masks were linearly registered to T_2^*-weighted space for comparison purpose using FSL's linear registration tool FLIRT. Since T_2^*- and T_1-weighted data were acquired immediately after one another, we chose to limit the registration transform to 7 degrees of freedom. We used the correlation ratio as a cost function and a nearest neighbor interpolator.

Subsequently, T_1-based segmentations were compared with the manual segmentations and our segmentations both in terms of overlap agreement and volumetric agreement.

3.3 Results

3.3.1 Sensitivity to the initial inner boundary position

The presented method placed an initial estimate of the GM/WM boundary using global GM voxel density, as described in the detection of inner boundary. We evaluated the influence of this step, illustrated in Figure 3.3a, on the final segmentation results by evaluating the variation of the average DI as a function of initial boundary GM/WM location. The resulting curve, depicted in Figure 3.3b, demonstrates two main points. First, the initial position determined using global GM voxel density is close to the global optimal position. Second, the outcome of the segmentation is not very dependent on an accurate initial positioning. For example, a variation of 9 voxels (≈2.2 mm), is reflected by a variation of only ≈6% in the computed DI.

3.3.2 Accuracy of the segmentation method

Figure 3.7 shows an example of the segmentation obtained using the presented method in which the cortical boundaries are overlaid on the magnitude and unwrapped phase images. A scatter plot and a Bland-Altman plot assessing the agreement regarding volumetric measurement for the 20-mm imaged section between the presented method and the human observer are shown in Figure 3.8. Numerical results are provided in Table 3.1.

In terms of volumetric measurement, from the scatter plot one can observe a significant correlation between our segmentations and the manual segmentations ($R = 0.555$, $p = 0.011$). In terms of spatial overlap, automated segmentation results show good agreement with the manual gold standard ($DI = 0.79 \pm 0.04$). The Bland-Altman analysis shows that the bias of the presented method compared with manual segmentation is small, as indicated by an average relative volumetric difference of 2.94%. A negative trend is visible, but a Pearson correlation analysis reveals a nonsignificant correlation of −0.333 ($p = 0.15$). Finally, a paired t-test between the automated and manual segmentation volumes shows no significant difference ($p = 0.391$).

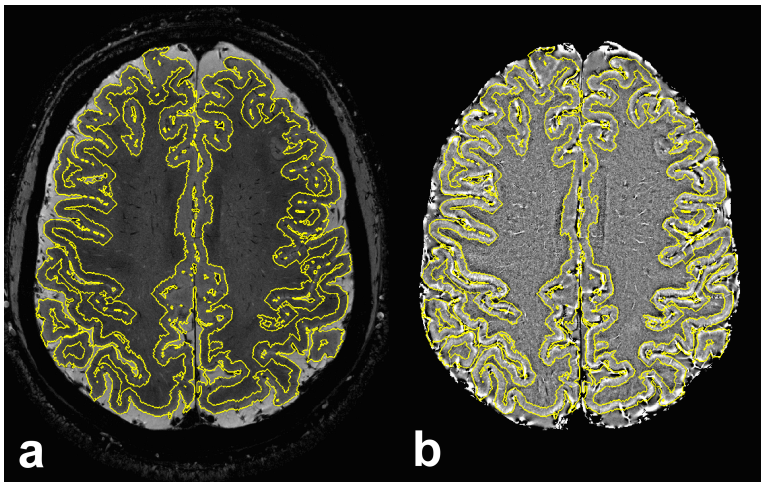


FIGURE 3.7: Example of cerebral cortex segmentation obtained by the method outlined in this article. Cortical boundaries are overlaid on (a) T_2^*-weighted magnitude image and (b) T_2^*-weighted phase image.

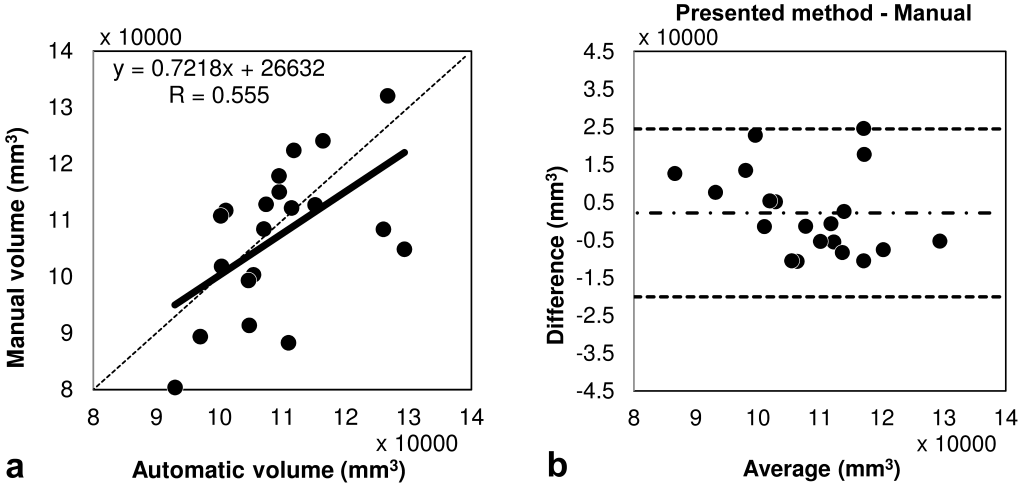


FIGURE 3.8: Volumetric agreement between automated and manual segmentations: (a) Scatter plot. The dashed line represents $y = x$, the solid line is the linear regression line; (b) Bland-Altman plot. Dashed dotted line = mean, dashed lines = mean ± 2SD.

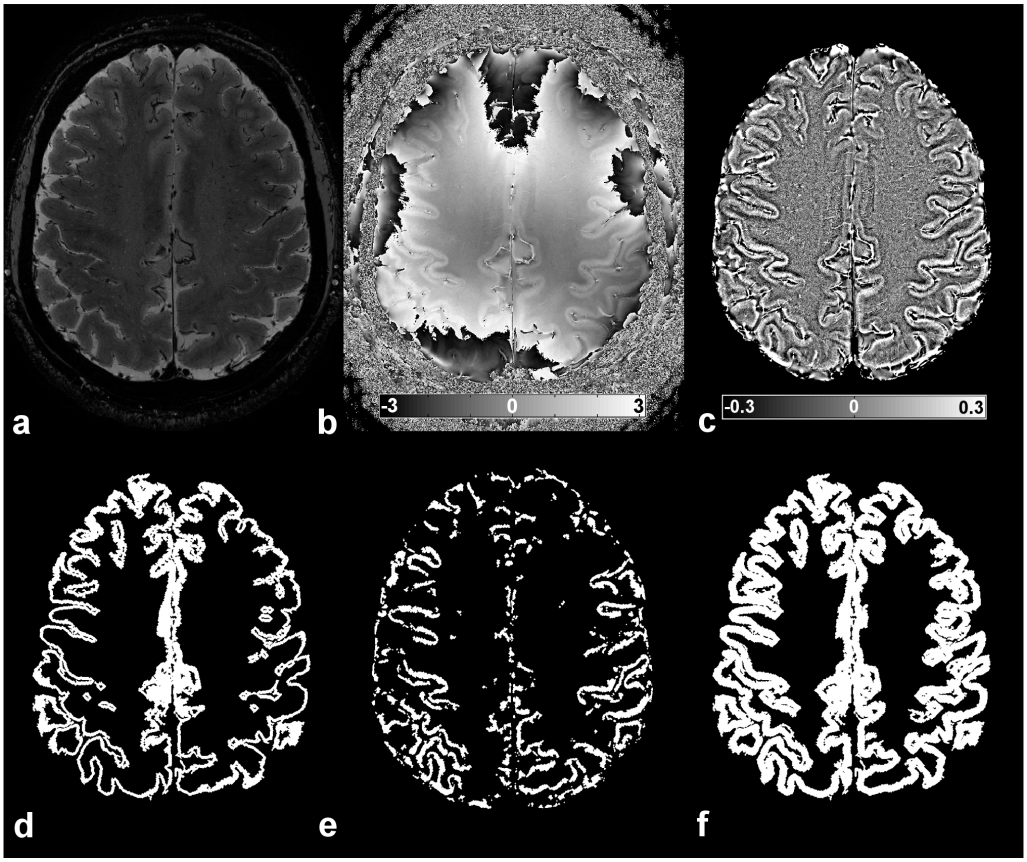


FIGURE 3.9: Example of the segmentations obtained using different approaches: (a) magnitude, (b) original phase, (c) unwrapped and skull-stripped phase, (d) segmentation by magnitude-only method, (e) segmentation by phase-only method, and (f) segmentation by the presented method.

3.3.3 Added value of combining phase and magnitude

Figure 3.9 shows an example of the segmentations obtained using only magnitude data, using only phase data, and using the combined magnitude and phase, respectively. Quantitative evaluation of the magnitude-only and phase-only methods in comparison with the validation of the presented method is provided in Table 3.1.

From a qualitative perspective, it can be observed that using only phase data provides unrealistic cortical segmentations and that using only magnitude data produce segmented cortical volumes that are too thin compared with those produced using the combined data. Those observations are confirmed by the quantitative evaluation. First, when considering segmentation overlap, the combined approach provides clearly better result than the other two methods both in terms of average and standard deviation. Second, relative VDs show that the combined approach provides segmentation results that, on average, are very close to the manual gold standard whereas the other two methods provide clearly

TABLE 3.1: Overlap agreement and volumetric comparison for different approaches.

	Dice Index (DI)		Volumetric comparison					
			% Volume difference (VD)				Correlation	
	Average	SD	Average	SD	Min	Max	R	p
Presented method	0.79	0.04	2.94	11.02	−9.58	25.74	0.555	0.011
Magnitude-only	0.60	0.12	−39.36	12.12	−62.24	−13.07	0.551	0.012
Phase-only	0.35	0.09	−65.46	16.43	−78.86	0.28	−0.031	0.895

underestimated cortical volumes. Finally, the Pearson correlation analysis shows that both the combined and magnitude-only methods provide results that correlate significantly with manual segmentation volumes. Overall, results obtained using the presented method clearly show that combining magnitude and phase data provide a significant improvement in quantitative measures with regard to using only magnitude or phase information.

3.3.4 Comparison with T_1-based segmentation

On the subset of 11 subjects used for the comparison, FreeSurfer and FSL show a lower overlap agreement with respect to the manual segmentations ($DI = 0.7 \pm 0.03$ and 0.7 ± 0.07 respectively) than the presented method ($DI = 0.81 \pm 0.02$). Regarding volumetric agreement, a good correlation is observed when comparing T_1-based segmentations to our segmentations (FreeSurfer: $R = 0.853$, $p < 0.001$ and FSL: $R = 0.597$, $p = 0.053$) and manual segmentations (FreeSurfer: $R = 0.848$, $p < 0.001$ and FSL: $R = 0.659$, $p = 0.027$). Our segmentations exhibit a higher correlation with the manual segmentations ($R = 0.902$, $p < 0.001$) than the T_1-based segmentations. The volumes segmented by the T_1-based techniques, however, are much smaller than either our volumes (average VD for FreeSurfer $= -21.0 \pm 3.7$ % and FSL $= -13.5 \pm 10.1$ %) or the manual volumes (average VD for FreeSurfer $= -22.2 \pm 4.2$ % and FSL $= -15.1 \pm 9.1$ %).

3.4 Discussion

In the segmentation pipeline, the accuracy of the refinement step as well as that of the final segmentation was dependent on the initial segmentation, since the refinement further captured cortical segments using the initial segmentation as an anatomical landmark. The accuracy of the initial segmentation was dependent on the detection of the outer boundary since the outer boundary was used as a curved landmark to detect the initial inter boundary. The detection of the outer boundary relied upon the magnitude CSF/GM contrast only, thus avoiding possible contamination of this boundary caused by artifacts from residual phase wraps. Therefore, this contrast and its extraction directly conditioned the accuracy of the final segmentation. This conditioning issue did not cause a negative effect on the segmentation accuracy since T_2^*-weighted magnitude images contain good CSF and GM separation information. During the segmentation, this information was efficiently extracted by K-means clustering, enabling good estimation of the outer boundary and thereby providing a reliable landmark for the subsequent steps.

Large variations of the initial inner boundary position did not have much effect on the results. As shown in Figure 3.3b, the maximum value of the DI when shifting the initial inner boundary was obtained at $\Delta d = 1$ (1 voxel shifted), and in general, the

relative DI deviation with respect to that maximum was small (absolute deviation < 6.5 %). Furthermore, the initial inner boundary identified by the presented method was close to the optimal position as indicated by the negligible relative DI deviation of −0.11%.

In the refinement step, the algorithm captured cortical segments which had not been included in the initial segmentation by means of transformation with reconstruction criteria, resulting in a significant improvement in the segmentation performance. The DIs of the initial segmentation and final segmentation compared with the manual segmentation were 0.71 ± 0.04 and 0.79 ± 0.04, respectively.

The proposed method is based on K-means clustering applied separately on magnitude and phase images. We carried out experiments to compare the results obtained using multifeature clustering, these features being phase and magnitude data, to those using the presented method, where two separate clustering steps were used. Quantitative results were in favor of separate K-means clustering. We observed that the intensity of different tissue types, e.g. CSF and WM, appeared to be overlapping on the unwrapped phase images, resulting in a different optimal number of classes required for magnitude and phase data. This issue may have caused the multifeature approach to perform not as well as expected. In contrast to the multifeature approach, applying K-means clustering on the magnitude images with the number of classes K equal to 4 produced good CSF and vein clusters, which allowed the subsequent steps to detect the outer boundary. The GM/WM contrast is clearer on phase images and could be extracted by applying K-means clustering with 3 classes. The resulting clusters included vein, GM, and WM or CSF. The GM/WM boundary was clearly present on the binary mask of the GM cluster, enabling the detection of the inner boundary using this cluster. Based on those results, we chose to use separate K-means clustering and combine the results afterwards.

The comparison between the presented method and the methods using only magnitude or phase demonstrated the added value of using the combined magnitude and phase information in the segmentation. Segmentation using only phase data failed to produce good segmentation. The developed algorithm initiated the segmentation with the detection of the outer CSF/GM boundary on which the subsequent steps strongly depended. Since CSF/GM contrast on the phase images was not good and WM and CSF could not be clustered in different classes, the outer boundary was inaccurately detected, resulting in poor segmentation. Segmentation using only magnitude data, on the other hand, was superior to the phase-only method but the results were still not satisfying as suggested by the numerical results in Table 3.1. Based on the good CSF/GM contrast on the magnitude images, this magnitude-only method could provide reliable outer boundary. However, the lack or decrease of GM/WM contrast on magnitude data of elderly subjects resulted in incorrect estimation of inner boundary and low performance of the algorithm. Unlike the magnitude-only method, the presented method used a combination of magnitude and phase information in the inner boundary detection. The results show an obvious improvement in terms of spatial overlap and volumetric measurement, which demonstrates the importance of phase data in this step. The GM/WM contrast on the phase images, which appeared not to suffer as much from the aging effect compared with the magnitude images, was the main contributor to the improvement of the segmentation.

When compared with the manual reference, the T_1-based approaches show a lower overlap and volumetric agreement than the presented method. We believe that the primary reason for the inaccuracy of the T_1-based segmentations is the decrease of GM/WM contrast on T_1-weighted images due to aging effects [29, 118]. Other possible

sources of this inaccuracy could be small geometric distortions between T_1 and T_2^* data and minor registration errors. The results of the quantitative comparison suggest that for cortical segmentation on T_2^*-weighted images of the elderly, the presented method has a superior performance compared with T_1-based techniques.

The presented method provides a solution to accurately segment the cerebral cortex for elderly populations, which remains a challenge for existing T_1-based algorithms due to the effect of aging on GM/WM contrast of magnitude data. It demonstrates the added value of integrating the phase information in a segmentation process. The presented method produces good cerebral cortex segmentation using only T_2^*-weighted data, which is an important prerequisite for volume-based or texture-based studies of neurodegenerative diseases. The method could be of particular interest for in vivo studies based on susceptibility effects associated with cortical iron content at ultrahigh field MRI. Moreover, it possibly alleviates the need for acquiring a high resolution T_1-weighted dataset when targeting abnormal iron deposition within the cortex. This would result in a shorter overall acquisition protocol, which is particularly important for elderly subjects and patients with neurodegenerative diseases.

In conclusion, we have presented an algorithm which combines magnitude and phase information to segment the human brain cerebral cortex using 7T MR T_2^*-weighted images. The proposed method makes use of contrast information obtained from the phase data to overcome the lack of contrast in magnitude data in a two-step framework where an initial segmentation is computed based on K-means clustering and further refined using transformation with reconstruction criteria. Quantitative evaluation carried on 7T MR data of elderly subjects demonstrated that the proposed method is able to provide accurate cortical segmentation of challenging datasets, where GM and WM contrast of the magnitude image is decreased significantly.

3.5 Acknowledgement

The authors would like to thank the memory clinic of Leiden University Medical Center for its contribution.

4

Group-wise cortical feature analysis using high field T_2^*-weighted MR images highlights local differences between young and elderly healthy subjects

This chapter was adapted from:

N. T. Doan, S. van Rooden, M. J. Versluis, M. Buijs, A. G. Webb, J. van der Grond, M. A. van Buchem, J. H. C. Reiber, and J. Milles, "Group-wise cortical feature analysis using high field T_2^*-weighted MR images highlights local differences between young and elderly healthy subjects," Submitted

Abstract

T_2^*-weighted MR images of the cerebral cortex at high field are increasingly used to study tissue susceptibility changes related to aging or pathologies. Quantitative approaches for cortical analysis using these images however have not been fully explored. We present a novel method for the computation of quantitative cortical measures and group-wise comparison using 7T T_2^*-weighted magnitude and phase images. We investigated grey matter (GM)/white matter (WM) contrast and cortical profiles which depict the magnitude or phase variation across the cerebral cortex. The cortex was segmented using a combination of T_2^*-weighted magnitude and phase information, and subsequently parcellated based on an anatomical atlas. Local GM/WM contrast and cortical profiles were computed from the magnitude and phase images in each parcellated region and further used for group-wise comparison. Differences in local GM/WM contrast were assessed using a Mann-Whitney U-test. A permutation test was applied for a global comparison using the entire cortical profiles at each region. Additionally, a second permutation test was carried out at every cortical depth to assess local differences on the regional profiles. We applied the method to compare a group of 10 young volunteers with a group of 15 elderly subjects. Using local GM/WM contrast, significant differences were shown in at least 14 out of 17 studied regions. Local comparison at each cortical depth highlighted localized differences in the centre and the boundaries of the cortex. Results of this study show that the proposed method can be a useful tool for studying cortical changes in normal aging and may also be useful in studies of neurodegenerative diseases.

4.1 Introduction

Post-mortem studies of the cerebral cortex have reported changes related to normal aging or pathological processes [98, 119]. Using magnetic resonance imaging (MRI), morphological changes such as cortical thinning have been found in aging and neurodegenerative diseases [94, 120]. However, the cortex does not only change in geometry but also in tissue signal properties: for instance, age-related cortical signal intensity alterations have been demonstrated on MR images [29]. Recent advances in MRI techniques with the ability to characterize tissue susceptibility properties have enabled non-invasive investigation on changes of substances such as myelin and iron with regard to aging and diseases [15, 72].

T_2^*-weighted MR data have been used in susceptibility-based studies of the brain. For example, phase information has been increasingly investigated as an indirect means to measure iron-induced changes associated with aging [121] and neurodegenerative diseases [73, 122]. It has been shown that the contrast between cortical grey matter (GM) and subcortical white matter (WM) on phase images is more pronounced as compared to the magnitude images [28, 29] and such contrast can be used for cortical segmentation [123]. MR phase was shown to reflect iron-induced differences in brain tissue susceptibility in GM regions [124]. Elevated iron deposition associated with aging was reported using phase images [121]. Recently, an increased phase shift was demonstrated in 7T MR images of Alzheimer's disease (AD) patients compared to age-matched control subjects [125]. Those studies of the cortical GM, even though valuable, were based on manual delineation of regions of interest (ROIs), which limits their generalization for the entire cortex, their application to larger datasets, and thus their translation to clinical use. With increased field strengths, phase images show an increased sensitivity with respect to tissue susceptibility and an increased image resolution [26, 31], allowing susceptibility-based studies of the cortical laminae. Intracortical contrast in 7T MR phase images was shown to be suggestive of an underlying layered structure of the cortex [72]. Based on 7T MRI and histochemical staining of the occipital cortex, it was demonstrated qualitatively that myelin-associated iron distributing over the laminar structure of the cortex forms the dominant source of the layer-specific phase variations [15]. Quantitative measurement of phase variation across the cerebral cortex at local cortical regions could harbour information on regional myelin and iron distribution, which could be useful in detecting and differentiating age-related and neurodegenerative cortical changes.

The aim of this study is to propose a novel and highly automated method for local quantitative analysis of the cerebral cortex using high field T_2^*-weighted images. The proposed method allows one to compute GM/WM contrast and cortical profiles at local cortical regions on T_2^*-weighted magnitude and phase images, and perform group-wise comparison using the computed measures. We apply the method to 7T MR images of young and elderly healthy subjects.

4.2 Materials and methods

4.2.1 Subjects

A group of 15 healthy elderly participants (mean age = 75.1 ± 3.6 years, female/male = 5/10) was recruited by focused advertisement. Subjects with an age between 69-80 years, who were living independently and had a Mini-Mental State Examination (MMSE) score ≥ 25 and a Geriatric Depression Scale (GDS) ≤ 4, were selected for inclusion. Subjects

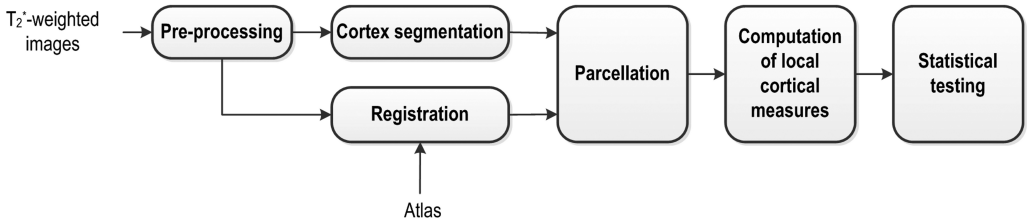


FIGURE 4.1: Flowchart of the presented analysis method.

with the following diseases were excluded: stroke, Parkinson's disease, dementia, diabetes mellitus, rheumatoid arthritis, polymyalgia rheumatic, cancer, heart failure, and chronic obstructive pulmonary disease. A second group of 10 healthy young participants (mean age = 23.3 years, female/male = 7/3) was also recruited by focused advertisement and selected based on age (20-30 years old). These two groups of subjects were originally recruited for different studies and the data acquired were subsequently included in this study. This study was approved by the local Committee on Medical Ethics and written informed consent was obtained from all subjects.

4.2.2 MR imaging

MRI was performed on a whole body human 7T MR system (Philips Medical Systems, Best, the Netherlands) using a quadrature transmit, 16-channel receive head coil (Nova Medical, Wilmington, MA). Participants were scanned using a flow compensated transverse 2D T_2^*-weighted gradient echo scan with a scan duration of 10 minutes (TR/TE/flip angle = 1784ms/25ms/60^o, voxel size = 0.24 x 0.24 x 1mm^3, FOV = 240 x 180mm^2), acquiring 46 slices. To minimize magnetic field inhomogeneity and reduce the number of phase wraps, third order shimming was performed using a manufacturer supplied image based approach. A navigator echo correction technique (TE = 9.5ms) was used to correct for resonance frequency fluctuations [114].

Due to difference in the time available for the T_2^*-weighted scan described above, even though the same T_2^*-weighted scan protocol was applied for all subjects, the number of scans obtained were different between the young and elderly groups. In particular, for the young subjects, two scans which together covered the entire brain were obtained. For the elderly subjects, because of the limited scan time available compared to the young subjects, only one scan which included the frontal and parietal regions was acquired. In addition to the T_2^*-weighted scans, within the same session, a magnetization-prepared 3D T_1-weighted gradient echo sequence was applied to obtain a whole brain scan of each participant. While the analysis was performed on T_2^*-weighted images, the T_1-weighted images were only used for registration purpose.

4.2.3 Overview

In this study, we propose a method for computing local cortical measures and subsequently using the computed measures for between-group comparisons. The flowchart of the presented method is depicted in Figure 4.1. The cerebral cortex was segmented using a

combination of T_2^*-weighted magnitude and phase images. Subsequently, an atlas was registered to the subject T_2^* space for parcellation of the cortex. Local GM/WM contrast and cortical profiles were then computed based on the cortex segmentation and the deformed atlas. This computation provided a common frame of reference for group-wise analyses. Statistical tests were carried out to study the differences in local GM/WM contrast and cortical profiles between two groups of subjects.

4.2.4 Pre-processing

Pre-processing of the T_2^*-weighted data consisted of four steps: intensity non-uniformity correction for the magnitude images, slab stitching for images of the young subjects, unwrapping for the phase images, and non-brain tissue removal. The N3 algorithm [82] was applied for non-uniformity correction of the magnitude images. Phase unwrapping was carried out by filtering in the *k*-space domain as proposed in [25]. The two scans of each young subject were stitched together to obtain a single whole brain volume using a rigid registration with three degrees of freedom (3 translations) on the magnitude images. Non-brain tissue removal was performed by a combination of thresholding and connected component analysis on both the magnitude and unwrapped phase data and was implemented according to [107].

4.2.5 Cortex segmentation

Segmentation of the cortex was performed using a combination of T_2^*-weighted magnitude and phase images as described previously [123]. The segmentation method was based on *K*-means clustering of magnitude and phase images. The outer contour of the cortex, i.e. cerebrospinal fluid (CSF)/GM interface, was detected using *K*-means clustering of the magnitude image. Subsequently, an initial inner contour, i.e. GM/WM interface, was determined by means of a minimum cost approach applied on the combined GM clusters of the magnitude and phase images and further refined to obtain the final cortex segmentation.

4.2.6 Registration

An atlas was registered to the subject T_2^*-weighted space for parcellation purposes using the elastix toolbox [85]. The T_1-weighted image of each subject and the MNI152 template [126] were used in an intermediate step during registration. In particular, the registration was carried out based on three transformations: (1) affine transformation from the atlas space to the MNI152 space, (2) affine transformation from the MNI152 space to the T_1-weighted space, and (3) rigid transformation (with 7 degrees of freedom) from the T_1-weighted space to the T_2^*-weighted space.

4.2.7 Parcellation

Local cortical measures were computed at parcellated cortical regions. The cortical parcellation was performed in the subject T_2^*-weighted space using the segmented cortex and the deformed atlas.

The atlas was deformed from its original space to the T_2^*-weighted space using the transformations computed previously and a nearest neighbour interpolator. Subsequently, the segmented cortex was parcellated into multiple regions using the deformed atlas as follows:

$$GM_i = S \cap l_i \tag{4.1}$$

where GM_i denotes the computed cortical GM region, S the binary mask of the cortex segmentation, and l_i the region with label i of the deformed atlas.

Furthermore, the WM region within l_i was defined as being adjacent to GM_i and identified as follows:

$$WM_i = \overline{GM_i} \cap l_i \cap M_{outer} \tag{4.2}$$

where M_{outer} denotes the outer mask.

4.2.8 Computation of local cortical measures

We examined between-group differences in GM/WM contrast and cortical profiles locally at each parcellated region. Local GM/WM contrast and cortical profiles were computed on both magnitude and phase images. The intensity of all magnitude images was normalized to the same range of $[0;1023]$ prior to the computation.

4.2.8.1 Local GM/WM contrast

The local GM/WM contrast Δ_i within region l_i was computed as the difference in average intensity or average phase value between GM_i and WM_i:

$$\Delta_i = \frac{1}{size(GM_i)} \sum_{x,y,z \in GM_i} I(x,y,z) - \frac{1}{size(WM_i)} \sum_{x,y,z \in WM_i} I(x,y,z) \tag{4.3}$$

where I denotes T_2^*-weighted magnitude or phase image.

Additionally, to provide information regarding homogeneity of the ROIs, we reported the standard deviation of the intensity or phase value within GM_i and WM_i.

4.2.8.2 Local cortical profiles

The cortical profiles were computed for each region l_i as follows. The outer mask M_{outer} was iteratively eroded using an elementary ball as the structuring element. At each iteration k, the outer contour C_k of the eroded mask was identified. The average phase value of all voxels that belonged to C_k and l_i on the phase image was computed as following:

$$p_{i,k} = \frac{1}{length(C_k \cap l_i)} \sum_{x,y,z \in (C_k \cap l_i)} I(x,y,z) \tag{4.4}$$

This computation resulted in a vector containing the average phase value at different iterations:

$$\boldsymbol{p} = [p_{i,1}, p_{i,2}, ..., p_{i,k}, ..., p_{i,K}] \tag{4.5}$$

where K was the maximum number of iteration, representing the maximum cortical depth considered and being set such that it was larger than the expected maximum value of cortical thickness (4.5mm) [127].

We defined d_i to be the distance (in voxels) between the outer and inner boundaries of the cortex in region l_i. The cortical phase profile $\boldsymbol{p_i}$ was composed of the first d_i elements of vector $\boldsymbol{p}$, where d_i was identified based on the gradient of vector $\boldsymbol{p}$, as following:

$$d_i = \arg\min_{k \in [1;K]} \nabla \boldsymbol{p}(k) \tag{4.6}$$

Since vector profile $\boldsymbol{p_i}$ contained not only information about the shape of the phase profile but also the mean phase value, in order to exclude the effect of possible differences

in the mean when investigating shape differences, we normalized $\boldsymbol{p_i}$ by subtracting its mean. The cortical profile was therefore determined as following:

$$\boldsymbol{p_i} = [p_{i,1}, p_{i,2}, ..., p_{i,d_i}] - \frac{1}{d_i} \sum_{k \in [1; d_i]} p_{i,k} \tag{4.7}$$

The cortical magnitude profile was computed similarly to the computation of cortical phase profile. Since the GM/WM contrast on the magnitude images of the elderly is decreased [29] while this contrast on the phase images does not appear to suffer from this aging effect, we used the value of d_i computed from the phase images in identifying the cortical magnitude profile. For data of the young subjects, even though the GM/WM contrast is more visible on the magnitude images of the young subjects compared to the elderly subjects, to avoid possible bias in statistical comparisons, we applied the same computation as used for the elderly subjects.

4.2.8.3 Local region selection

In this work, the Automated Anatomical Labeling (AAL) atlas [128], which contains in total 90 anatomical regions of interest, was used for cortical parcellation. Since the scans of the elderly had limited coverage compared to those of the young subjects and were affected by differences in brain size between subjects, we could only perform group comparison on a subset of the regions defined in this atlas. Local region selection was performed as follows. To ensure geometrical correspondence in group-wise comparison, a mask specifying the common coverage between two groups was identified in the atlas space by intersecting the coverage of all scans such that the common coverage contained data of at least 10 subjects per group. This mask was then used to determine the brain regions on which further analysis was carried out: a region l_i of the atlas was included if it contained more than 1cm^3 of both GM ($GM_i > 1\text{cm}^3$) and WM ($WM_i > 1\text{cm}^3$). In the computation of cortical profile, the values of d_i, identified using Eq. 4.6, outside the range of cortical thickness ([1mm; 4.5mm] [127]) were considered outliers and excluded from the analysis. Finally, we only performed statistical testing on a region if it had at least 10 samples per group to make sure that the results of the comparisons had sufficient statistical power. Based on the criteria described above, a set of 17 regions was selected for statistical testing.

4.2.9 Statistical testing

To check whether there was a difference in any parcellated region between the two groups, we performed statistical testing using the computed local GM/WM contrast and cortical profile. Since our original hypothesis was that any difference in a region was independent from that in other regions, we did not perform correction of the p values for comparisons at multiple regions in our statistical analyses.

4.2.9.1 Local GM/WM contrast

The difference in local GM/WM magnitude or phase contrast between the two groups was assessed using the Mann-Whitney U-test [129]. The Mann-Whitney U-test is a non-parametric test which makes no assumptions regarding data distributions and can be used to assess whether the mean of two groups are significantly different from each other. The test was carried out using MATLAB (Natick, MA, version 7.9.0) with a significance level of 0.05.

4.2.9.2 Local cortical profile

We compared the cortical magnitude or phase profiles between two groups using the permutation test which requires limited assumptions. This method has been employed for significance testing of waveform difference potentials [130] and successfully used in neuroimaging studies [131, 132].

Due to the inter-subject variability in cortical thickness, normalization for the length of cortical profiles was needed before performing the permutation test. For every region, vector cortical profile $\boldsymbol{p_i}$ was normalized such that its length was equal to the maximum value of d_i over all studied subjects using a spline interpolator.

When comparing the cortical profiles, there were two questions of interest:

Question 1: "are the shapes of cortical profiles obtained from two groups statistically different?"

Question 2: "at which cortical depths are there statistical differences between two groups?"

These questions were answered using two different permutation tests.

First, a permutation test was performed to check the overall null hypothesis for each cortical region: "the profiles of two groups are the same". This test addressed group-wise comparison considering the entire profile. The profiles of both groups were randomly permuted $10,000$ times. In each iteration, we computed a t statistic at every cortical depth and stored the highest value of the resulting statistics. This quantity was denoted as t_{val}. Similarly, we computed the statistic of the original group division, denoted as t_{orig}. After this computation, we obtained a vector $\boldsymbol{t}$, whose length was $(10,000+1)$, containing $10,000$ values of t_{val} and t_{orig}. The p value of the test was computed as following:

$$p = \frac{N}{N_{test}} \tag{4.8}$$

where N_{test} was the total number of group divisions: $N_{test} = 10,000+1$, and N was the total number of elements in vector $\boldsymbol{t}$ that were greater or equal to t_{orig}.

Second, for each cortical region, another permutation test was performed to check the null hypothesis "there is no difference between two groups at a specific cortical depth". In this test, the local difference at each cortical depth was assessed. The magnitude or phase values observed at a particular cortical depth were randomly permuted $10,000$ times. In each iteration, a t statistic (t_{val}) was computed and stored. The t statistic of the original group division (t_{orig}) was also computed. Consequently, a vector $\boldsymbol{t}$ consisting of $10,000$ values of t_{val} and the value of t_{orig} was obtained. The p value was computed as the ratio between the total number of statistics contained in vector $\boldsymbol{t}$ that were greater or equal to t_{orig} (N) and the total number of divisions ($N_{test} = 10,001$). This test was carried out for every cortical depth on the profile. Subsequently, the Bonferroni procedure was applied to correct for multiple comparisons. This resulted in a set of adjusted p values, one p value per cortical depth, which were used to accept or reject the null hypothesis.

We implemented the permutation tests in MATLAB and used 0.05 as the significance level.

4.3 Results

Figure 4.2 and 4.3 present maps of the p values obtained using local GM/WM contrast and cortical profiles on a parcellated cortex of an elderly subject. In these figures, the

images are color-coded based on the computed p values. The colour bar is scaled using log_{10} of the p values. For visualization purposes, all p values greater than the significance level of 0.05 are presented in blue to focus only on discriminative regions. Figure 4.4 shows the magnitude and phase profiles and the adjusted p values obtained at each cortical depth. In Table 4.1 and Table 4.2, we report the mean and standard deviation of the intensity or phase value within GM and WM ROIs as well as the p values of the U-test and permutation test. Table 4.1 presents the results obtained with the magnitude images and Table 4.2 presents the results obtained with the phase images.

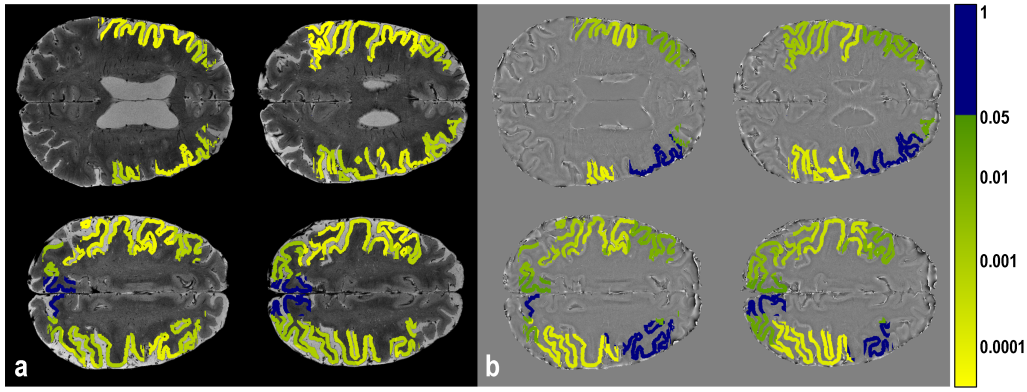


FIGURE 4.2: Map of p values obtained from the U-test on: (a) local magnitude GM/WM contrast, and (b) local phase GM/WM contrast.

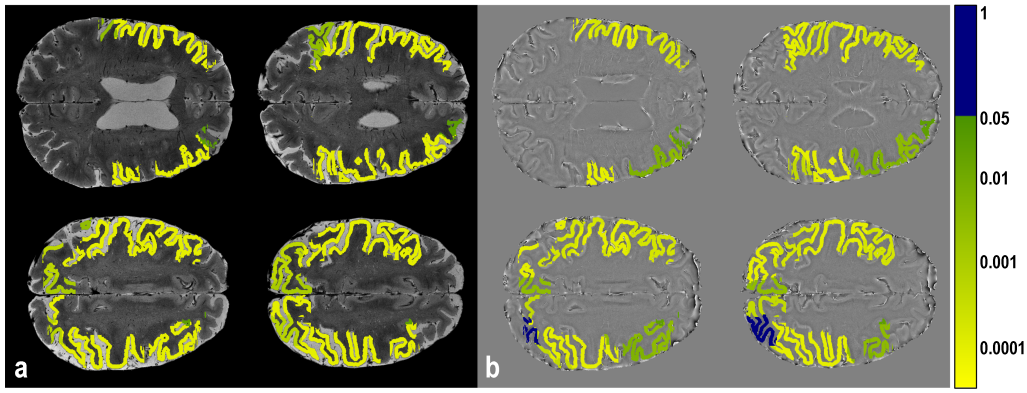


FIGURE 4.3: Map of p values obtained from the whole profile-based permutation test: (a) cortical magnitude profile, and (b) cortical phase profile.

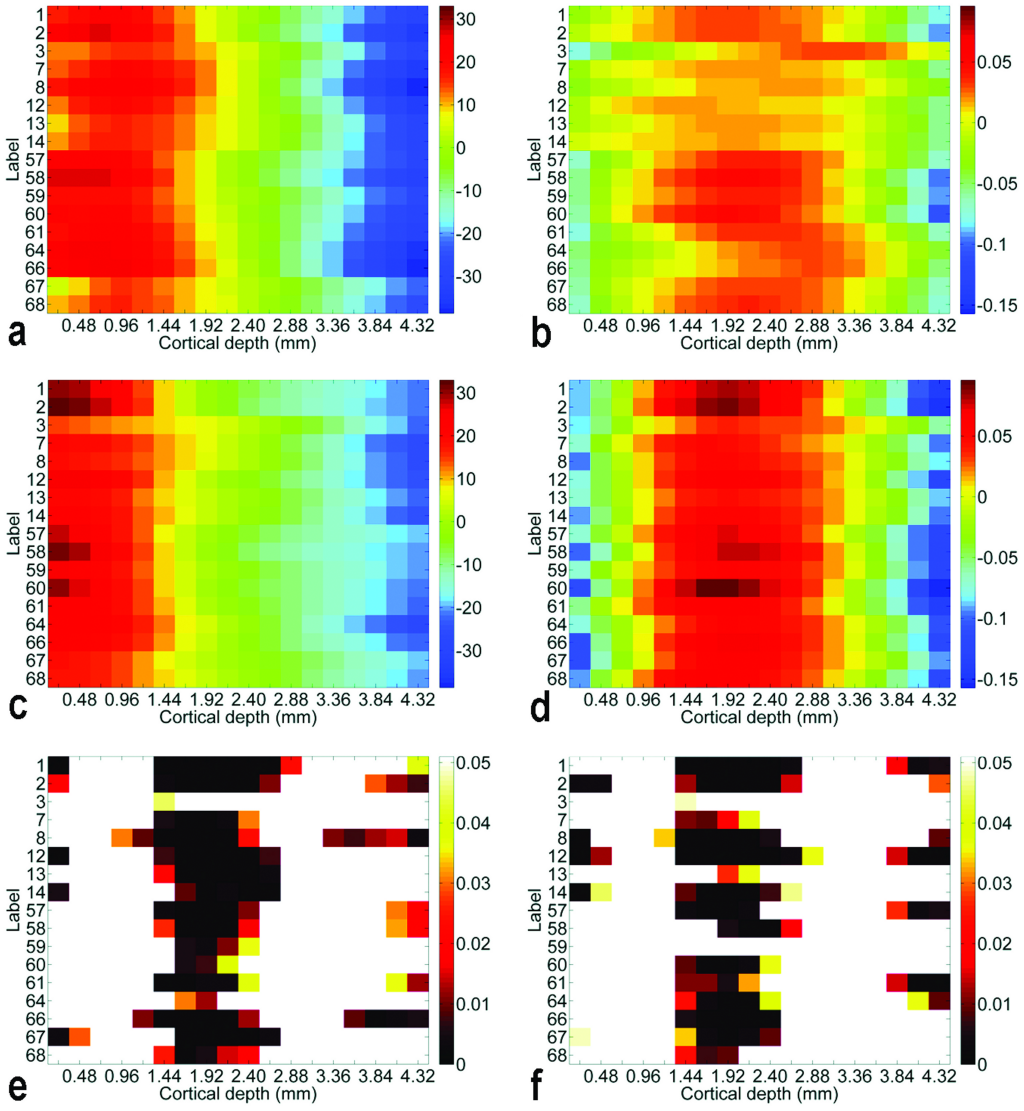


FIGURE 4.4: Visualization of the mean profiles within the cortex of all studied regions and the p values of the permutation tests: (a) magnitude and (b) phase profiles of the young group; (c) magnitude and (d) phase profiles of the elderly group; (e) adjusted p values obtained at each depth on the magnitude profiles and (f) adjusted p values obtained at each depth on the phase profiles. It should be noted that all individual profiles were used in the permutation tests to compute the p values; however in this figure, the mean cortical profiles are presented for illustration purposes.

TABLE 4.1: List of studied regions: the mean and standard deviation of the intensity within magnitude GM and WM ROIs of each label, p values obtained from the U-test on local magnitude GM/WM contrast and permutation test on entire magnitude profile comparison. Significant p values are in bold. L = Left, R = Right, std = Standard deviation.

Label	Anatomical region	Young				Eldely				p values of U-test using GM/WM contrast	p values of permutation test using the entire regional cortical profile
		GM		WM		GM		WM			
		Average mean	Average std	Average mean	Average std	Average mean	Average std	Average mean	Average std		
1	Precentral gyrus L	248	44	194	36	204	45	171	32	**2.8E-04**	**1.0E-04**
2	Precentral gyrus R	250	46	195	37	196	44	163	31	**1.8E-04**	**1.0E-04**
3	Superior frontal gyrus L	260	52	197	40	217	44	176	34	**6.5E-04**	**2.4E-02**
7	Middle frontal gyrus L	266	49	204	42	220	43	178	35	**6.5E-04**	**1.0E-04**
8	Middle frontal gyrus R	266	51	200	42	214	43	172	36	**6.5E-04**	**1.0E-04**
12	Inferior frontal gyrus, opercular part R	268	49	198	42	204	42	167	34	**7.3E-05**	**1.0E-04**
13	Inferior frontal gyrus, triangular part L	266	49	198	41	211	43	170	35	**9.2E-05**	**1.0E-04**
14	Inferior frontal gyrus, triangular part R	268	52	199	42	204	43	164	35	**5.8E-05**	**1.0E-04**
57	Postcentral gyrus L	238	47	192	33	204	44	174	32	**9.7E-04**	**1.0E-04**
58	Postcentral gyrus R	239	48	193	32	196	44	170	32	**9.2E-05**	**1.0E-04**
59	Superior parietal gyrus L	237	43	193	32	208	41	179	31	**2.1E-03**	**6.0E-04**
60	Superior parietal gyrus R	240	44	192	31	198	42	167	30	**2.2E-03**	**5.0E-04**
61	Inferior parietal gyrus L	246	43	196	33	215	41	184	31	**1.4E-04**	**1.0E-04**
64	Supramarginal gyrus R	259	49	193	39	212	41	170	32	**3.6E-05**	**2.8E-03**
66	Angular gyrus R	257	47	198	36	212	41	174	31	**7.2E-04**	**1.0E-04**
67	Precuneus L	242	45	201	37	212	43	178	35	2.8E-01	**1.0E-04**
68	Precuneus R	244	45	201	38	216	43	182	35	7.1E-02	**1.1E-03**

TABLE 4.2: List of studied regions: the mean and standard deviation of the intensity within phase GM and WM ROIs of each label, p values obtained from the U-test on local phase GM/WM contrast and permutation test on entire phase profile comparison. Significant p values are in bold. L = Left, R = Right, std = Standard deviation.

Label	Anatomical region	Young				Eldely				p values of U-test using GM/WM contrast	p values of permutation test using the entire regional cortical profile
		GM		WM		GM		WM			
		Average mean	Average std	Average mean	Average std	Average mean	Average std	Average mean	Average std		
1	Precentral gyrus L	0.082	0.316	-0.109	0.174	0.193	0.353	-0.067	0.213	**7.3E-05**	**1.0E-04**
2	Precentral gyrus R	0.081	0.325	-0.117	0.189	0.197	0.343	-0.073	0.225	**2.8E-04**	**1.0E-04**
3	Superior frontal gyrus L	0.008	0.548	-0.069	0.227	0.132	0.602	-0.032	0.240	**1.6E-02**	**2.2E-02**
7	Middle frontal gyrus L	0.047	0.409	-0.083	0.202	0.111	0.402	-0.047	0.218	6.3E-02	**3.3E-03**
8	Middle frontal gyrus R	0.028	0.396	-0.083	0.208	0.113	0.404	-0.044	0.226	**7.1E-03**	**2.0E-04**
12	Inferior frontal gyrus, opercular part R	0.046	0.333	-0.073	0.185	0.155	0.357	-0.058	0.208	**2.8E-04**	**1.0E-04**
13	Inferior frontal gyrus, triangular part L	0.063	0.423	-0.090	0.193	0.123	0.433	-0.049	0.209	2.3E-01	**6.0E-03**
14	Inferior frontal gyrus, triangular part R	0.023	0.438	-0.080	0.210	0.111	0.433	-0.054	0.232	**9.9E-03**	**2.0E-04**
57	Postcentral gyrus L	0.083	0.380	-0.107	0.193	0.210	0.354	-0.060	0.213	**1.4E-04**	**1.0E-04**
58	Postcentral gyrus R	0.077	0.377	-0.125	0.203	0.205	0.370	-0.068	0.222	**1.2E-03**	**2.0E-04**
59	Superior parietal gyrus L	0.127	0.365	-0.087	0.186	0.215	0.424	-0.036	0.238	**1.5E-02**	3.2E-01
60	Superior parietal gyrus R	0.129	0.372	-0.097	0.198	0.207	0.330	-0.073	0.202	**4.6E-03**	**1.0E-04**
61	Inferior parietal gyrus L	0.072	0.285	-0.092	0.172	0.205	0.310	-0.069	0.202	**1.4E-04**	**4.0E-04**
64	Supramarginal gyrus R	0.035	0.403	-0.090	0.205	0.163	0.381	-0.038	0.209	**1.7E-03**	**1.0E-04**
66	Angular gyrus R	0.063	0.325	-0.092	0.193	0.187	0.385	-0.033	0.213	**2.0E-02**	**1.0E-04**
67	Precuneus L	0.086	0.383	-0.092	0.210	0.153	0.402	-0.045	0.248	2.3E-01	**4.0E-04**
68	Precuneus R	0.083	0.341	-0.091	0.188	0.162	0.368	-0.047	0.230	**2.5E-02**	**3.1E-03**

The U-test on local magnitude GM/WM contrast revealed differences in 15 out of the 17 regions studied. No differences were found in the left or right precuneus. Differences were shown in 14 out of 17 regions using the U-test on local phase GM/WM contrast. No differences were found in the left middle frontal gyrus, left inferior frontal gyrus triangular part, or left precuneus. Significant differences were found in all studied regions by the permutation test on the entire cortical magnitude profiles. The permutation test on the entire cortical phase profiles showed highly significant differences in 16 out of 17 regions. No difference was found in the left superior parietal gyrus.

As can be seen in Figure 4.4, in traversing from the CSF/GM interface to the GM/WM interface, the magnitude profiles showed a decreasing intensity while the phase value increased up to the middle of the cortex and then decreased from there on. When comparing the young and elderly groups, Figure 4.4a and 4.4c show that the magnitude profiles of the young group were higher than those of the elderly group in the middle of the cortex. Conversely, at the same location of the cortex, Figure 4.4b and 4.4d show that the phase profiles of the young group were lower than those of the elderly group. These observations are corroborated by the p values presented in Figure 4.4e and 4.4f. Significant differences were found at the middle of the cortical ribbon for almost all regions for both magnitude and phase profiles. In addition, significant differences at the two tails of the profiles, near the CSF/GM interface and GM/WM interface, can also be observed, although to a lesser extent than differences in the middle cortex. A similar pattern of p values was obtained for both magnitude and phase profiles.

4.4 Discussion

In this study, we proposed a novel method for between-group comparison using local GM/WM contrast and cortical profile derived from 7T T_2^*-weighted magnitude and phase images. The proposed method was applied to compare young and elderly healthy subjects. The differences found are in line with existing literature and could be explained by changes in myelin and iron content in the cortical GM and WM as an effect of aging.

The differences found using the local magnitude GM/WM contrast suggest a change of this contrast as an effect of aging. This result is in accordance with findings in a previous study of Salat et al. [29]. Using T_1-weighted MPRAGE images, they reported strong changes in neural tissue signal properties with aging and that these changes statistically exceed any changes in morphometry such as cortical thinning. Stronger age-related effects on T_1-weighted MRI signal in the WM compared to GM resulting in reduced GM/WM contrast were also observed by Westlye et al. [133]. In terms of magnitude cortical profile, the profile of the young group (Figure 4.4a) started to decrease in the centre of the cortical ribbon, whereas in the elderly group (Figure 4.4c) this phenomenon took place at a location beyond the central location and closer to the CSF/GM interface. The pattern of p values presented in Figure 4.4e highlights the localized differences at this location. Similarly to the differences in local magnitude GM/WM contrast, this observation can be attributed to aging of the brain resulting in a decrease in GM intensity [29].

Using local phase GM/WM contrast, differences were shown in 14 out of 17 studied regions. Possible contributors to GM/WM contrast on the phase images include deoxy-hemoglobin, myelin, and iron content [134]. It was evident that deoxy-hemoglobin has no significant contribution to GM/WM phase contrast [135]. Recent studies have suggested that myelin content is the primary source of this contrast [134, 136]. Aging of healthy brain leads to changes in myelin content in the brain and affects both the

WM and GM [137–139]. Particularly, myelination follows roughly quadric trajectories, reaching a maximum at an age of ~45 and declining in older age [140, 141]. Cortical iron accumulation is another contributor to the observed contrast differences. Increased iron with advancing age in the cerebral cortex has been shown in histological studies [119]. Additional evidence on significant elevation of iron in the frontal cortex with aging comes from a study on DNA integrity [142].

Phase images have been used previously as an indirect measure of iron deposition [71]. It has been suggested that iron colocalizes with myelinated fibers not only in the WM but also in the GM and myelin-associated iron is the dominant source of intracortical magnetic susceptibility-based contrast [15]. In addition, myelin also varies across the cortex [72]. It can be observed from the cortical phase profiles in Figure 4b and 4d that the phase values are more spread over the cortical layer in the young group and more concentrated at the centre of the cortex in the elderly group. This observation indicates a difference regarding the distribution of myelin-associated iron over the cortex: more diffuse in the young group and more focal in the central thickness in the elderly group. Given the colocalization of ferritin iron and myelin within the cortex, it is speculated that the observed differences were linked to changes in both cortical iron and myelin due to aging.

When comparing the discriminative regions found using local GM/WM contrast and cortical profile, there are regions where the permutation test on the entire profiles showed differences while the U-test on GM/WM contrast did not (left and right precuneus on the magnitude images, and the left middle frontal gyrus, left inferior frontal gyrus triangular part, and left precuneus on the phase images), and vice versa (the left superior parietal gyrus on the phase images). This can be explained by the fact that local GM/WM contrast and cortical profile provide complementary information. The local GM/WM contrast is a scalar representing the difference in the mean value of GM and WM ROIs. Local GM/WM was used instead of the mean value of GM as it can compensate for any difference in magnitude or phase values which are not restricted to GM. Conversely, the cortical profile, normalized to exclude possible differences in the mean, is a vector representing how the magnitude or phase value varies across the cortical ribbon.

Local GM/WM contrast was computed based on the average intensity or phase value in GM and WM ROIs. As can be seen from Table 4.1, in the magnitude measures, intensity variation in the GM was approximately equivalent to the difference in mean intensity between GM and WM while the variation in WM was below this difference. In the phase measures, as presented in Table 4.2, the variation in the GM ROIs was larger than the GM/WM contrast, indicating a certain degree of phase heterogeneity within the ROIs. This heterogeneity is likely to be larger for larger ROIs and vice versa.

In this study, we evaluated our method using data of young and elderly healthy groups. A potential application of the method is the comparison between age-matched groups of patients with age-related neurodegenerative diseases such as Alzheimer's disease and healthy control subjects. It is known that GM/WM contrast on the magnitude images of the elderly is decreased with aging whereas this contrast on the phase images appears not to suffer from this effect [72]. Our approach makes use of the more consistent GM/WM contrast on the phase images in cortical parcellation and computation of the cortical profiles, and therefore is particularly useful for studies of elderly subjects. In this study, we chose to use the AAL structural atlas to parcellate the segmented cortex into multiple regions. The proposed method however is not bound to this atlas. One may choose to use

another atlas with predefined cortical areas depending on the specific applications, or use functional regions defined based on functional MRI.

Additionally, although the method was devised and tested using 7T data, we expect that it could be applied to high-resolution images obtained at 3T. This, however, should be confirmed by a further study using 3T data. It should also be noted that T_2^*-weighted magnitude and phase imaging benefits from increased image contrast and stronger susceptibility effects at increased field strengths [26, 31], and thus the proposed method would be more sensitive to between-group differences related to tissue susceptibility properties when carried out at 7T.

There were a few limitations of the study. Slightly different image acquisition schemes were used for the two groups. Only one T_2^*-weighted scan was acquired for each elderly subject, whereas two scans were acquired for each young subject. Signal variation due to motion may have an effect when combining the slabs of the young subjects. However, the two scans were acquired within the same section, right after each other with a quick pause in between. Visual inspection showed no considerable effect of rotation. Any 3D translation was compensated and intensity normalization was performed when stitching the slabs together. Regarding the geometrical correspondence of the scan coverage between groups, each elderly scan was positioned at the middle of the brain such that it included the parietal and frontal lobes, resulting in the coverage of this scan intersecting with that of both scans in the young subjects. The use of both scans for the young subjects in this study therefore led to more ROIs to be analysed in group-wise comparison.

Statistical testing was only performed on a subset of cortical regions due to the difference in data coverage between young and elderly subjects. When performing local region selection, for each region, an inclusion criterion concerning the size of GM and WM ROIs was applied to minimize the effect of noise on the measurements. Another criterion was applied on the values of local distance between CSF/GM and GM/WM interfaces (d_i) to detect outliers. Visual inspection of the outliers revealed inaccurate positioning or missing the outer contour locally at a few cortical regions which led to inaccurate identification of the GM/WM interface. This was possibly caused by the lack of CSF voxels on the magnitude images that the segmentation algorithm was based on to detect the outer contour.

Image phase is known to be dependent on geometry and orientation relative to the B_o magnetic field. The effect of this dependency on between-group comparison was minimized by careful positioning of all subjects in the same manner. Another limitation is the non-local relation between the measured phase values and the underlying tissue susceptibility. Recently, quantitative susceptibility mapping (QSM) techniques [143, 144] have been proposed to compute quantitative susceptibility map by solving the inverse magnetic field to susceptibility source problem. These techniques require that the phase images are obtained from a 3D sequence. The data in this study were acquired using 2D GRE sequence and therefore are not suitable for the application of QSM. Nevertheless, in principle, given a susceptibility map computed using QSM, local GM/WM contrast and cortical profile can be derived from the susceptibility map based on the presented method.

4.5 Conclusions

We have presented a novel method for quantification of local cortical changes using 7T T_2^*-weighted magnitude and phase images. We applied the method to compare young and elderly subjects. Using local phase and magnitude GM/WM contrast, differences were

shown in 14 and 15 out of 17 studied regions, respectively. Localized differences in phase and magnitude profiles were revealed in 16 and 17 regions, respectively. The results of this study show that the proposed method can be a useful tool to study cortical changes in normal aging and may also be useful in studies of neurodegenerative diseases.

4.6 Acknowledgements

This research was performed within the framework of CTMM, the Center for Translational Molecular Medicine (www.ctmm.nl), project LeARN (grant 02N-101).

5

Cortical analysis using 7T MR phase images reveals regional differences between early and late onset Alzheimer's disease

This chapter was adapted from:

S. van Rooden*, **N. T. Doan***, M. J. Versluis, J. D. C. Goos, A. G. Webb, A. M. Oleksik, W. M. van der Flier, P. Scheltens, A. W. E. Weverling - Rynsburger, F. Barkhof, G. J. Blauw, J. H. C. Reiber, M. A. van Buchem, J. Milles, and J. van der Grond, "Cortical analysis using 7T MR phase images reveals regional differences between early and late onset Alzheimer's disease," Submitted, * share first authorship

Abstract

The overall aim of the present study is to explore regional iron related differences possibly indicative for AD pathology in the cerebral cortex between early (EOAD) and late onset Alzheimer's disease (LOAD) patients using 7T MR phase images. High resolution T_2^*-weighted scans were acquired in 12 EOAD and 17 LOAD patients at 7T MRI. Lobar peak phase shifts, regional phase contrasts, and cortical profiles were computed from the phase images in different cortical regions to compare the EOAD and LOAD groups. An increased peak phase shift was found for the whole brain in EOAD patients compared to LOAD patients ($p = 0.005$). The regional phase contrast in EOAD patients was higher than in LOAD patients in the middle frontal gyrus, postcentral gyrus, superior parietal gyrus, inferior parietal gyrus and precuneus ($0.002 < p < 0.042$). EOAD patients had a different cortical layer pattern in the middle frontal gyrus, precentral gyrus, postcentral gyrus, superior parietal gyrus, and precuneus compared to LOAD patients ($0.005 < p < 0.050$). These data suggest that patients with EOAD have an increased iron accumulation possibly related to increased amyloid deposition in specific cortical regions as compared to LOAD patients.

5.1 Introduction

Alzheimer's disease (AD) is a very common form of dementia and prevalence is increasing rapidly [145, 146]. Although age is one of the main risk factors for the development of AD, AD may also develop in younger patients, often referred to as early onset AD (EOAD). Previous studies have demonstrated that EOAD patients show a different profile of cognitive impairment and more rapid cognitive decline compared to late onset AD (LOAD) patients [147–152]. EOAD patients exhibit atypical non-amnestic symptoms more often than LOAD patients, leading to an incorrect clinical diagnosis in one-third of the EOAD cases [153, 154]. Although EOAD patients share multiple characteristics with LOAD patients, several studies have shown differences between the two groups with respect to the pattern and severity of atrophy [155, 156] as well as the pattern and severity of disturbances in metabolism [157–159], any or all of which might account for the differences in cognition [160, 161].

Neuropathological studies have shown that EOAD patients show more neuritic plaques and neurofibrillary tangles than LOAD patients [162–164]. However, these findings have not been substantiated in clinical studies. Studies using Positron Emission Tomography (PET) with carbon-11-labelled Pittsburgh compound-B (PiB) were not conclusive in replicating the post-mortem findings. In two studies, the reported overall amyloid burden did not differ between EOAD and LOAD patients [158, 159], whereas in another study, higher amyloid burden was shown in EOAD patients compared to LOAD patients [165]. A more recent PET study showed a regional increased amount of amyloid burden within the parietal cortex as opposed to an overall increase in the whole brain in EOAD patients in comparison to LOAD patients [158].

Recently, high resolution T_2^*-weighted high field MRI was used to highlight indirect cortical changes due to differences in iron accumulation related to amyloid deposition in vivo [125, 166]. A previous study suggested that iron accumulation, which may reflect AD pathology and more specifically amyloid deposition, is reflected by the phase information from a T_2^*-weighted MRI sequence at 7T MRI and measurement of the relative phase in regions of interest demonstrated a high specificity with respect to AD detection [125]. In contrast to PiB-PET, which is based on an in-plane resolution of 2 x 2 mm^2, the high resolution high field MRI approach uses images with an in-plane resolution of 0.24 x 0.24 mm^2, allowing accurate and detailed detection of phase changes, even within cortical layers [167].

The overall aim of the present study was to explore regional differences in AD based on phase information, which may reflect AD pathology, in the cerebral cortex between EOAD and LOAD patients using 7T MR phase images. In particular, group differences in lobar phase shift, cortical contrast and the layer pattern within the cortex at local cortical regions were investigated.

5.2 Materials and methods

5.2.1 Participants

This study was approved by the local institutional review board. In all cases, informed consent was obtained according to the declaration of Helsinki [168]. In total 17 LOAD patients (age > 67 years) with a mean age of 76.4 years (range 68 to 86 years, 11 male/6 female) and 12 EOAD patients with a mean age of 62.2 years (range 51 to 67 years, 7 male/5 female) were included.

The AD patients were recruited from the memory clinic of the Leiden University Medical Center, the VU University Medical Center in Amsterdam, the Bronovo Hospital in The Hague and the Diaconessen Hospital in Leiden. Memory clinic patients were referred to the hospital by their general practitioner or a medical specialist. Prior to the 7T study, all patients underwent a routine clinical protocol, comprising a whole brain MRI, a battery of neuropsychological tests, and a general medical and neurological examination performed by a neurologist, psychiatrist or internist-geriatrician. The diagnosis was made in a multidisciplinary consensus meeting using the NINCDS-ADRDA criteria for diagnosing probable Alzheimer's disease [169]. Participants with the diagnosis "probable AD", who were capable of giving informed consent (Mini Mental State Examination (MMSE) ≥ 19) were selected for inclusion in the 7T study either retrospectively within one year after attending the memory clinic, or prospectively.

5.2.2 MR acquisition

MRI was performed on a whole body human 7T MR system (Philips Healthcare, Best, the Netherlands) using a quadrature transmit and 16-channel receive head coil (Nova Medical, Wilmington, MA, USA). Participants were scanned using a 2D flow-compensated transverse T_2^*-weighted gradient-echo scan including the frontal and parietal regions, which are most prone for amyloid deposition, with a total imaging duration of 10 minutes. Positioning of this stack was performed using the sagittal plane of the survey within the frontal and parietal region above the occipital lobe. The middle of the stack was positioned through the corpus callosum, just above the thalamus. Imaging parameters were: repetition time (TR)/echo time (TE) 794/25 ms, flip angle 45^o , slice thickness 1.0 mm with a 0.1 mm interslice gap, 20 slices, 240 x 180 x 22 mm^3 field of view, 1000 x 1024 matrix size, resulting in an in-plane nominal spatial resolution of 0.24 x 0.24 mm^2. The band width per pixel was 46 Hz, corresponding to a readout length of approximately 22 ms. The frequency and phase encoding directions were along the anterior-posterior and right-left axes, respectively. These sequences are very sensitive to image artifacts arising from resonance frequency fluctuations within the brain caused by slight patient movements, even in areas significantly away from the head. A navigator echo was included to correct for these artifacts [114]. Shimming up to third order was performed using an image based shimming approach [170]. The phase images were subsequently unwrapped by high-pass filtering with a 92x92 kernel size [171].

5.2.3 Image analysis

5.2.3.1 Lobar peak phase shift measurements

As in a previous study, phase values in the cortex were determined using the transverse 2D T_2^*-weighted gradient echo scans. The peak phase values of the cortical gray matter (GM) were determined on the unwrapped phase images in regions of interest (ROIs) in four different areas of the brain: frontal, left temporoparietal, right temporoparietal and parietal [125]. The overall peak-to-peak phase shift (expressed in radians) between cortical gray and subcortical white matter (WM) (lobar cortical phase shift) was calculated for each region in each subject.

5.2.3.2 Regional GM/WM phase contrast

The regional GM/WM phase contrast was measured in more localized cortical regions using the method presented in [167]. The cerebral cortex was segmented using a

combination of T_2^*-weighted magnitude and phase information as described in [123]. An atlas with labels of predefined cortical ROIs (AAL atlas [128]) was then registered to the subject T_2^*-weighted image for cortical anatomical parcellation (Figure 5.1b). For each atlas label (Figure 5.1c), cortical GM and subcortical WM ROIs on the phase images were identified with the GM ROI being the intersection between the segmented cortex and the binary mask of the label, and the WM ROI located within the label and adjacent to the GM ROI. The regional GM/WM contrast was computed as the difference between the mean phase value of the GM and WM ROIs.

5.2.3.3 Regional cortical phase profile

A cortical phase profile (Figure 5.1d) representing the distribution of the phase value across the cortical layer [167] was calculated for each atlas label. The outer mask, bordered by the outer cortical contour, was iteratively eroded. For each iteration, the mean phase value of voxels positioned both in the contour of the eroded mask and the particular label was computed, resulting in one node of the profile (see Figure 5.1). The length of the profile was determined as the local distance between the cerebral spinal fluid (CSF)/GM and GM/WM interfaces on the phase images. The mean phase value of the corresponding WM ROI was subtracted from the profile to correct for local RF coil inhomogeneity.

To minimize the effect of noise on the measurements, the regional GM/WM contrast and cortical profile for labels were computed only when both GM and WM ROIs satisfied a size criterion ($\geq 1\text{cm}^3$). Finally, statistical testing was only performed on labels having data from at least 10 subjects to ensure sufficient statistical power.

5.2.4 Statistics

A Mann-Whitney U-test was used to assess the difference in MMSE and a chi-square test was used to assess the difference in gender between groups. In this study, we used MMSE score as a measure of the disease severity. Linear regression analysis was used to assess the association between early and late age-at-onset and lobar peak phase shift measurements in the four different lobar regions of the cortex, adjusted for gender and disease severity (MMSE).

Linear regression analysis adjusted for gender and disease severity (MMSE) was also used to assess group differences in regional GM/WM contrast. To compare the cortical profiles, two different permutation tests were used. Due to possible differences between subjects in cortical thickness, the cortical profiles were normalized to have the same length prior to the permutation tests. The first permutation test checked whether there was a difference between two groups considering the entire profile, resulting in one p value per comparison. The second permutation test was more localized. It was performed at each cortical depth, resulting in one p value per node of the profile. The resulting p values were then adjusted for the total number of nodes using the False Discovery Rate (FDR) procedure.

Permutation tests were carried out using Matlab (Natick, MA, version 7.14). All other statistical analyses were performed with the Statistical Package of Social Sciences (SPSS, version 17.0.1; SPSS, Chicago, Ill). A significance level of 0.05 was used.

5.3 Results

Characteristics of the participants are shown in Table 5.1. Age was 76.4 ± 5.9 years in the LOAD group and 62.2 ± 5.2 years in the EOAD group. No difference in gender and MMSE was present between the EOAD and LOAD groups.

Figure 5.1 shows a representative transverse T_2^*-weighted phase image of the cortex of a subject (Figure 5.1a) and an illustration of cortical parcellation (Figure 5.1b) as well as the computation of regional cortical profiles (Figure 5.1c-d). Table 5.2 shows the lobar peak phase shifts of the frontal, temporoparietal, parietal cortex and the whole brain. For all of these regions, a larger cortical phase shift ($p < 0.05$) was found in the EOAD patient group compared to the LOAD patient group which was associated with age-at-onset (adjusted for gender and disease severity).

Table 5.3 reports the mean regional GM/WM contrast computed from the EOAD and LOAD groups in 18 studied regions as well as the p values obtained from the statistical comparisons between the two groups in terms of regional GM/WM contrast and cortical profile. The p values obtained from linear regression analysis (adjusted for gender and disease severity) and from the permutation test using the entire profile are color-mapped on the cortex of an EOAD patient in Figure 5.2a-b. Linear regression analysis (adjusted for gender and disease severity) showed significant differences in regional GM/WM contrast in the left middle frontal gyrus, right postcentral gyrus, left and right superior parietal gyrus, right inferior parietal gyrus, and left and right precuneus. The EOAD group consistently showed higher mean GM/WM contrast than the LOAD group.

When comparing the cortical phase profile, significant differences were found in the left middle frontal gyrus, right precentral gyrus, right postcentral gyrus, left and right superior parietal gyrus, and left and right precuneus (Table 5.3, Figure 5.2b). Figure 5.3 presents the mean cortical phase profile of each group at each region studied (Figure 5.3a-b) and the p values obtained at each node before and after the FDR correction for the total number of nodes (Figure 5.3c-d). As can be observed from Figure 5.3a-b, the cortical phase profiles of both groups are bell shaped. The profile of the EOAD group however exhibits larger amplitudes than the LOAD group. The p values presented in Figure 5.3c-d specify the cortical depths where the EOAD group shows significantly larger phase values than the LOAD group. Before multiple comparison correction, differences were shown at multiple nodes on the cortical profile of the left middle frontal gyrus, left inferior frontal gyrus opercular part, right precentral gyrus, right postcentral gyrus, left and right superior parietal gyrus, right inferior parietal gyrus and left and right precuneus. In most of these structures, the differences were most significant at the cortical layers between the CSF/GM interface and the middle of the cortex. After correction, significant differences were shown in the left and right superior parietal gyrus as well as left and right precuneus.

TABLE 5.1: Characteristics of early and late onset AD patients. EOAD = early onset Alzheimer's disease, LOAD = late onset Alzheimer's disease, MMSE = Mini Mental State Examination.

	EOAD (n = 12)	LOAD (n = 17)
Mean age, years (range)	62.2 (51–67)	76.4 (68–86)
Male/female	7/5	11/6
Median MMSE, points (range)	22 (19–26)	23 (19–26)

TABLE 5.2: Mean lobar phase shifts (in radians) and SDs of the brain lobes in early and late onset Alzheimer's disease patients. p values were obtained using linear regression analysis adjusted for gender and disease severity. EOAD = early onset Alzheimer's disease, LOAD = late onset Alzheimer's disease, asterisks indicate significant differences.

	EOAD (n = 12)	LOAD (n = 17)	p value
Frontal	1.15 ± 0.09	1.04 ± 0.11	0.014*
Temporoparietal left	1.25 ± 0.05	1.18 ± 0.09	0.029*
Temporoparietal right	1.31 ± 0.09	1.23 ± 0.10	0.045*
Parietal	1.27 ± 0.08	1.16 ± 0.10	0.006*
Total	1.25 ± 0.06	1.15 ± 0.09	0.005*

TABLE 5.3: The mean regional gray matter/white matter phase contrast computed for both groups and the p values obtained by linear regression analysis (adjusted for gender and disease severity) using this measure and permutation test using the entire cortical profile. GM = gray matter, WM = white matter, L = left, R = right, EOAD = early onset Alzheimer's disease, LOAD = late onset Alzheimer's disease, asterisks indicate significant differences.

Lobe	Structure	GM/WM contrast (rad)		p value Linear regression	p value Permutation test
		EOAD	LOAD		
Frontal	Superior frontal gyrus L	0.165 ± 0.057	0.166 ± 0.090	0.844	0.720
	Superior frontal gyrus R	0.167 ± 0.078	0.149 ± 0.087	0.688	0.849
	Middle frontal gyrus L	0.199 ± 0.035	0.144 ± 0.049	0.005*	0.050*
	Middle frontal gyrus R	0.197 ± 0.045	0.160 ± 0.049	0.072	0.203
	Inferior frontal gyrus, opercular part L	0.225 ± 0.044	0.180 ± 0.074	0.169	0.114
	Inferior frontal gyrus, opercular part R	0.237 ± 0.031	0.227 ± 0.048	0.656	0.425
	Inferior frontal gyrus, triangular part L	0.196 ± 0.035	0.160 ± 0.051	0.051	0.164
	Inferior frontal gyrus, triangular part R	0.199 ± 0.028	0.169 ± 0.058	0.126	0.186
Temporoparietal	Precentral gyrus L	0.274 ± 0.047	0.236 ± 0.086	0.220	0.170
	Precentral gyrus R	0.310 ± 0.041	0.287 ± 0.072	0.415	0.035*
	Postcentral gyrus L	0.277 ± 0.052	0.247 ± 0.052	0.165	0.156
	Postcentral gyrus R	0.288 ± 0.030	0.252 ± 0.044	0.025*	0.028*
Parietal	**Superior parietal gyrus L**	0.305 ± 0.045	0.245 ± 0.035	0.004*	0.005*
	Superior parietal gyrus R	0.284 ± 0.031	0.248 ± 0.034	0.020*	0.037*
	Inferior parietal gyrus L	0.273 ± 0.033	0.255 ± 0.038	0.210	0.405
	Inferior parietal gyrus R	0.293 ± 0.041	0.246 ± 0.043	0.042*	0.063
	Precuneus L	0.249 ± 0.052	0.191 ± 0.044	0.007*	0.008*
	Precuneus R	0.241 ± 0.026	0.190 ± 0.036	0.002*	0.007*

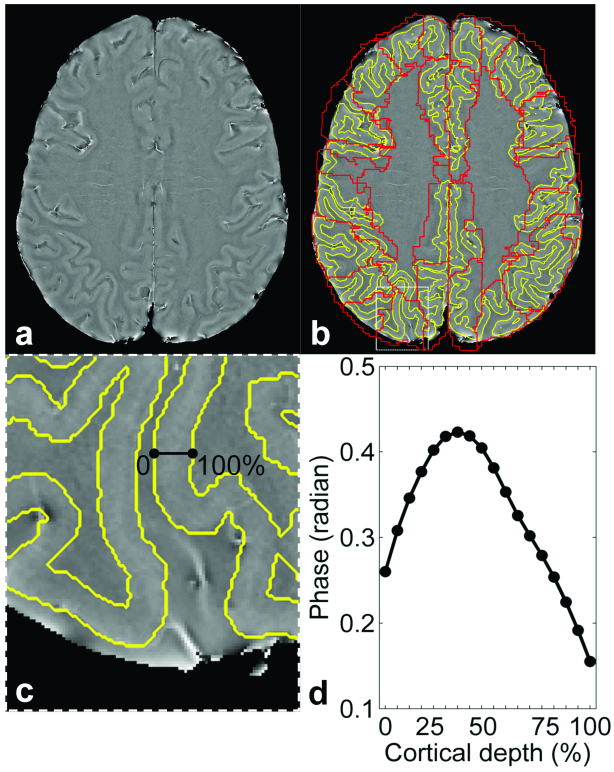


FIGURE 5.1: Illustrative example of cortical parcellation and the computation of regional cortical profiles: (a) representative transverse 2D T_2^*- weighted gradient echo phase image (in-plane spatial resolution is 0.24 x 0.24 mm^2); (b) contours of the segmented cortex (in yellow) and of the labels as defined in the AAL atlas (in red) overlaid on the phase image; (c) magnified cortical ROI; (d) the cortical phase profile computed for the superior parietal region located within the ROI presented in (c).

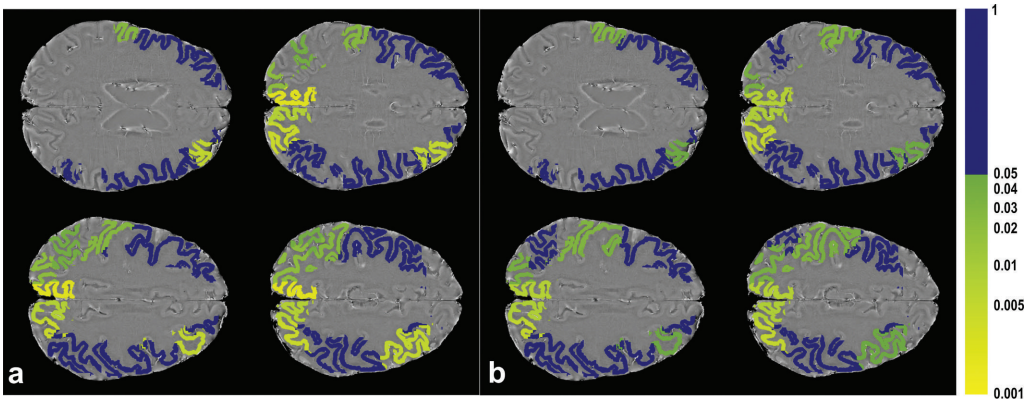


FIGURE 5.2: Maps of p values on the cortex of an early onset AD patient: (a) linear regression analysis (adjusted for gender and disease severity) on regional GM/WM contrast, and (b) permutation test on entire cortical profile. All p values > 0.05 are presented in blue, and the color bar is scaled using $-\log_{10}(p \text{ values})$ otherwise. Only the cortical regions included in this study were presented.

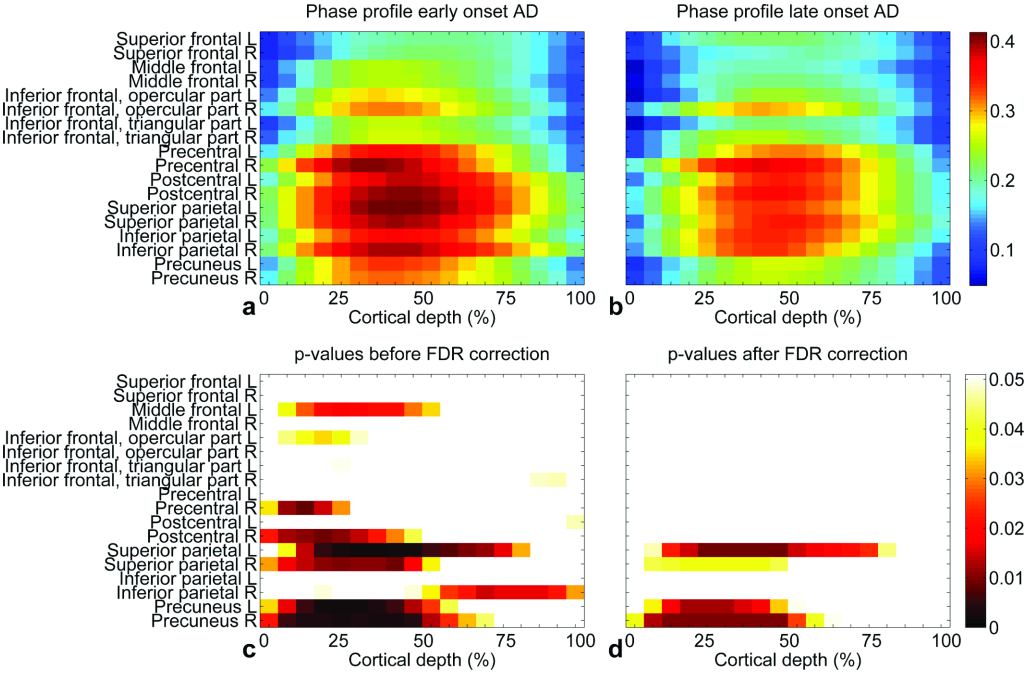


FIGURE 5.3: Cortical phase profiles and the p values obtained using a permutation test at each cortical depth: (a) profile of early onset AD, (b) profile of late onset AD, (c) p value before FDR correction for the number of nodes on the profile, and (d) p values after the FDR correction. The color map in (a) and (b) presents the phase values in radians. The hotter the color, the higher the phase value and vice versa. A cortical depth of 0% corresponds to the CSF/GM interface and 100% the GM/WM interface.

5.4 Discussion

This study shows that using 7T MRI phase images, global (i.e. per lobe) and regional differences in the cortex, as well as differences within the cortical layers, can be detected between EOAD and LOAD patients in great detail. Measurement of the lobar peak phase shift demonstrated a higher phase shift throughout the whole brain in EOAD patients compared to LOAD patients independent of the disease severity. Within the four lobar cortical regions studied, a higher cortical phase shift of the frontal, temporoparietal and parietal regions was associated with an early age-at-onset. Previous studies in brain specimens of AD patients have shown that amyloid deposition and neurofibrillary tangles as well as tau deficiency co-localize with neuronal iron accumulation [98, 172–174]. The relative phase in cortical regions of interest can be used as an indicator of iron in the brain [26, 124, 175, 176], which opens up the possibility to measure neuronal iron co-localized with AD pathology. Previously, it was demonstrated that AD pathology and more specifically amyloid deposition is indirectly reflected by the phase information from a T_2^*-weighted MRI sequence [125]. In this respect, the in-vivo data presented in this study confirm the previous histological and in-vivo studies which reported that EOAD patients show more amyloid plaques and tangles than LOAD patients [162–165]. Therefore, the finding of an overall increased phase shift in EOAD patients compared to LOAD patients suggests that AD pathology, and more specifically amyloid deposition, is more severe in the EOAD patients. Measurement of the regional phase contrast showed higher phase values in EOAD patients compared to LOAD patients in the middle frontal gyrus, postcentral gyrus, superior parietal gyrus, inferior parietal gyrus and precuneus independent of disease severity. The finding of an increased regional phase contrast mainly in the parietal sub-regions is in accordance with a recent PET-PiB study which shows a higher amyloid burden in the parietal lobe in EOAD patients in comparison with LOAD patients [158]. Moreover, we also found an increased regional phase contrast in the middle frontal gyrus which confirms an earlier neuropathological study showing a higher amount of amyloid plaques in EOAD patients compared to LOAD patients in the parietal and frontal regions [162]. Previous studies have shown that the precuneus, posterior cingulate gyrus, parietal and frontoparietal regions in EOAD patients also show more atrophy than in LOAD patients [155, 156, 160, 177–179]. This might imply a direct association between severity of AD pathology and atrophy in EOAD patients.

The overall cortical layer pattern also showed differences between EOAD and LOAD patients in the middle frontal gyrus, precentral gyrus, postcentral gyrus, superior parietal gyrus, and precuneus. The phase profiles showed higher phase values in the EOAD patients compared to LOAD patients. In the superior parietal gyrus and precuneus, significant differences within the cortical layers between the CSF/GM interface and the middle of the cortex could be detected between EOAD and LOAD patients. A previous study showed that the contrast between different cortical layers using high-field MRI T_2^*-weighted sequences and phase images is based on differences in iron and myelin content between different layers [72, 180]. The current results imply that the distribution of iron and/or myelin is different in the cortical layers close to the CSF/GM interface in the superior parietal gyrus and precuneus between the two groups, with the EOAD patients showing higher amounts of iron/ demyelination.

The precuneus and superior parietal gyrus were the only structures showing a significant difference in mean phase contrast and cortical profile at very specific cortical

depths. Previous studies have demonstrated that the precuneus and parietal cortex show more atrophy [156, 178, 179, 181] and more severely impaired metabolism [159, 182] in EOAD patients than in LOAD patients. Our results indicate that within the precuneus and the superior parietal gyrus more iron and/or less myelin is present, which may reflect increased AD pathology resulting in a change of the cortical layer pattern and phase contrast. This is in line with the notion that these structures play an important role in the development of EOAD, or alternatively that EOAD is a different subtype of AD characterized by pathological changes of the precuneus and superior parietal gyrus.

One overall limitation of the study is that phase measurements may be influenced by the geometry and orientation of the individual structures [26]. To limit such effects as much as possible, all participants were positioned in the same manner, and for every subject, the phase measurements were performed in the same way and were averaged to cancel out the possible effects of geometry and orientation. A second limitation is the small number of subjects and the absence of a healthy control group. However, it is very unlikely that our results were related to an age effect as with healthy aging an increased phase shift would be expected due to a slight increase in cortical iron and demyelination with aging [119, 183, 184]. Instead, we found an increased phase shift in the EOAD patients. Moreover, the source of the observed differences in phase contrast and cortical profile is not completely clear. Although it is most likely that the difference in phase contrast and profile between groups is mainly attributable to iron, other compounds may contribute to a change in phase contrast, such as deoxy-hemoglobin, myelin and proteins [185]. The effect of deoxy-hemoglobin is expected to be rather small in comparison with iron and myelin [72]. Myelin and proteins might explain part of the results in our study, although very few studies have investigated the differences in these substances between EOAD and LOAD patients [186, 187] and therefore it is difficult to verify what their influence has been. Future research should focus on studying the correlation between histology and MR images to confirm that the differences in phase contrast and profile between LOAD and EOAD patients is due to AD pathology.

In conclusion, in this study, using 7T MRI phase information, regional cortical differences in contrast and layer pattern were detected in EOAD versus LOAD patients, indicating regionally more severe iron accumulation possibly due to amyloid deposition in EOAD compared to LOAD patients.

5.5 Acknowledgement

This research was performed within the framework of CTMM, the Center for Translational Molecular Medicine (www.ctmm.nl), project LeARN (grant 02N-101). The authors thank Mrs. G. Labadie for her help in recruiting, interviewing and planning all the participants.

6

Deformation texture-based features for classification in Alzheimer's disease

This chapter was adapted from:

N. T. Doan, B. van Lew, B. P. F. Lelieveldt, M. A. van Buchem, J. H. C. Reiber, and J. Milles, "Deformation texture-based features for classification in Alzheimer's disease," Medical Imaging 2013: Image Processing, Sebastien Ourselin, David R. Haynor, Editors, Proc. SPIE 8669, 866927 (2013).

Copyright 2013 Society of Photo-Optical Instrumentation Engineers. One print or electronic copy may be made for personal use only. Systematic electronic or print reproduction and distribution, duplication of any material in this paper for a fee or for commercial purposes, or modification of the content of the paper are prohibited.

Abstract

Neurological pathologies are often reflected in brain magnetic resonance images as abnormal global or local anatomical changes. These variations can be computed using non-rigid registration and summarized using Jacobian determinant maps of the resulting deformation field, which characterise local volume changes. We propose a new approach which exploits the information contained in Jacobian determinant maps of the whole brain in Alzheimer's disease (AD) classification by means of texture analysis. Textural features were derived from whole-brain Jacobian determinant maps based on 3D Grey Level Co-occurrence Matrix. The large number of features obtained depicts anatomical variations at different resolution, allowing retaining both global and local information. Principle component analysis was applied for feature reduction such that 95% of the data variance was retained. Classification was performed using a linear support vector machine. We evaluated our approach using a bootstrapping procedure in which 92 subjects were randomly split into separate training and testing sets. For comparison purposes, we implemented two dissimilarity-based classification approaches, one based on pairwise registration and the other based on registration to a single template. Our new approach significantly outperformed the other approaches. The results of this study showed that pairwise registration did not bring added value compared to registration to a single template and textural features were more informative than dissimilarity-based features. This study demonstrates the potential of texture analysis on whole brain Jacobian determinant map for diagnosis of AD subjects.

6.1 Introduction

Alzheimer's disease (AD) is the most common cause of dementia. Much research using magnetic resonance imaging (MRI) has been carried out to derive biomarkers for early detection of the disease. Studies based on volumetric and shape analysis have reported abnormalities for AD patients in structures such as the hippocampus, cortex [62], thalamus, putamen [63], amygdala [64] and ventricle [65]. Volumetric and shape analyses require the determination of structures of interest, as well as their accurate segmentation, and consider changes occurring within them only in a very global manner. As a result, these approaches are only tractable in a hypothesis-driven framework and are not capable of detecting local changes internal to structures, which may precede volume or shape changes.

To alleviate those issues, segmentation-less methods using image-based registration have been devised. Deformation-based morphometry is a popular approach for detecting group differences using non-rigid registration algorithms [66, 188]. The Jacobian determinant map, computed from the deformation field, is particularly useful as it characterises local volumetric compression or expansion. Klein et al. proposed to use the dissimilarity measure computed from the logarithm of the Jacobian determinant map as a potential measure allowing early diagnosis of dementia [67]. However, this approach requires pairwise registration between subjects and only yields one global measure for each pair of subjects. This method thus uses a very computationally intensive step to generate a feature matrix containing global measures of the deformation between subjects.

In this study, we propose a new approach based on Jacobian determinant maps in a classification framework, which alleviates the computationally intensive aspects of the method proposed by Klein and colleagues. After deforming all subjects to a single template, we apply texture analysis on the Jacobian determinant map to study patterns of volumetric changes over the entire brain and use them to classify healthy controls and AD patients. This approach allows taking into account not only global deformations, but also more local characteristics as it results in a large number of textural features from which the most descriptive variations can be selected for classification purposes. Moreover, it only requires registration to a common template instead of pairwise registration over the whole dataset. This approach, which involves global and local information, could potentially allow the differentiation of neurological pathologies based on MR image data. We further evaluate our method using MR data of controls, mild-cognitively impaired (MCI) subjects and AD patients obtained from the OASIS database [189].

6.2 Materials and methods

6.2.1 Materials

T_1-weighted images of 92 subjects aged between 60 and 96 years old were obtained from the publicly available OASIS database [189]. This dataset consisted of 39 non-demented subjects, 39 demented subjects, and 14 MCI converters who were characterized as non-demented at the time of the image acquisition but became demented at later stages of the study. The non-demented and demented subjects were randomly grouped into separate training and testing sets as follows. The training set included a group of 25 demented subjects and a group of 25 non-demented subjects, each of which comprised 7 males and 18 females. The testing set included the remaining 14 non-demented subjects, 14 demented subjects and the group of 14 MCI converters. Each group of the testing set

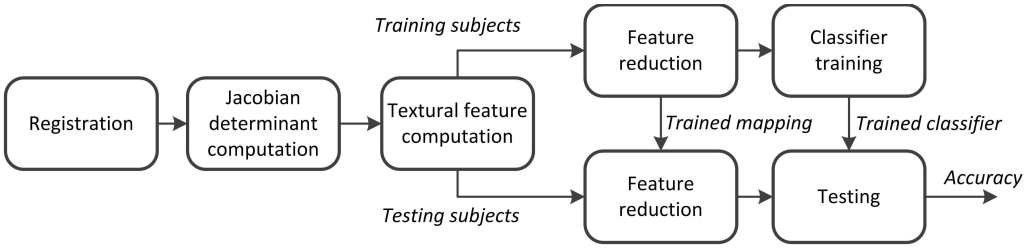


FIGURE 6.1: Flowchart of the proposed approach.

comprised 4 males and 10 females. All groups in the training set and testing set were age-matched.

6.2.2 Methods

T_1-weighted images of all subjects were non-rigidly registered to a template. Subsequently, the Jacobian determinant map of the deformation field resulting from the non-rigid registration was computed. A large number of textural features were derived from the Jacobian determinant map. A classifier was trained using the features retained after feature reduction. The performance of the trained classifier was evaluated on the testing set. The overall framework is depicted in Figure 6.1.

6.2.2.1 Registration

Each subject was registered to a common template in a two-step framework using the *elastix* registration toolbox [85]. As this work involved local textural characteristics of the deformation field, instead of using an average image of the studied population as the template, we chose to use a high contrast, high resolution template (Colin27) constructed from 27 scans of the same normal individual [190]. In the first step of the registration, we applied an affine transformation to compensate for the global misalignment with normalized correlation coefficient as a similarity measure. In the second step, a B-Spline non-rigid registration was used to compensate for local misalignment. The B-Spline registration was carried out at five resolutions using an isotropic grid spacing of 120, 60, 60, 30 and 15 mm. We used mutual information as a similarity measure and an adaptive gradient descent search algorithm. The brain mask of the Colin27 template was used as a mask of region of interest during the affine and B-Spline registrations.

6.2.2.2 Jacobian determinant computation

For each B-Spline registration, the determinant of Jacobian was computed as following: $\boldsymbol{J(p)} = det(\partial_{\boldsymbol{T}}/\partial_{\boldsymbol{p}})$, where $\boldsymbol{T(p)}$ was the recovered non-rigid transformation, and $\boldsymbol{p}$ a voxel coordinate. Values of $\boldsymbol{J}$ greater than 1 indicate volumetric expansion, smaller than 1 indicate compression, and equal to 1 indicate preservation. An example of the Jacobian determinant map is provided in Figure 6.2.

6.2.2.3 Textural feature computation

In this study, the textural features were computed based on the Grey-Level Co-occurrence Matrix (GLCM). The 3D GLCM $\boldsymbol{M}$ was computed from the Jacobian determinant map

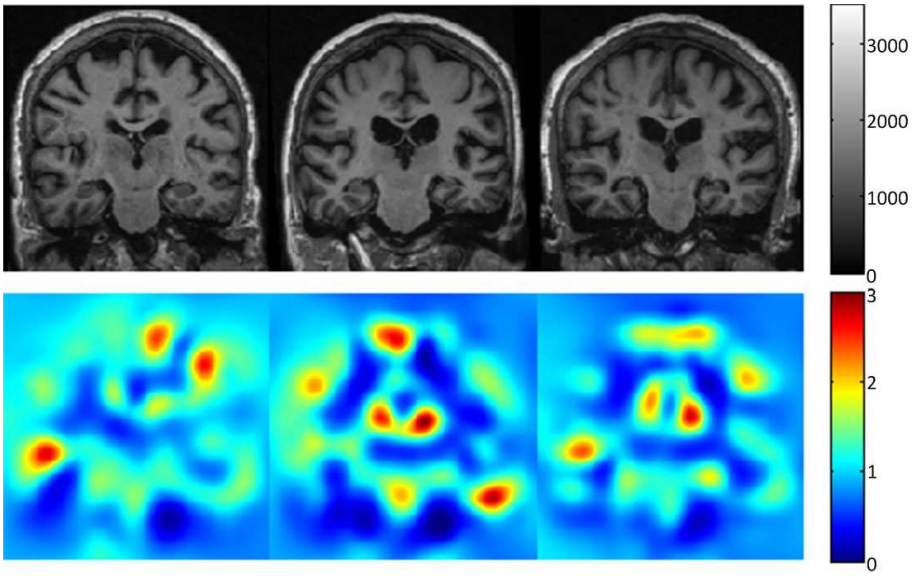


FIGURE 6.2: The Jacobian determinant maps of three 78 years old female subjects: non-demented (left), MCI (middle), and demented (right). Upper row: T_1-weighted images which were registered to the Colin27 template using affine transformation; lower row: the corresponding Jacobian determinant maps computed from the B-Spline transformations.

over the entire brain region of each subject as proposed in Chen et al. [42]:

$$\boldsymbol{M}(i,j) = \sum_{x=1}^{P}\sum_{y=1}^{Q}\sum_{z=1}^{L}\begin{cases}1 \text{ if } \boldsymbol{I}(x,y,z) = i \text{ and } \boldsymbol{I}(x+\Delta_x, y+\Delta_y, z+\Delta_z) = j \\ 0, \text{ otherwise}\end{cases}, \tag{6.1}$$

where $\boldsymbol{M}(i,j)$ was the entry at row i^{th} and column j^{th} of matrix $\boldsymbol{M}$, $\boldsymbol{I}$ the Jacobian determinant map, $\Delta(\Delta_x, \Delta_y, \Delta_z)$ an offset composed of a direction θ and a distance d.

Prior to the computation of GLCMs, the Jacobian determinant map was quantized to N quantization levels to avoid obtaining sparse matrices. The global minimum and global maximum of the Jacobian determinant of all training and testing subjects were used in the quantization step. In this study, we chose the commonly used quantization level N of 64 [35]. 169 GLCMs were computed considering 13 directions and 11 distances (d = 1, 5, 10, 15,..., 50 voxels). A wide range of d was chosen so that the derived features could be sensitive to textural variations at different scales. Thirteen Haralick features [41] were derived from each GLCM, resulting in a feature vector of 1859 elements.

6.2.2.4 Classification

6.2.2.4.1 Feature reduction

Principal Component Analysis (PCA) was applied on the resulting data to reduce the number of features such that 95% of the data variance was retained. Since the range of the features was very different, to avoid the PCA emphasizing features with large ranges, we normalized the features to unit-variance before applying PCA.

6.2.2.4.2 Training and testing

In this study, we used a bootstrapping approach where the training set and testing set were formed by randomly splitting the dataset of 92 subjects. Group division was repeated 1000 times on the non-demented and demented subjects whereas the MCI converters were used as testing subjects in every iteration. For each iteration, a 5-fold cross-validation was performed on the training set using a k-nearest neighbour (k-NN) classifier and a linear support vector machine (SVM) with polynomial kernel of order 1. The cross-validation was repeated 30 times and the average performance was reported. Subsequently, the classifiers, trained using all samples of the training set, were used to classify subjects in the testing set. To assess the classification performance, we computed the sensitivity, specificity, accuracy, and area under ROC curve (AUC). The feature reduction and classification experiments were carried out using the Matlab pattern recognition toolbox PRTools (http://www.prtools.org/).

6.2.2.4.3 Comparison with classification based on inter-subject whole brain dissimilarities

For comparison purposes, we implemented two different classification approaches. The first approach involved inter-subject whole brain dissimilarities as presented in Klein et al. [67]. Pairwise registration was carried out to register each subject to all other subjects using an affine registration followed by a B-Spline registration. The same parameter settings of *elastix* as described in section 6.2.2.1 were used in this registration. A dissimilarity matrix was computed from the standard deviation of the logarithm ($stdev(log)$) of the Jacobian determinant maps and used as input feature matrix of a classifier. Each feature vector consisted of 50 elements. For each subject i, each feature was derived as the dissimilarity measure between that subject and a subject j ($j \in [1;50]$) in the training set. A k-NN classifier, as proposed in Klein et al. [67], and a linear SVM with order 1 polynomial kernel were used for classification. The second approach used $stdev(log)$ of $\boldsymbol{J}_{iT}$, where $\boldsymbol{J}_{iT}$ was the Jacobian determinant map of the transformation from subject i to the Colin27 template, as a feature to train a k-NN classifier and a linear SVM with order 1 polynomial kernel. This approach hereafter is referred to as the hybrid approach since it is based on registration to a single template, as employed in our approach, to compute dissimilarities similar to those proposed in Klein's approach.

Similarly to our approach, Klein's approach and the hybrid approach were evaluated using the bootstrapping procedure. In each case of group division, 5-fold cross-validation was performed on the training set and the trained classifiers were used for classification of subjects in the testing set. Paired t-tests, with significant level of 0.05, were performed to compare our approach with Klein's approach and the hybrid approach in terms of sensitivity, specificity, accuracy, and AUC. The following aspects were addressed in the comparison: classification performance of our approach *versus* Klein's approach and the hybrid approach, pairwise registration *versus* registration to a single template, the use of a global dissimilarity feature *versus* global and local textural features, and performance of a k-NN classifier *versus* a linear SVM.

6.3 Results and discussion

Table 6.1 presents a summary of the cross-validation performance on the training set and the classification results of the trained classifiers on the testing set. The detailed results are visualized by the boxplots in Figure 6.3.

TABLE 6.1: Classification performance on the training set and testing set. In the testing set, the converters and demented subjects were labelled in the same class. Spec = specificity, Sen = sensitivity, Acc = Accuracy. * in the results of Klein's approach and the hybrid approach indicates a significant difference between one of these approaches and our approach. † in the results of Klein's approach indicates a significant difference between this approach and the hybrid approach.

Classification approach	Classifier	Training set (cross-validation)			Testing set						
					Performance over entire testing set				Accuracy per group (%)		
		Spec (%)	Sen (%)	Acc (%)	Spec (%)	Sen (%)	Acc (%)	AUC	Non-demented	Demented	Converters
Klein's approach	*k*-NN	57 ± 7*†	46 ± 8*†	52 ± 5*†	55 ± 16*	50 ± 14*†	51 ± 7*†	0.53 ± 0.08*†	55 ± 16*	47 ± 17*†	53 ± 14*†
	SVM	47 ± 18*†	53 ± 18*†	50 ± 5*	45 ± 25*†	54 ± 26*†	51 ± 10*†	0.52 ± 0.08*	45 ± 25*†	52 ± 25*†	55 ± 27*†
Hybrid approach	*k*-NN	55 ± 7*	51 ± 7*	53 ± 6*	54 ± 16*	54 ± 13	54 ± 7*	0.56 ± 0.07*	54 ± 16*	50 ± 16*	57 ± 15*
	SVM	45 ± 12*	56 ± 8*	50 ± 9*	47 ± 17*	62 ± 12*	57 ± 13*	0.52 ± 0.12*	47 ± 17*	56 ± 12*	68 ± 18*
Our approach	*k*-NN	63 ± 7	48 ± 8	55 ± 5	63 ± 16	54 ± 13	57 ± 8	0.62 ± 0.09	63 ± 16	49 ± 16	60 ± 18
	SVM	60 ± 6	59 ± 6	59 ± 5	62 ± 14	67 ± 12	65 ± 8	0.72 ± 0.08	62 ± 14	58 ± 15	76 ± 13

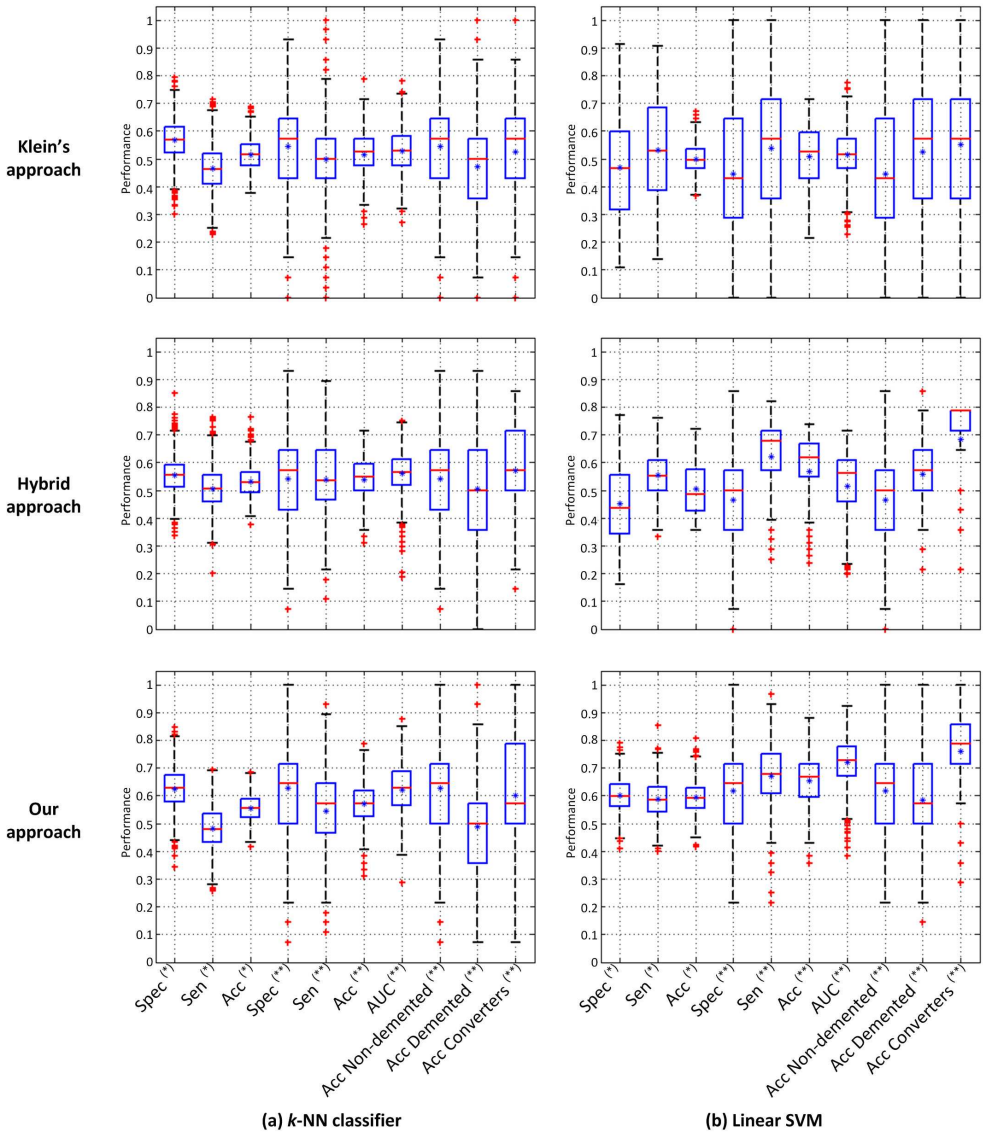


FIGURE 6.3: Cross-validation performance on the training set (*) and classification results on the testing set (**) of three approaches using (a) *k*-NN classifier and (b) linear SVM. Spec = Specificity, Sen = Sensitivity, Acc = Accuracy. In each boxplot, the red line presents the median value while the blue star presents the mean.

6.3.1 Performance of the proposed approach

Our approach with the linear SVM yielded an accuracy of 59 ± 5% (Spec = 60 ± 6%, Sen = 59 ± 6%) on the training set, an accuracy of 65 ± 8% (Spec = 62 ± 14%, Sen = 67 ± 12%) and AUC of 0.72 ± 0.08 on the testing set. Compared to the linear SVM, a lower performance was obtained using the *k*-NN classifier (Acc = 55 ± 5% on the training set; and Acc = 57 ± 8%, AUC = 0.62 ± 0.09 on the testing set). The classification performances of our approach were moderate, indicating that the textural features indeed contained useful discriminative information. Interestingly, it is noted that our approach showed a good accuracy for the prediction of MCI converters (Acc = 76 ± 13%), which was higher than the classification accuracy of AD in the testing set (Acc = 58 ± 15%). This indicates that our approach could capture patterns of volumetric changes that are more prominent in the converters than in AD.

6.3.2 Our approach *versus* Klein's approach and the hybrid approach

The numerical results presented in Table 6.1 show that our approach yielded higher classification results compared to both Klein's approach and the hybrid approach using either a *k*-NN classifier (Acc = 55 ± 5% for our approach *vs.* 52 ± 5% for Klein's approach and 53 ± 6% for the hybrid approach on the training set; Acc = 57 ± 8% *vs.* 51 ± 7% and 54 ± 7%, AUC = 0.62 ± 0.09 *vs.* 0.53 ± 0.08 and 0.56 ± 0.07 on the testing set) or a linear SVM (Acc = 59 ± 5% *vs.* 50 ± 5% and 50 ± 9% on the training set; Acc = 65 ± 8% *vs.* 51 ± 10% and 57 ± 13%, AUC = 0.72 ± 0.08 *vs.* 0.52 ± 0.08 and 0.52 ± 0.12 on the testing set). Using the linear SVM, our approach gave the best performance both on the training and testing sets. A rather large deviation of the classification accuracy on the testing set was observed from the boxplots in Figure 6.3 for all three approaches. Nevertheless, our approach with the linear SVM showed the lowest deviation compared to the other approaches with the same classifier (standard deviation = 8%, 10%, and 13% for our approach, Klein's approach, and the hybrid approach, respectively). Overall, the results showed that our approach significantly outperformed Klein's approach and the hybrid approach and seem to indicate that the relatively low performances, compared to existing literature, may be attributed to the selected data.

6.3.3 Pairwise registration *versus* registration to a single template

While the hybrid approach was only based on registration of subjects to a common template, Klein's approach required a large number of registrations, which was not only computationally intensive but also more prone to registration errors. Both Klein's approach and the hybrid approach showed poor performance (maximum Acc = 57 ± 13% obtained by the hybrid approach on the testing set), with the hybrid approach showing higher classification accuracy both on the training and testing sets. It can be deduced that, in the context of this study, extensive pairwise registration did not bring added value compared to registration to a single template.

6.3.4 Global dissimilarity feature *versus* global and local textural features

The hybrid approach and our approach were based on the same registration. The feature used in the hybrid approach was computed as a global measure from the resulting Jacobian determinant map. Our approach, on the other hand, involves second-order textural features computed at different scales. This enables the approach to be more sensitive to spatial differences. It can be observed in Table 6.1 that a higher sensitivity

was obtained using our approach with the linear SVM compared to the hybrid approach on the training set (Sen = 59 ± 6 % *vs.* 56 ± 8 %) and the testing set (Sen = 67 ± 12 % *vs.* 62 ± 12 %).

6.3.5 *k*-NN classifier *versus* linear SVM

In our approach, the linear SVM gave superior performance, especially the sensitivity, compared to the *k*-NN classifier. In the hybrid approach, the *k*-NN classifier showed higher accuracy on the training set and higher AUC on the testing set. This classifier showed a higher accuracy on the training set, a comparable accuracy and higher AUC on the testing set compared to the linear SVM in Klein's approach. These observations suggest that the performance of the classifiers is strongly dependent on the particular framework. In this case, the linear SVM is preferred for our approach whereas the *k*-NN classifier is more suitable for Klein's approach and the hybrid approach.

6.4 Conclusions

In this paper, we presented a new approach to image registration-based classification for brain pathologies. The results show that this approach significantly outperformed two similar approaches, one published elsewhere in the literature. Additionally, in the context of this study, pairwise registration did not bring added value compared to registration to a single template and textural features were more informative than dissimilarity-based features. This study demonstrates the potential of texture analysis on the Jacobian determinant map over the entire brain for diagnosis of AD subjects.

7

Summary and conclusion

7.1 Summary and conclusion

Alzheimer's (AD) and Huntington's (HD) diseases are among the most devastating and costly neurodegenerative diseases. Finding biomarkers for early detection of AD and for disease monitoring as well as therapeutic agent assessment of HD has been a long-standing research goal for neuro-scientists. Post-mortem studies have demonstrated the association between AD and HD with abnormal iron accumulation in the brain structures such as the basal ganglia and the cerebral cortex. T_2^*-weighted imaging provides a non-invasive means to study susceptibility changes of substances such as myelin and iron in the brain. Particularly, phase images show an increased sensitivity to magnetic susceptibility differences with increased field strength. The main goal of the thesis was to develop methods for quantitative analysis of human brain T_2^*-weighted images at ultrahigh field strength. Additionally, we also aimed to investigate textural features for classification of AD in a deformation-based context.

Chapter 1 of the thesis provided an overview of AD and HD as well as T_2^*-weighted imaging at ultrahigh field strength. We highlighted the increased interest in using ultrahigh field T_2^*-weighted images for susceptibility studies of the diseases and the need to develop quantitative analysis techniques making use of these images. A brief review of texture analysis and its application in neuro-MR image analysis were presented. Finally, this chapter summarized the goals and contributions of the thesis.

In **chapter 2**, we proposed a quantitative analysis framework composed of 7T T_2^*-weighted imaging and a second order texture analysis approach. Textural features were computed from both the magnitude and phase images and subsequently used for group-wise comparison. We applied the proposed approach to study textural differences in subcortical structures between pre-manifest HD, manifest HD and control subjects. While the magnitude-based features showed differences in the pallidum in manifest HD, the phase-based features showed differences in the caudate nucleus and in both the caudate nucleus and putamen in premanifest HD and manifest HD, respectively. Our study reported the first evidence of textural heterogeneity of subcortical structures in HD. The regional specific textural differences found are in line with existing findings on structural deficits in both premanifest and manifest HD.

While chapter 2 focused on subcortical structures, chapters 3, 4 and 5 dealt with

the cerebral cortex. In **chapter 3**, we presented a new method for segmentation of the cerebral cortex from 7T T_2^*-weighted images. We first discussed the need to develop a new method that allows to perform the segmentation directly on T_2^*-weighted images. Manual segmentation is not feasible as it is not only time consuming but also subjected to inter-subject variability. Segmentation based on T_1-weighted images suffers from the decreased GM/WM contrast due to aging effect. The proposed method was based on *K*-means clustering of the magnitude and phase images. It combined magnitude and phase information in a two-step framework. In the first step, the outer contour of the cortex was segmented using the magnitude information. Subsequently, an initial inner contour was estimated using the combined magnitude and phase information, thereby obtaining the initial segmentation of the cortex. In the second step, this initial segmentation was further refined using a mathematical tool called transformation with reconstruction criteria to obtain the final segmentation. We evaluated our method using the manual segmentations and the T_1-based segmentations obtained using FreeSurfer and FSL, two state-of-the-art methods. Our method showed good agreement with the manual segmentation and a superior performance compared to the T_1-based approaches.

Chapter 4 presented a method for local group-wise analysis of the cerebral cortex. The cortex was segmented using the method presented in chapter 3 and parcellated using an atlas with predefined cortical areas. Subsequently, local GM/WM contrast and local cortical profile were computed automatically at each parcellated cortical ROI. Group-wise comparison in terms of local GM/WM contrast was performed using a Mann-Whitney U-test. To compare local cortical profiles, we used two permutation tests, one using the entire profile and one performed at each node on the profile. We applied the method to compare a group of young subjects and a group of elderly healthy subjects. Using local phase and magnitude GM/WM contrast, differences were shown in 14 and 15 of 17 studied regions, respectively. Localized differences in phase and magnitude profiles were revealed in 16 and 17 regions, respectively. The local comparison at each cortical depth highlighted differences in the centre and boundaries of the cortex. The differences found were in line with existing literature and could be explained by known changes in myelin and iron content as an effect of aging. The results showed that the method can be a useful tool in studying normal aging and might also be useful in studies of neurodegenerative diseases.

In **chapter 5**, we explored regional differences between early onset AD (EOAD) patients and late onset AD (LOAD) patients using MR phase images. We manually measured peak phase shift from four different lobes in the brain and applied the method presented in chapter 4 to compute GM/WM phase contrast and cortical phase profile at several local cortical regions. Subsequently, we applied a linear regression model adjusted for gender and the disease severity, quantified by MMSE score, to assess group differences in terms of lobar phase shift and local GM/WM contrast. The differences in cortical profiles were evaluated using two permutation tests as described in chapter 4. The results showed that subjects with EOAD had a larger cortical phase contrast and a more severely affected cortical layer pattern compared to LOAD subjects, especially in the middle frontal gyrus, postcentral gyrus, superior parietal gyrus, and precuneus. These results indicate that patients with EOAD have an increased iron accumulation possibly related to an increased amyloid deposition in specific cortical regions compared to LOAD patients.

Finally, in **chapter 6**, we investigated the use of deformation-based textural features in

classification of AD and compared the added value of registration to a single template and pairwise registration in such a classification framework. In our approach, T_1-weighted images of 92 subjects were non-rigidly registered to a template. Textural features were derived from the Jacobian determinant map of the resulting deformation field of the entire brain using the Gray Level Co-occurrence Matrix (GLCM) approach. PCA was applied on the large set of computed features for feature reduction. The retained features were used as an input of a linear support vector machine for classification. Classification performance was evaluated using a bootstrapping procedure. We compared the method with two dissimilarity-based approaches, one based on pairwise registration and the other based on registration to a template. We showed in the context of this study that pairwise registration did not bring added value compared to registration to a single template and textural features were more informative than dissimilarity-based features. Our study demonstrates the potential of texture analysis on the Jacobian determinant map over the entire brain for diagnosis of AD subjects.

Considering the work presented in **chapters 2-6**, we believe that we have achieved the goals formulated in Section 1.5. We set up a framework for texture analysis of subcortical structures using 7T T_2^*-weighted images (**chapter 2**). Application of the framework was demonstrated in HD. In terms of cortical analysis, a new algorithm for segmentation of the cortex from 7T T_2^*-weighted images was proposed and extensively validated (**chapter 3**). This development enabled further steps in quantification of changes in the cortex. Subsequently, we developed a highly automated method for detecting regional changes in GM/WM contrast and cortical profile at multiple cortical ROIs (**chapter 4**). In addition to an analysis of aging effect using data of young and old healthy subjects (**chapter 4**), this method was also applied an in vivo study of AD patients (**chapter 5**). Besides, the use of textural features derived from the deformation field was addressed (**chapter 6**). Even though the classification performance was moderate, the results demonstrated the potential of using deformation-based textural features in classification of AD.

7.2 Future work

Phase unwrapping is an important preprocessing step in phase-based analysis. Throughout this thesis, we used a high-pass filtering technique [25] to perform this operation. Even though this technique has been widely used in the literature, one disadvantage is that, depending on the kernel size used, it could lead to information loss or artifacts remaining in areas with very steep transitions [191]. Non-filtering techniques such as SHARP [192] and PRELUDE [193] could be considered as alternatives.

Image phase has some limitations. It is affected by the structure geometry and tissue orientation with respect to the main magnetic field. Furthermore, it has been shown that the phase image has a non-local relation with the underlying tissue susceptibility. Much research is focusing on developing quantitative susceptibility mapping techniques [143, 144] that can provide an estimation of tissue susceptibility map based on phase images. The texture analysis and group-wise cortical analysis frameworks could be easily adapted to derive cortical features from a susceptibility map. It should be mentioned that the cortex segmentation step would still require the combined magnitude and phase information.

In chapter 4, we investigated two cortical features, local cortical GM/WM contrast and cortical profile, on magnitude and phase images. Other cortical characteristics, for instance, local inhomogeneity can be visually observed on the phase images. Further

work should focus on deriving cortical textural features. For that purpose, the GLCM approach deployed in chapter 2 for subcortical structures could be extended to analysis of the cortex. While computing GLCM, the search direction should be adapted at each voxel being considered using the norm of the outer cortical surface at that voxel as the reference direction.

The performance of AD classification presented in chapter 6 was moderate. Textural features were derived solely from the entire brain deformation field, which was strongly dependent on the registration settings. In this study, we used B-Spline registration in a multi-resolution non-rigid registration framework. At the finest resolution, a relatively large grid spacing of 15mm was emperically chosen to avoid physiology-meaningless "foldings" in the deformation field. A disadvantage is that the deformation may not be sensitive to small local changes such as changes in the accumbens nucleus [194] or in thickness of the cerebral cortex [195]. Further research could examine the use of smaller grid spacings in combination with a bending penalty term. Additionally, multi-resolution texture analysis techniques such as Wavelet-based approaches [39] could be investigated.

In this thesis, application of the methods developed for 7T T_2^*-weighted image analysis has been demonstrated in normal aging, Alzheimer's disease and Huntington's disease. Nevertheless, they can also be applied in the context of other neurological diseases such as Parkinson's disease and multiple sclerosis where clinical studies have reported alterations in iron content of the brain structures [77, 196].

Due to the much higher cost of a 7T human MRI system compared to a 3T system (7M $ vs. 3M $) and further technical development needed for 7T, it is not likely that 7T MRI will replace 3T MRI in the near future. Therefore, it would be interesting to check if the developed methods can be translated to 3T. However, it should be noted that susceptibility-based studies performed at 7T would benefit from an increased sensitivity with respect to tissue magnetic susceptibility compared to 3T.

Iron has been shown to play an important role in normal aging and neurological disease processes. In my opinion, T_2^*-weighted imaging at ultrahigh field holds great promise to be a useful tool for in vivo studies of brain iron. Constant effort has been dedicated to designing sequences and hardware to improve the quality of images acquired at ultrahigh field. Images with higher resolution and sensitivity to tissue susceptibility are possible to obtain. Image processing techniques such as those presented in this thesis would be good candidates for extracting useful information from ultrahigh field T_2^*-weighted magnitude and phase images.

Samenvatting en conclusie

Samenvatting en conclusie

De ziekte van Alzheimer (AD) en de ziekte van Huntington (HD) behoren tot de ernstigste en meest ingrijpende neurodegeneratieve ziekten. Het vinden van biomarkers voor vroege opsporing van AD, het volgen van het ziekteproces en de ontwikkeling van nieuwe behandelingen voor HD zijn belangrijke onderzoeksdoelen. Post-mortem studies hebben de associatie aangetoond tussen AD en HD met verhoogde ijzerstapeling in de hersenstructuren, zoals de basale ganglia en de cerebrale cortex. T_2^*-gewogen MRI beeldvorming biedt de mogelijk om op een niet-invasieve wijze veranderingen in magnetische susceptibiliteit van stoffen zoals myeline en met name ijzer in de hersenen te bestuderen. Fasebeelden in het bijzonder, tonen bij hoge veldsterktes een verhoogde sensitiviteit voor verschillen in magnetische susceptibiliteit. Het doel van dit proefschrift was om methoden te ontwikkelen voor de kwantitatieve analyse van T_2^*-gewogen beelden van het menselijk brein gemaakt met ultrahoge veldsterkte. Daarnaast hebben we ons ook gericht op het onderzoeken van textuurkenmerken voor de classificatie van AD in een deformatie-gebaseerde context.

Hoofdstuk 1 van dit proefschrift beschrijft de achtergrond van de ziektes AD en HD, en geeft een inleiding in T_2^*-gewogen MRI beeldvorming bij ultrahoge veldsterkte. Gezien de groeiende interesse in het gebruik van T_2^*-gewogen beelden met ultrahoge veldsterkte, wordt de noodzaak om kwantitatieve analysetechnieken te ontwikkelen voor deze beelden steeds groter. Vervolgens wordt een kort overzicht gepresenteerd van textuuranalyse en haar toepassingen in de neuro-MR beeldanalyse. Tot slot geeft dit hoofdstuk een overzicht van de doelstellingen en de bijdragen van dit proefschrift.

In **hoofdstuk 2** hebben we een platform voor kwantitatieve analyse geïntroduceerd bestaande uit 7T T_2^*-gewogen beeldvorming en een tweede orde textuuranalyse benadering. Textuurkenmerken werden berekend uit zowel de magnitude en fase beelden en vervolgens gebruikt voor groepsgewijze vergelijkingen. De voorgestelde aanpak is toegepast om textuur verschillen te bestuderen in de subcorticale structuren tussen premanifeste HD patiënten, manifeste HD patiënten en controlestudies. De kernmerken gebaseerd op de magnitude beelden toonen met name verschillen in het pallidum in manifeste HD patiënten. Daarentegen, de kenmerken op de fase beelden lieten verschillen zien in de nucleus caudatus in pre-manifeste HD patiënten en verschillen in zowel de nucleus caudatus als het putamen in manifeste HD patiënten. Onze studie beschrijft een eerste bewijs van heterogeniteit in de textuur van subcorticale structuren in HD. De gevonden regio-specifieke textuurverschillen komen overeen met de bestaande bevindingen over structurele afwijkingen in zowel premanifeste en manifeste patiënten met HD.

Waar de focus in hoofdstuk 2 lag op de subcorticale structuren, ligt de focus in de hoofdstukken 3, 4 en 5 op de cerebrale cortex. In **hoofdstuk 3** wordt een nieuwe methode voor de segmentatie van de cerebrale cortex op 7T T_2^*-gewogen beelden gepresenteerd. Als

eerste werd de noodzaak besproken om een nieuwe segmentatie methode te ontwikkelen gebaseerd op de T_2^*-gewogen beelden. In deze beelden is manuele segmentatie niet haalbaar, niet alleen omdat het tijdrovend is, maar ook gevoelig voor inter-subject variabiliteit. Segmentatie op basis van het T_1-gewogen beeld wordt verder bemoeilijkt door een verminderd GM/WM contrast als gevolg van veroudering. De voorgestelde methode is gebaseerd op *K*-means clustering van de magnitude en fase beelden en combineert informatie uit de magnitude en fase beelden in een twee-traps benadering. In de eerste stap wordt de buitenste contour van de cortex gesegmenteerd aan de hand van de magnitude informatie. Vervolgens wordt een initiëlebinnen contour geschat aan de hand van de gecombineerde magnitude en fase informatie, resulterend in een initiële segmentatie van de cortex. In de tweede stap wordt de initiële segmentatie verder verfijnd met behulp van transformatie met specifieke reconstructiecriteria, om de uiteindelijke segmentatie verkrijgen. De methode werd geëvalueerd met behulp van de manuele segmentaties en de T_1-gebaseerde segmentaties verkregen met behulp van FreeSurfer en FSL, twee state-of-the-art methoden. Onze methode toont een goede overeenkomst met de manuele segmentatie en superieure prestaties in vergelijking met de T_1- gebaseerde benaderingen.

In **hoofdstuk 4** wordt een methode geïntroduceerd voor lokale groepsgewijze analyse van de cerebrale cortex. De cortex wordt gesegmenteerd volgens de methode beschreven in hoofdstuk 3 en vervolgens opgedeeld met behulp van een atlas waarin gedefinieerde corticale gebieden staan. Vervolgens werd automatisch voor elke corticale gebied het lokale GM/WM contrast en het lokale corticale profiel berekend. Groepsgewijze vergelijkingen aan de hand van lokaal GM/WM contrast werd uitgevoerd met behulp van een Mann-Whitney U-test. Twee permutatietests zijn gebruikt om lokale corticale profielen te vergelijken; één test met het hele profiel en één test op elk knooppunt in het profiel. We pasten de methode toe voor het vergelijken van een groep jonge proefpersonen met een groep oudere gezonde proefpersonen. Door het gebruik van de lokale fase- en magnitudecontrast van GM/WM werden verschillen gevonden in respectievelijk 14 en 15 van 17 de onderzochte gebieden. Gelokaliseerde verschillen in de fase- en magnitude profielen werden gevonden in respectievelijk 16 en 17 regio's. De lokale vergelijking op elke corticale diepte van het profiel toonde verschillen tussen het centrum en de grenzen van de cortex. De gevonden verschillen komen overeen met de bestaande literatuur en kunnen worden verklaard door de reeds bekende veranderingen in myeline en ijzergehalte als gevolg van veroudering. De resultaten tonen aan dat de methode een nuttig instrument kan zijn bij het bestuderen van het normale verouderingsproces en ook toegevoegde waarde kan hebben bij het bestuderen van neurodegeneratieve ziekten.

In **hoofdstuk 5** hebben we de regionale verschillen onderzocht tussen patiënten die op jonge leeftijd AD ontwikkelen (EOAD, Early Onset AD) en patiënten die op latere leeftijd AD ontwikkelen (LOAD, Late Onset AD) aan de hand van MR fasebeelden. We hebben handmatig de piek faseverschuiving in alle hersenkwabben gemeten en hebben de methode uit hoofdstuk 4 voor het berekenen van GM/WM fasecontrast en corticaal fase profiel in verschillende lokale corticale gebieden toegepast. Vervolgens hebben we een lineair regressie model gecorrigeerd voor geslacht en de MMSE score gebruikt om groepsverschillen in termen van lobaire faseverschillen en lokaal GM/WM contrast te beoordelen. De verschillen in corticale profielen werden geëvalueerd met behulp van twee permutatietests zoals beschreven in hoofdstuk 4. De resultaten toonen aan dat patiënten met EOAD een hoger corticaal fasecontrast en een meer aangedaan corticaal

laagpatroon hadden in vergelijking met LOAD patiënten, vooral in de middelste frontale gyrus, postcentralis gyrus, superieure pariëtale gyrus, en precuneus. Deze resultaten tonen aan dat EOAD patiënten meer ijzerstapeling hebben, mogelijk gerelateerd aan een verhoogde amyloïd stapeling, in vergelijking met LOAD patiënten.

Tenslotte wordt in **hoofdstuk 6**, het gebruik van deformatie-gebaseerde textuurkenmerken voor de classificatie van AD beschreven, en wordt de toegevoegde waarde van de registratie naar een template en paarsgewijze registratie met behulp van een classifier vergeleken. In onze aanpak werden T_1-gewogen beelden van 92 proefpersonen niet-rigide geregistreerd op een template. Textuurkenmerken werden afgeleid van de Jacobiaan determinanten matrix van het resulterende deformatieveld van het gehele brein met behulp van Gray Level Co-occurrence Matrix (GLCM). Principale componenten analyse werd toegepast op de grote set van berekende functies om het aantal kenmerken te reduceren. De behouden kenmerken werden gebruikt als input van een lineaire support vector machine die werd gebruikt voor classificatie. De classificatie werd geëvalueerd met behulp van een bootstrapping procedure. We vergeleken de methode met twee op verschil-gebaseerde benaderingen, één gebaseerd op paarsgewijze registratie en de andere op basis van de registratie naar een sjabloon. We toonen in het kader van dit onderzoek aan dat paarsgewijze registratie geen meerwaarde heeft ten opzichte van de registratie naar een enkel sjabloon en dat textuurkenmerken informatiever zijn dan verschil-gebaseerde kernmerken. Onze studie toont het potentieel van textuuranalyse op de Jacobian determinant matrix aan over het hele brein voor de diagnose van AD patiënten.

Terugblikkend op het werk beschreven in de hoofdstukken 2 tot en met 6, denken we de doelstellingen geformuleerd in paragraaf 1.5 te hebben bereikt. We hebben een platform ontwikkeld voor textuuranalyse van subcorticale structuren aan de hand van 7T T_2^*-gewogen beelden (**hoofdstuk 2**). De toepassing van het framework werd aangetoond in HD. Voor corticale analyse is een nieuw algoritme voor segmentatie van de cortex op basis van 7T T_2^*-gewogen beelden voorgesteld en uitgebreid gevalideerd (**hoofdstuk 3**). Deze ontwikkeling maakt verdere stappen voor kwantificatie van veranderingen in de cortex mogelijk. Vervolgens hebben we een sterk geautomatiseerde methodiek ontwikkeld voor het identificeren van regionale veranderingen in GM/WM contrast en veranderingen in het corticale profiel in meerdere corticale gebieden (**hoofdstuk 4**). Naast een analyse van het verouderingseffect aan de hand van gegevens van jonge en oude gezonde proefpersonen (**hoofdstuk 4**), werd deze methode ook toegepast in een onderzoek met AD patiënten (**hoofdstuk 5**). Bovendien is het gebruik van textuurkenmerken afgeleid uit het deformatieveld besproken (**hoofdstuk 6**). Hoewel de classificatie matig presteerde, toonen de resultaten het potentieel van het gebruik deformatie-gebaseerde textuurkenmerken voor de classificatie van AD aan.

Vervolgonderzoek

Fase extractie is een belangrijke voorbereidingsstap in fase-gebaseerde analyse. In dit proefschrift, hebben we een high-pass filter techniek [25] gebruikt om deze bewerking uit te voeren. Hoewel deze techniek op grote schaal wordt gebruikt, heeft deze het nadeel dat, afhankelijk van de gebruikte kernelgrootte, het kan leiden tot verlies van informatie of juist tot het behoud van artefacten in gebieden met scherpe overgangen [191]. Technieken die niet gebaseerd zijn op filtering, zoals SHARP [192] en PRELUDE [193], kunnen als alternatieven dienen: dit verdient nader onderzoek

Fasebeelden hebben een aantal beperkingen. Het beeld wordt beïnvloed door de geometrie van de structuur en de oriëntatie van het weefsel ten opzichte van het magneetveld. Bovendien is aangetoond dat de fase een niet-lokale relatie heeft met de susceptibiliteit van het onderliggende weefsel. Een groot deel van het onderzoek is gericht op het ontwikkelen van kwantitatieve susceptibiliteit kenmerken [143, 144] die de susceptibiliteit van weefsel kunnen schatten op basis van op fasebeelden. De textuuranalyse en groepsgewijze corticale analyse methoden kunnen eenvoudig worden aangepast om corticale kenmerken af te leiden uit een susceptibiliteitsgrafiek. De segmentatie van de cortex vereist echter nog wel de aanwezigheid van gecombineerde magnitude en fase informatie.

In hoofdstuk 4 onderzochten we twee corticale kenmerken, namelijk lokaal corticaal GM/WM contrast en het corticale profiel, gebaseerd op magnitude en fase beelden. Andere corticale karakteristieken, zoals lokale inhomogeniteit, kunnen visueel worden waargenomen op de fasebeelden. Verder onderzoek moet worden toegespitst op het afleiden van corticale textuurkenmerken. Daartoe kan de GLCM methode die in hoofdstuk 2 wordt toegepast op subcorticale structuren worden uitgebreid naar de analyse van de cortex. Tijdens het berekenen van de GLCM moet de zoekrichting bij elke voxel worden aangepast zodat de norm van het buitenste corticale oppervlak van de desbetreffende voxel als referentie richting wordt gebruikt.

Het resultaat van de AD classificatie gepresenteerd in hoofdstuk 6 was matig. De textuurkenmerken werden afgeleid van het deformatieveld van het gehele brein en dit veld is sterk afhankelijk van de gekozen registratieinstellingen. In deze studie werd een B-Spline registratie gebruikt in een multi-resolutie registratie framework. Op de fijnste resolutie werd op empirische wijze een relatief grote roosterafstand van 15 mm gekozen om fysiek onmogelijke "vouwen" in het deformatieveld te voorkomen. Een nadeel hiervan is dat de vervorming wellicht niet gevoelig is voor veranderingen in kleine structuren zoalsin de nucleus accumbens [194] of de dikte van de cerebrale cortex [195]. In toekomstig onderzoek zou het gebruik van kleinere roosterafstanden in combinatie met een op buiging gebaseerde randvoorwaarde kunnen worden bestudeerd. Daarnaast kunnen multi-resolutie textuuranalysetechnieken zoals Wavelet-gebaseerde benaderingen [39] worden onderzocht.

In dit proefschrift is de toepassing van de ontwikkelde methoden voor 7T T_2^*-gewogen MRI beeldanalyse aangetoond bij normale veroudering, de ziekte van Alzheimer en de ziekte van Huntington. Tevens kunnen ze ook worden toegepast in de context van andere neurologische aandoeningen zoals de ziekte van Parkinson en multiple sclerose waarbij klinische studies veranderingen in ijzergehalte in de hersenstructuren hebben gerapporteerd [77, 196].

Door de veel hogere kosten van een 7T MRI systeem in vergelijking met een 3T systeem (7M $ tegenover 3M $) en verdere noodzakelijke technische ontwikkelingen voor 7T is het niet waarschijnlijk dat 3T MRI in de nabije toekomst door 7T MRI zal worden vervangen. Daarom zou het interessant zijn om te onderzoeken of de ontwikkelde methoden getransleerd kunnen worden naar 3T. Er moet wel worden opgemerkt dat susceptibiliteits-gebaseerde studies uitgevoerd op 7T gevoeliger zijn voor magnetische susceptibiliteitseffecten in het weefsel dan uitgevoerd op 3T.

In het verleden er is aangetoond dat ijzer een belangrijke rol speelt in het normale verouderingsproces en bij neurologische ziekteprocessen. T_2^*-gewogen beeldvorming bij ultrahoog veld is, naar mijn mening, een veelbelovend en nuttig hulpmiddel voor

in-vivo studies van het ijzergehalte in de hersenen. Er is veel onderzoek nodig voor het ontwerpen van sequenties en hardware om de kwaliteit van de beelden gemaakt met ultrahoge veldsterkte te verbeteren. Het moet mogelijk zijn beelden met een hogere resolutie en gevoeligheid voor weefsel susceptibiliteitseffecten te verkrijgen. Beeldverwerkingstechnieken zoals gepresenteerd in dit proefschrift zijn daarbij essentieel voor het extraheren van nuttige informatie uit ultrahoog veld T_2^*-gewogen magnitude en fase beelden.

References

[1] A. E. Guttmacher, F. S. Collins, R. L. Nussbaum, and C. E. Ellis, "Alzheimer's disease and parkinson's disease," *N Engl J Med*, vol. 348, no. 14, pp. 1356–1364, 2003.

[2] D. E. Barnes and K. Yaffe, "The projected effect of risk factor reduction on Alzheimer's disease prevalence," *The Lancet Neurology*, vol. 10, no. 9, pp. 819–828, 2011.

[3] A. Association, "2012 Alzheimer's disease facts and figures," *Alzheimers Dement*, vol. 8, no. 2, pp. 131–168, 2012.

[4] G. B. Frisoni, N. C. Fox, C. R. Jack, P. Scheltens, and P. M. Thompson, "The clinical use of structural MRI in Alzheimer disease," *Nat Rev Neurol*, vol. 6, no. 2, pp. 67–77, 2010.

[5] N. Fayed, P. J. Modrego, G. R. Salinas, and J. Gazulla, "Magnetic resonance imaging based clinical research in Alzheimer's disease," *J Alzheimers Dis*, vol. 31, pp. S5–S18, 2012.

[6] R. Roos, "Huntington's disease: a clinical review," *Orphanet J Rare Dis*, vol. 5, no. 1, p. 40, 2010.

[7] M. J. Novak and S. J. Tabrizi, "Huntington's disease: clinical presentation and treatment," *Int Rev Neurobiol*, vol. 98, pp. 297–323, 2011.

[8] C. A. Ross and S. J. Tabrizi, "Huntington's disease: from molecular pathogenesis to clinical treatment," *The Lancet Neurology*, vol. 10, no. 1, pp. 83–98, 2011.

[9] D. W. Weir, A. Sturrock, and B. R. Leavitt, "Development of biomarkers for Huntington's disease," *The Lancet Neurology*, vol. 10, no. 6, pp. 573–590, 2011.

[10] S. van den Bogaard, E. Dumas, J. van der Grond, M. van Buchem, and R. Roos, "MRI biomarkers in Huntington's disease," *Front Biosci (Elite Ed)*, vol. 4, pp. 1910–1925, 2012.

[11] T. G. Beach, S. E. Monsell, L. E. Phillips, and W. Kukull, "Accuracy of the clinical diagnosis of Alzheimer disease at National Institute on Aging Alzheimer Disease Centers, 2005-2010," *J Neuropathol Exp Neurol*, vol. 71, no. 4, pp. 266–273, 2012.

[12] L. Guzmán-Martínez, G. A. Farías, and R. B. Maccioni, "Emerging noninvasive biomarkers for early detection of Alzheimer's disease," *Arch Med Res*, vol. 43, no. 8, pp. 663–666, 2012.

[13] G. Bartzokis and T. A. Tishler, "MRI evaluation of basal ganglia ferritin iron and neurotoxicity in Alzheimer's and huntingon's disease," *Cell Mol Biol (Noisy-le-grand)*, vol. 46, no. 4, pp. 821–833, 2000.

[14] L. Zecca, M. B. H. Youdim, P. Riederer, J. R. Connor, and R. R. Crichton, "Iron, brain ageing and neurodegenerative disorders," *Nat Rev Neurosci*, vol. 5, no. 11, pp. 863–873, 2004.

[15] M. Fukunaga, T.-Q. Li, P. van Gelderen, J. A. de Zwart, K. Shmueli, B. Yao, J. Lee, D. Maric, M. A. Aronova, G. Zhang, R. D. Leapman, J. F. Schenck, H. Merkle, and J. H. Duyn, "Layer-specific variation of iron content in cerebral cortex as a source of MRI contrast," *Proc Natl Acad Sci U S A*, vol. 107, no. 8, pp. 3834–3839, 2010.

[16] I. Bohanna, N. Georgiou-Karistianis, A. J. Hannan, and G. F. Egan, "Magnetic resonance imaging as an approach towards identifying neuropathological biomarkers for Huntington's disease," *Brain Research Reviews*, vol. 58, no. 1, pp. 209–225, 2008.

[17] E. H. Aylward, "Change in MRI striatal volumes as a biomarker in preclinical Huntington's disease," *Brain Res Bull*, vol. 72, no. 2, pp. 152–158, 2007.

[18] S. J. Tabrizi, D. R. Langbehn, B. R. Leavitt, R. A. Roos, A. Durr, D. Craufurd, C. Kennard, S. L. Hicks, N. C. Fox, R. I. Scahill, B. Borowsky, A. J. Tobin, H. D. Rosas, H. Johnson, R. Reilmann, B. Landwehrmeyer, and J. C. Stout, "Biological and clinical manifestations of Huntington's disease in the longitudinal TRACK-HD study: cross-sectional analysis of baseline data," *The Lancet Neurology*, vol. 8, no. 9, pp. 791–801, 2009.

[19] J. S. Paulsen, P. C. Nopoulos, E. Aylward, C. A. Ross, H. Johnson, V. A. Magnotta, A. Juhl, R. K. Pierson, J. Mills, D. Langbehn, and M. Nance, "Striatal and white matter predictors of estimated diagnosis for Huntington disease," *Brain Res Bull*, vol. 82, no. 3-4, pp. 201–207, 2010.

[20] S. van den Bogaard, E. Dumas, T. Acharya, H. Johnson, D. Langbehn, R. Scahill, S. Tabrizi, M. van Buchem, J. van der Grond, and R. Roos, "Early atrophy of pallidum and accumbens nucleus in Huntington's disease," *J Neurol*, vol. 258, no. 3, pp. 412–420, 2011.

[21] S. van den Bogaard, E. Dumas, L. Ferrarini, J. Milles, M. van Buchem, J. van der Grond, and R. Roos, "Shape analysis of subcortical nuclei in Huntington's disease, global versus local atrophy - results from the TRACK-HD study," *J Neurol Sci*, vol. 307, no. 1-2, pp. 60–68, 2011.

[22] E. M. Dumas, M. J. Versluis, S. J. van den Bogaard, M. J. van Osch, E. P. Hart, W. M. van Roon-Mom, M. A. van Buchem, A. G. Webb, J. van der Grond, and R. A. Roos, "Elevated brain iron is independent from atrophy in Huntington's disease," *Neuroimage*, vol. 61, no. 3, pp. 558–564, 2012.

[23] G. B. Chavhan, P. S. Babyn, B. Thomas, M. M. Shroff, and E. M. Haacke, "Principles, techniques, and applications of T2*-based MR imaging and its special applications," *Radiographics*, vol. 29, no. 5, pp. 1433–1449, 2009.

[24] M. Versluis, J. van der Grond, M. van Buchem, P. van Zijl, and A. Webb, "High-field imaging of neurodegenerative diseases," *Neuroimaging Clin N Am*, vol. 22, no. 2, pp. 159–171, 2012.

[25] Y. Wang, Y. Yu, D. Li, K. T. Bae, J. J. Brown, W. Lin, and E. M. Haacke, "Artery and vein separation using susceptibility-dependent phase in contrast-enhanced MRA," *J Magn Reson Imaging*, vol. 12, no. 5, pp. 661–670, 2000.

[26] B. Yao, T.-Q. Li, P. v. Gelderen, K. Shmueli, J. A. de Zwart, and J. H. Duyn, "Susceptibility contrast in high field MRI of human brain as a function of tissue iron content," *Neuroimage*, vol. 44, no. 4, pp. 1259–1266, 2009.

[27] B. P. Thomas, E. B. Welch, B. D. Niederhauser, W. O. Whetsell, A. W. Anderson, J. C. Gore, M. J. Avison, and J. L. Creasy, "High-resolution 7T MRI of the human hippocampus in vivo," *J Magn Reson Imaging*, vol. 28, no. 5, pp. 1266–1272, 2008.

[28] A. M. Abduljalil, P. Schmalbrock, V. Novak, and D. W. Chakeres, "Enhanced gray and white matter contrast of phase susceptibility-weighted images in ultra-high-field magnetic resonance imaging," *J Magn Reson Imaging*, vol. 18, no. 3, pp. 284–290, 2003.

[29] D. H. Salat, S. Y. Lee, A. J. van der Kouwe, D. N. Greve, B. Fischl, and H. D. Rosas, "Age-associated alterations in cortical gray and white matter signal intensity and gray to white matter contrast," *Neuroimage*, vol. 48, no. 1, pp. 21–28, 2009.

[30] K. Hopp, B. F. G. Popescu, R. P. E. McCrea, S. L. Harder, C. A. Robinson, M. E. Haacke, A. H. Rajput, A. Rajput, and H. Nichol, "Brain iron detected by SWI high pass filtered phase calibrated with synchrotron X-ray fluorescence," *J Magn Reson Imaging*, vol. 31, no. 6, pp. 1346–1354, 2010.

[31] J. H. Duyn, "The future of ultra-high field MRI and fMRI for study of the human brain," *Neuroimage*, vol. 62, no. 2, pp. 1241–1248, 2012.

[32] E. Moser, F. Stahlberg, M. E. Ladd, and S. Trattnig, "7-T MR–from research to clinical applications?" *NMR Biomed*, vol. 25, no. 5, pp. 695–716, 2012.

[33] M. S. de Oliveira, M. L. F. Balthazar, A. D'Abreu, C. L. Yasuda, B. P. Damasceno, F. Cendes, and G. Castellano, "MR imaging texture analysis of the corpus callosum and thalamus in amnestic mild cognitive impairment and mild Alzheimer disease," *AJNR Am J Neuroradiol*, vol. 32, pp. 60–66, 2010.

[34] B. Julész, E. N. Gilbert, L. A. Shepp, and H. L. Frisch, "Inability of humans to discriminate between visual textures that agree in second-order statistics-revisited," *Perception*, vol. 2, no. 4, pp. 391–405, 1973.

[35] A. Kassner and R. E. Thornhill, "Texture analysis: a review of neurologic MR imaging applications," *AJNR Am J Neuroradiol*, vol. 31, no. 5, pp. 809–816, 2010.

[36] A. Materka, M. Strzelecki *et al.*, "Texture analysis methods-a review," *Technical University of Lodz, Institute of Electronics, COST B11 Report*, 1998.

[37] J.-K. Kamarainen, V. Kyrki, and H. Kalviainen, "Invariance properties of Gabor filter-based features-overview and applications," *IEEE Trans Image Process*, vol. 15, no. 5, pp. 1088 –1099, 2006.

[38] S. Drabycz, R. G. Stockwell, and J. R. Mitchell, "Image texture characterization using the discrete orthonormal S-transform," *J Digit Imaging*, vol. 22, no. 6, pp. 696–708, 2009.

[39] P. M. Szczypinski, M. Strzelecki, A. Materka, and A. Klepaczko, "MaZda–A software package for image texture analysis," *Comput Methods Programs Biomed*, vol. 94, no. 1, pp. 66–76, 2009.

[40] R. G. Stockwell, L. Mansinha, and R. P. Lowe, "Localization of the complex spectrum: The S transform," *IEEE Trans Signal Process*, vol. 44, no. 4, pp. 998–1001, 1996.

[41] R. M. Haralick, K. Shanmugam, and I. H. Dinstein, "Textural features for image classification," *IEEE Trans Syst, Man, Cybern*, vol. 3, no. 6, pp. 610–621, 1973.

[42] W. Chen, M. L. Giger, H. Li, U. Bick, and G. M. Newstead, "Volumetric texture analysis of breast lesions on contrast-enhanced magnetic resonance images," *Magn Reson Med*, vol. 58, no. 3, pp. 562–571, 2007.

[43] M. E. Mayerhoefer, P. Szomolanyi, D. Jirak, A. Materka, and S. Trattnig, "Effects of MRI acquisition parameter variations and protocol heterogeneity on the results of texture analysis and pattern discrimination: an application-oriented study," *Med Phys*, vol. 36, no. 4, pp. 1236–1243, 2009.

[44] S. Duchesne, N. Bernasconi, A. Bernasconi, and D. Collins, "MR-based neurological disease classification methodology: Application to lateralization of seizure focus in temporal lobe epilepsy," *Neuroimage*, vol. 29, no. 2, pp. 557–566, 2006.

[45] S. Duchesne, A. Caroli, C. Geroldi, C. Barillot, G. B. Frisoni, and D. L. Collins, "MRI-based automated computer classification of probable AD versus normal controls," *IEEE Trans Med Imaging*, vol. 27, no. 4, pp. 509–520, 2008.

[46] S. Duchesne, C. Bocti, K. De Sousa, G. B. Frisoni, H. Chertkow, and D. L. Collins, "Amnestic MCI future clinical status prediction using baseline MRI features," *Neurobiol Aging*, vol. 31, no. 9, pp. 1606–1617, 2010.

[47] H. C. Achterberg, F. Lijn, T. Heijer, A. Lugt, M. M. B. Breteler, W. J. Niessen, and M. Bruijne, "Prediction of dementia by hippocampal shape analysis," in *Machine Learning in Medical Imaging*. Springer, 2010, vol. 6357, pp. 42–49.

[48] S. V. Bharath Kumar, "Textural content in 3T MR: an image-based marker for Alzheimer's disease," in *Medical Imaging*, 2005, pp. 1366–1376.

[49] P. A. Freeborough and N. C. Fox, "MR image texture analysis applied to the diagnosis and tracking of Alzheimer's disease," *IEEE Trans Med Imaging*, vol. 17, no. 3, pp. 475–479, 1998.

[50] Y. Liu, L. Teverovskiy, O. Carmichael, R. Kikinis, M. Shenton, C. Carter, V. Stenger, S. Davis, H. Aizenstein, and J. Becker, "Discriminative MR image feature analysis for automatic schizophrenia and Alzheimer's disease classification," in *Medical Image Computing and Computer-Assisted Intervention – MICCAI*, vol. 3216, 2004, pp. 393–401.

[51] Y. Peng, Z. Wu, and J. Jiang, "A novel feature selection approach for biomedical data classification," *J Biomed Inform*, vol. 43, no. 1, pp. 15–23, 2010.

[52] J. Zhang, L. Tong, L. Wang, and N. Li, "Texture analysis of multiple sclerosis: a comparative study," *Magn Reson Imaging*, vol. 26, no. 8, pp. 1160–1166, 2008.

[53] J. Zhang, C. Yu, G. Jiang, W. Liu, and L. Tong, "3D texture analysis on MRI images of Alzheimer's disease," *Brain Imaging and Behavior*, vol. 6, no. 1, pp. 61–69, 2012.

[54] S. B. Antel, D. Collins, N. Bernasconi, F. Andermann, R. Shinghal, R. E. Kearney, D. L. Arnold, and A. Bernasconi, "Automated detection of focal cortical dysplasia lesions using computational models of their MRI characteristics and texture analysis," *Neuroimage*, vol. 19, no. 4, pp. 1748–1759, 2003.

[55] P. Georgiadis, D. Cavouras, I. Kalatzis, D. Glotsos, E. Athanasiadis, S. Kostopoulos, K. Sifaki, M. Malamas, G. Nikiforidis, and E. Solomou, "Enhancing the discrimination accuracy between metastases, gliomas and meningiomas on brain MRI by volumetric textural features and ensemble pattern recognition methods," *Magn Reson Imaging*, vol. 27, no. 1, pp. 120–130, 2009.

[56] P. Theocharakis, D. Glotsos, I. Kalatzis, S. Kostopoulos, P. Georgiadis, K. Sifaki, K. Tsakouridou, M. Malamas, G. Delibasis, D. Cavouras, and G. Nikiforidis, "Pattern recognition system for the discrimination of multiple sclerosis from cerebral microangiopathy lesions based on texture analysis of magnetic resonance images," *Magn Reson Imaging*, vol. 27, no. 3, pp. 417–422, 2009.

[57] T. Sankar, N. Bernasconi, H. Kim, and A. Bernasconi, "Temporal lobe epilepsy: Differential pattern of damage in temporopolar cortex and white matter," *Hum Brain Mapp*, vol. 29, no. 8, pp. 931–944, 2008.

[58] K. Jafari-Khouzani, K. Elisevich, S. Patel, B. Smith, and H. Soltanian-Zadeh, "FLAIR signal and texture analysis for lateralizing mesial temporal lobe epilepsy," *Neuroimage*, vol. 49, no. 2, pp. 1559–1571, 2010.

[59] Y. Zhang, H. Zhu, J. R. Mitchell, F. Costello, and L. M. Metz, "T2 MRI texture analysis is a sensitive measure of tissue injury and recovery resulting from acute inflammatory lesions in multiple sclerosis," *Neuroimage*, vol. 47, no. 1, pp. 107–111, 2009.

[60] M. d. C. Alegro, A. V. Silva, S. Y. Bando, R. d. D. Lopes, L. H. Martins de Castro, W. HungTsu, C. A. Moreira-Filho, and E. Amaro, "Texture analysis of high resolution MRI allows discrimination between febrile and afebrile initial precipitating injury in mesial temporal sclerosis," *Magn Reson Med*, vol. 68, pp. 1647–1653, 2012.

[61] M. Sikiö, K. K. Holli, L. C. Harrison, H. Ruottinen, M. Rossi, M. T. Helminen, P. Ryymin, R. Paalavuo, S. Soimakallio, H. J. Eskola, I. Elovaara, and P. Dastidar, "Parkinson's disease: Interhemispheric textural differences in MR images," *Acad Radiol*, vol. 18, no. 10, pp. 1217–1224, 2011.

[62] M. R. Sabuncu, R. S. Desikan, J. Sepulcre, B. T. Yeo, H. Liu, N. J. Schmansky, M. Reuter, M. W. Weiner, R. L. Buckner, R. A. Sperling, B. Fischl, and for the Alzheimer's Disease Neuroimaging Initiative, "The dynamics of cortical and hippocampal atrophy in Alzheimer disease," *Arch Neurol*, vol. 68, no. 8, pp. 1040–1048, 2011.

[63] L. de Jong, K. van der Hiele, I. Veer, J. Houwing, R. Westendorp, E. Bollen, P. de Bruin, H. Middelkoop, M. van Buchem, and J. van der Grond, "Strongly reduced volumes of putamen and thalamus in Alzheimer's disease: an MRI study," *Brain*, vol. 131, no. 12, pp. 3277–3285, 2008.

[64] E. Cavedo, M. Boccardi, R. Ganzola, E. Canu, A. Beltramello, C. Caltagirone, P. M. Thompson, and G. B. Frisoni, "Local amygdala structural differences with 3T MRI in patients with Alzheimer disease," *Neurology*, vol. 76, no. 8, pp. 727–733, 2011.

[65] L. Ferrarini, W. M. Palm, H. Olofsen, R. van der Landen, M. A. van Buchem, J. H. C. Reiber, and F. Admiraal-Behloul, "Ventricular shape biomarkers for Alzheimer's disease in clinical MR images," *Magn Reson Med*, vol. 59, no. 2, pp. 260–267, 2008.

[66] J. Ashburner, C. Hutton, R. Frackowiak, I. Johnsrude, C. Price, and K. Friston, "Identifying global anatomical differences: Deformation-based morphometry," *Hum Brain Mapp*, vol. 6, no. 5-6, pp. 348–357, 1998.

[67] S. Klein, M. Loog, F. van der Lijn, T. den Heijer, A. Hammers, M. de Bruijne, A. van der Lugt, R. Duin, M. Breteler, and W. Niessen, "Early diagnosis of dementia based on intersubject whole-brain dissimilarities," in *Biomedical Imaging: From Nano to Macro, 2010 IEEE International Symposium on*, 2010, pp. 249 –252.

[68] J. J. M. Zwanenburg, M. J. Versluis, P. R. Luijten, and N. Petridou, "Fast high resolution whole brain T2* weighted imaging using echo planar imaging at 7T," *Neuroimage*, vol. 56, pp. 1902–1907, 2011.

[69] T.-Q. Li, P. van Gelderen, H. Merkle, L. Talagala, A. P. Koretsky, and J. Duyn, "Extensive heterogeneity in white matter intensity in high-resolution T2*-weighted MRI of the human brain at 7.0 T," *Neuroimage*, vol. 32, no. 3, pp. 1032–1040, 2006.

[70] J. Hagemeier, B. Weinstock-Guttman, N. Bergsland, M. H. Brown, E. Carl, C. Kennedy, C. Magnano, D. Hojnacki, M. G. Dwyer, and R. Zivadinov, "Iron deposition on SWI-filtered phase in the subcortical deep gray matter of patients with clinically isolated syndrome may precede structure-specific atrophy," *AJNR Am J Neuroradiol*, vol. 33, pp. 1596–1601, 2012.

[71] R. Zivadinov, M. Heininen-Brown, C. V. Schirda, G. U. Poloni, N. Bergsland, C. R. Magnano, J. Durfee, C. Kennedy, E. Carl, J. Hagemeier, R. H. Benedict, B. Weinstock-Guttman, and M. G. Dwyer, "Abnormal subcortical deep-gray matter susceptibility-weighted imaging filtered phase measurements in patients with multiple sclerosis: A case-control study," *Neuroimage*, vol. 59, no. 1, pp. 331–339, 2012.

[72] J. H. Duyn, P. van Gelderen, T.-Q. Li, J. A. de Zwart, A. P. Koretsky, and M. Fukunaga, "High-field MRI of brain cortical substructure based on signal phase," *Proc Natl Acad Sci U S A*, vol. 104, no. 28, pp. 11 796–11 801, 2007.

[73] W. Zhu, W. Zhong, W. Wang, C. Zhan, C. Wang, J. Qi, J. Wang, and T. Lei, "Quantitative MR phase-corrected imaging to investigate increased brain iron deposition of patients with Alzheimer disease," *Radiology*, vol. 253, no. 2, pp. 497–504, 2009.

[74] R. Roos and G. Bots, "Nuclear membrane indentations in Huntington's chorea," *J Neurol Sci*, vol. 61, no. 1, pp. 37–47, 1983.

[75] R. A. Roos, J. F. Pruyt, J. de Vries, and G. T. Bots, "Neuronal distribution in the putamen in Huntington's disease," *J Neurol Neurosurg Psychiatry*, vol. 48, no. 5, pp. 422–425, 1985.

[76] J. P. Vonsattel and M. DiFiglia, "Huntington disease," *J Neuropathol Exp Neurol*, vol. 57, no. 5, pp. 369–384, 1998.

[77] D. T. Dexter, A. Carayon, F. Javoy-Agid, Y. Agid, F. R. Wells, S. E. Daniel, A. J. Lees, P. Jenner, and C. D. Marsden, "Alterations in the levels of iron, ferritin and other trace metals in Parkinson's disease and other neurodegenerative diseases affecting the basal ganglia," *Brain*, vol. 114, no. 4, pp. 1953–1975, 1991.

[78] G. Bartzokis, P. H. Lu, T. A. Tishler, S. M. Fong, B. Oluwadara, J. P. Finn, D. Huang, Y. Bordelon, J. Mintz, and S. Perlman, "Myelin breakdown and iron changes in Huntington's disease: pathogenesis and treatment implications," *Neurochem Res*, vol. 32, no. 10, pp. 1655–1664, 2007.

[79] J. Vymazal, J. Klempíř, R. Jech, J. Zidovská, M. Syka, E. Ruzicka, and J. Roth, "MR relaxometry in Huntington's disease: Correlation between imaging, genetic and clinical parameters," *J Neurol Sci*, vol. 263, no. 1-2, pp. 20–25, 2007.

[80] C. K. Jurgens, R. Jasinschi, A. Ekin, M.-N. W. Witjes-Ané, J. van der Grond, H. Middelkoop, and R. A. Roos, "MRI T2 hypointensities in basal ganglia of premanifest Huntington's disease," *PLoS Curr*, vol. 2, 2010.

[81] B. Belaroussi, J. Milles, S. Carme, Y. M. Zhu, and H. Benoit-Cattin, "Intensity non-uniformity correction in MRI: existing methods and their validation," *Med Image Anal*, vol. 10, no. 2, pp. 234–246, 2006.

[82] J. G. Sled, A. P. Zijdenbos, and A. C. Evans, "A nonparametric method for automatic correction of intensity nonuniformity in MRI data," *IEEE Trans Med Imaging*, vol. 17, no. 1, pp. 87–97, 1998.

[83] M. J. McAuliffe, F. M. Lalonde, D. McGarry, W. Gandler, K. Csaky, and B. L. Trus, "Medical image processing, analysis and visualization in clinical research," in *Computer-Based Medical Systems, 2001. CBMS 2001. Proceedings. 14th IEEE Symposium on*, 2002, pp. 381–386.

[84] B. Patenaude, S. M. Smith, D. N. Kennedy, and M. Jenkinson, "A Bayesian model of shape and appearance for subcortical brain segmentation," *Neuroimage*, vol. 56, no. 3, pp. 907–922, 2011.

[85] S. Klein, M. Staring, K. Murphy, M. A. Viergever, and J. Pluim, "elastix: A toolbox for intensity-based medical image registration," *IEEE Trans Med Imaging*, vol. 29, no. 1, pp. 196–205, 2010.

[86] M. Hollander and D. A. Wolfe, *Nonparametric Statistical Methods*. NY John Wiley & Sons, 1999.

[87] J. P. G. Vonsattel, C. Keller, and E. P. Cortes Ramirez, "Huntington's disease - neuropathology," *Handbook of Clinical Neurology / Edited by P.J. Vinken and G.W. Bruyn*, vol. 100, pp. 83–100, 2011.

[88] H. H. Ruocco, I. Lopes-Cendes, L. M. Li, M. Santos-Silva, and F. Cendes, "Striatal and extrastriatal atrophy in Huntington's disease and its relationship with length of the CAG repeat," *Braz J Med Biol Res*, vol. 39, no. 8, pp. 1129–1136, 2006.

[89] A. Peinemann, S. Schuller, C. Pohl, T. Jahn, A. Weindl, and J. Kassubek, "Executive dysfunction in early stages of Huntington's disease is associated with striatal and insular atrophy: A neuropsychological and voxel-based morphometric study," *J Neurol Sci*, vol. 239, no. 1, pp. 11–19, 2005.

[90] J. Kassubek, F. D. Juengling, D. Ecker, and G. B. Landwehrmeyer, "Thalamic atrophy in Huntington's disease co-varies with cognitive performance: A morphometric MRI analysis," *Cereb Cortex*, vol. 15, no. 6, pp. 846–853, 2005.

[91] J. F. Schenck and E. A. Zimmerman, "High-field magnetic resonance imaging of brain iron: birth of a biomarker?" *NMR Biomed*, vol. 17, no. 7, pp. 433–445, 2004.

[92] H. D. Rosas, A. K. Liu, S. Hersch, M. Glessner, R. J. Ferrante, D. H. Salat, A. van der Kouwe, B. G. Jenkins, A. M. Dale, and B. Fischl, "Regional and progressive thinning of the cortical ribbon in Huntington's disease," *Neurology*, vol. 58, no. 5, pp. 695–701, 2002.

[93] P. C. Nopoulos, E. H. Aylward, C. A. Ross, H. J. Johnson, V. A. Magnotta, A. R. Juhl, R. K. Pierson, J. Mills, D. R. Langbehn, and J. S. Paulsen, "Cerebral cortex structure in prodromal Huntington disease," *Neurobiol Dis*, vol. 40, no. 3, pp. 544–554, 2010.

[94] B. C. Dickerson, A. Bakkour, D. H. Salat, E. Feczko, J. Pacheco, D. N. Greve, F. Grodstein, C. I. Wright, D. Blacker, H. D. Rosas, R. A. Sperling, A. Atri, J. H. Growdon, B. T. Hyman, J. C. Morris, B. Fischl, and R. L. Buckner, "The cortical signature of Alzheimer's disease: regionally specific cortical thinning relates to symptom severity in very mild to mild AD dementia and is detectable in asymptomatic amyloid-positive individuals," *Cereb Cortex*, vol. 19, no. 3, pp. 497–510, 2009.

[95] T. D. Cannon, P. M. Thompson, T. G. M. van Erp, A. W. Toga, V.-P. Poutanen, M. Huttunen, J. Lonnqvist, C.-G. Standerskjold-Nordenstam, K. L. Narr, M. Khaledy, C. I. Zoumalan, R. Dail, and J. Kaprio, "Cortex mapping reveals regionally specific patterns of genetic and disease-specific gray-matter deficits in twins discordant for schizophrenia," *Proc Natl Acad Sci U S A*, vol. 99, no. 5, pp. 3228–3233, 2002.

[96] A. Fornito, M. Yücel, B. Dean, S. J. Wood, and C. Pantelis, "Anatomical abnormalities of the anterior cingulate cortex in schizophrenia: bridging the gap between neuroimaging and neuropathology," *Schizophr Bull*, vol. 35, no. 5, pp. 973–993, 2009.

[97] S. M. Wolosin, M. E. Richardson, J. G. Hennessey, M. B. Denckla, and S. H. Mostofsky, "Abnormal cerebral cortex structure in children with ADHD," *Hum Brain Mapp*, vol. 30, no. 1, pp. 175–184, 2009.

[98] J. A. Duce, A. Tsatsanis, M. A. Cater, S. A. James, E. Robb, K. Wikhe, S. L. Leong, K. Perez, T. Johanssen, M. A. Greenough, H.-H. Cho, D. Galatis, R. D. Moir, C. L. Masters, C. McLean, R. E. Tanzi, R. Cappai, K. J. Barnham, G. D. Ciccotosto, J. T. Rogers, and A. I. Bush, "Iron-export ferroxidase activity of β-amyloid precursor protein is inhibited by zinc in Alzheimer's disease," *Cell*, vol. 142, no. 6, pp. 857–867, 2010.

[99] D. J. Piñero and J. R. Connor, "Iron in the brain: An important contributor in normal and diseased states," *Neuroscientist*, vol. 6, no. 6, pp. 435 –453, 2000.

[100] M. A. Smith, X. Zhu, M. Tabaton, G. Liu, J. McKeel, M. L. Cohen, X. Wang, S. L. Siedlak, B. E. Dwyer, T. Hayashi, M. Nakamura, A. Nunomura, and G. Perry, "Increased iron and free radical generation in preclinical Alzheimer disease and mild cognitive impairment," *J Alzheimers Dis*, vol. 19, no. 1, pp. 363–372, 2010.

[101] M. D. Meadowcroft, J. R. Connor, M. B. Smith, and Q. X. Yang, "MRI and histological analysis of beta-amyloid plaques in both human Alzheimer's disease and APP/PS1 transgenic mice," *J Magn Reson Imaging*, vol. 29, no. 5, pp. 997–1007, 2009.

[102] A. M. Dale, B. Fischl, and M. I. Sereno, "Cortical surface-based analysis. I. segmentation and surface reconstruction," *Neuroimage*, vol. 9, no. 2, pp. 179–194, 1999.

[103] X. Zeng, L. H. Staib, R. T. Schultz, and J. S. Duncan, "Segmentation and measurement of the cortex from 3-D MR images using coupled-surfaces propagation," *IEEE Trans Med Imaging*, vol. 18, no. 10, pp. 927–937, 2002.

[104] D. MacDonald, N. Kabani, D. Avis, and A. C. Evans, "Automated 3-D extraction of inner and outer surfaces of cerebral cortex from MRI," *Neuroimage*, vol. 12, no. 3, pp. 340–356, 2000.

[105] C. R. Jack, M. A. Bernstein, N. C. Fox, P. Thompson, G. Alexander, D. Harvey, B. Borowski, P. J. Britson, J. L. Whitwell, C. Ward, A. M. Dale, J. P. Felmlee, J. L. Gunter, D. L. Hill, R. Killiany, N. Schuff, S. Fox-Bosetti, C. Lin, C. Studholme, C. S. DeCarli, G. Krueger, H. A. Ward, G. J. Metzger, K. T. Scott, R. Mallozzi, D. Blezek, J. Levy, J. P. Debbins, A. S. Fleisher, M. Albert, R. Green, G. Bartzokis, G. Glover, J. Mugler, and M. W. Weiner, "The Alzheimer's disease neuroimaging initiative (ADNI): MRI methods," *J Magn Reson Imaging*, vol. 27, no. 4, pp. 685–691, 2008.

[106] P. Bourgeat, J. Fripp, P. Stanwell, S. Ramadan, and S. Ourselin, "MR image segmentation of the knee bone using phase information," *Med Image Anal*, vol. 11, no. 4, pp. 325–335, 2007.

[107] D. S. J. Pandian, C. Ciulla, E. M. Haacke, J. Jiang, and M. Ayaz, "Complex threshold method for identifying pixels that contain predominantly noise in magnetic resonance images," *J Magn Reson Imaging*, vol. 28, no. 3, pp. 727–735, 2008.

[108] A. K. Jain and R. C. Dubes, *Algorithms for Clustering Data*. Prentice-Hall, Inc., 1988.

[109] R. C. Gonzalez and R. E. Woods, *Digital Image Processing, 2nd ed.* Prentice Hall, 2002.

[110] L. Vincent, "Morphological grayscale reconstruction in image analysis: applications and efficient algorithms," *IEEE Trans Image Process*, vol. 2, no. 2, pp. 176–201, 1993.

[111] I. Santillán, A. M. Herrera-Navarro, J. D. Mendiola-Santibáñez, and I. R. Terol-Villalobos, "Morphological connected filtering on viscous lattices," *J Math Imaging Vis*, vol. 36, no. 3, pp. 254–269, 2009.

[112] I. R. Terol-Villalobos and D. Vargas-Vázquez, "Openings and closings by reconstruction using propagation criteria," in *Computer Analysis of Images and Patterns*. Springer, 2001, pp. 502–509.

[113] I. R. Terol-Villalobos, J. D. Mendiola-Santibáñez, and S. L. Canchola-Magdaleno, "Image segmentation and filtering based on transformations with reconstruction criteria," *J Vis Commun Image R*, vol. 17, no. 1, pp. 107–130, 2006.

[114] M. J. Versluis, J. M. Peeters, S. van Rooden, J. van der Grond, M. A. van Buchem, A. G. Webb, and M. J. P. van Osch, "Origin and reduction of motion and f0 artifacts in high resolution T2*-weighted magnetic resonance imaging: application in Alzheimer's disease patients," *Neuroimage*, vol. 51, no. 3, pp. 1082–1088, 2010.

[115] L. R. Dice, "Measures of the amount of ecologic association between species," *Ecology*, vol. 26, no. 3, pp. 297–302, 1945.

[116] J. M. Bland and D. G. Altman, "Statistical methods for assessing agreement between two methods of clinical measurement," *Int J Nurs Stud*, vol. 47, no. 8, pp. 931–936, 2010.

[117] P. A. Yushkevich, J. Piven, H. C. Hazlett, R. G. Smith, S. Ho, J. C. Gee, and G. Gerig, "User-guided 3D active contour segmentation of anatomical structures: significantly improved efficiency and reliability," *Neuroimage*, vol. 31, no. 3, pp. 1116–1128, 2006.

[118] S. Magnaldi, M. Ukmar, A. Vasciaveo, R. Longo, and R. Pozzi-Mucelli, "Contrast between white and grey matter: MRI appearance with ageing," *Eur Radiol*, vol. 3, no. 6, pp. 513–519, 1993.

[119] B. Hallgren and P. Sourander, "The effect of age on the non-haemin iron in the human brain," *J Neurochem*, vol. 3, no. 1, pp. 41–51, 1958.

[120] D. H. Salat, R. L. Buckner, A. Z. Snyder, D. N. Greve, R. S. R. Desikan, E. Busa, J. C. Morris, A. M. Dale, and B. Fischl, "Thinning of the cerebral cortex in aging," *Cereb Cortex*, vol. 14, no. 7, pp. 721–730, 2004.

[121] X. Xu, Q. Wang, and M. Zhang, "Age, gender, and hemispheric differences in iron deposition in the human brain: An in vivo MRI study," *Neuroimage*, vol. 40, no. 1, pp. 35–42, 2008.

[122] J. Zhang, Y. Zhang, J. Wang, P. Cai, C. Luo, Z. Qian, Y. Dai, and H. Feng, "Characterizing iron deposition in Parkinson's disease using susceptibility-weighted imaging: an in vivo MR study," *Brain Res*, vol. 1330, pp. 124–130, 2010.

[123] N. T. Doan, S. van Rooden, M. J. Versluis, A. G. Webb, J. van der Grond, M. A. van Buchem, J. H. C. Reiber, and J. Milles, "Combined magnitude and phase-based segmentation of the cerebral cortex in 7T MR images of the elderly," *J Magn Reson Imaging*, vol. 36, no. 1, pp. 99–109, 2012.

[124] R. J. Ogg, J. W. Langston, E. M. Haacke, R. G. Steen, and J. S. Taylor, "The correlation between phase shifts in gradient-echo MR images and regional brain iron concentration," *Magn Reson Imaging*, vol. 17, no. 8, pp. 1141–1148, 1999.

[125] S. van Rooden, M. J. Versluis, M. K. Liem, J. Milles, A. B. Maier, A. M. Oleksik, A. G. Webb, M. A. van Buchem, and J. van der Grond, "Cortical phase changes in Alzheimer's disease at 7T MRI: A novel imaging marker," *Alzheimers Dement*, vol. 10, no. 1, pp. e19–e26, 2014.

[126] D. L. Collins, P. Neelin, T. M. Peters, and A. C. Evans, "Automatic 3D intersubject registration of MR volumetric data in standardized Talairach space," *J Comput Assist Tomogr*, vol. 18, no. 2, pp. 192–205, 1994.

[127] B. Fischl and A. M. Dale, "Measuring the thickness of the human cerebral cortex from magnetic resonance images," *Proc Natl Acad Sci U S A*, vol. 97, no. 20, pp. 11 050–11 055, 2000.

[128] N. Tzourio-Mazoyer, B. Landeau, D. Papathanassiou, F. Crivello, O. Etard, N. Delcroix, B. Mazoyer, and M. Joliot, "Automated anatomical labeling of activations in SPM using a macroscopic anatomical parcellation of the MNI MRI single-subject brain," *Neuroimage*, vol. 15, no. 1, pp. 273–289, 2002.

[129] H. B. Mann and D. R. Whitney, "On a test of whether one of two random variables is stochastically larger than the other," *Ann Math Statist*, vol. 18, no. 1, pp. 50–60, 1947.

[130] R. C. Blair and W. Karniski, "An alternative method for significance testing of waveform difference potentials," *Psychophysiology*, vol. 30, no. 5, pp. 518–524, 1993.

[131] T. E. Nichols and A. P. Holmes, "Nonparametric permutation tests for functional neuroimaging: a primer with examples," *Hum Brain Mapp*, vol. 15, no. 1, pp. 1–25, 2002.

[132] L. Ferrarini, W. M. Palm, H. Olofsen, M. A. van Buchem, J. H. C. Reiber, and F. Admiraal-Behloul, "Shape differences of the brain ventricles in Alzheimer's disease," *Neuroimage*, vol. 32, no. 3, pp. 1060–1069, 2006.

[133] L. T. Westlye, K. B. Walhovd, A. M. Dale, T. Espeseth, I. Reinvang, N. Raz, I. Agartz, D. N. Greve, B. Fischl, and A. M. Fjell, "Increased sensitivity to effects of normal aging and Alzheimer's disease on cortical thickness by adjustment for local variability in gray/white contrast: a multi-sample MRI study," *Neuroimage*, vol. 47, no. 4, pp. 1545–1557, 2009.

[134] C. Langkammer, N. Krebs, W. Goessler, E. Scheurer, K. Yen, F. Fazekas, and S. Ropele, "Susceptibility induced gray-white matter MRI contrast in the human brain," *Neuroimage*, vol. 59, no. 2, pp. 1413–1419, 2012.

[135] J. Lee, Y. Hirano, M. Fukunaga, A. C. Silva, and J. H. Duyn, "On the contribution of deoxy-hemoglobin to MRI gray-white matter phase contrast at high field," *Neuroimage*, vol. 49, no. 1, pp. 193–198, 2010.

[136] J. Lee, K. Shmueli, B.-T. Kang, B. Yao, M. Fukunaga, P. van Gelderen, S. Palumbo, F. Bosetti, A. C. Silva, and J. H. Duyn, "The contribution of myelin to magnetic susceptibility-weighted contrasts in high-field MRI of the brain," *Neuroimage*, vol. 59, no. 4, pp. 3967–3975, 2012.

[137] E. R. Sowell, B. S. Peterson, P. M. Thompson, S. E. Welcome, A. L. Henkenius, and A. W. Toga, "Mapping cortical change across the human life span," *Nat Neurosci*, vol. 6, no. 3, pp. 309–315, 2003.

[138] O. Piguet, K. Double, J. Kril, J. Harasty, V. Macdonald, D. McRitchie, and G. Halliday, "White matter loss in healthy ageing: a postmortem analysis," *Neurobiol Aging*, vol. 30, no. 8, pp. 1288–1295, 2009.

[139] A. Giorgio, L. Santelli, V. Tomassini, R. Bosnell, S. Smith, N. De Stefano, and H. Johansen-Berg, "Age-related changes in grey and white matter structure throughout adulthood," *Neuroimage*, vol. 51, no. 3, pp. 943–951, 2010.

[140] G. Bartzokis, P. H. Lu, K. Tingus, M. F. Mendez, A. Richard, D. G. Peters, B. Oluwadara, K. A. Barrall, J. P. Finn, P. Villablanca, P. M. Thompson, and J. Mintz, "Lifespan trajectory of myelin integrity and maximum motor speed," *Neurobiol Aging*, vol. 31, no. 9, pp. 1554–1562, 2010.

[141] G. Bartzokis, P. H. Lu, P. Heydari, A. Couvrette, G. J. Lee, G. Kalashyan, F. Freeman, J. W. Grinstead, P. Villablanca, J. P. Finn, J. Mintz, J. R. Alger, and L. L. Altshuler, "Multimodal magnetic resonance imaging assessment of white matter aging trajectories over the lifespan of healthy individuals," *Biol Psychiatry*, vol. 72, no. 12, pp. 1026–1034, 2012.

[142] P. Vasudevaraju, Bharathi, J. T, N. M. Shamasundar, K. Subba Rao, B. M. Balaraj, R. Ksj, and S. R. T S, "New evidence on iron, copper accumulation and zinc depletion and its correlation with DNA integrity in aging human brain regions," *Indian J Psychiatry*, vol. 52, no. 2, pp. 140–144, 2010.

[143] A. Deistung, A. Schäfer, F. Schweser, U. Biedermann, R. Turner, and J. R. Reichenbach, "Toward in vivo histology: A comparison of quantitative susceptibility mapping (QSM) with magnitude-, phase-, and R2*-imaging at ultra-high magnetic field strength," *Neuroimage*, vol. 65, pp. 299–314, 2013.

[144] C. Langkammer, T. Liu, M. Khalil, C. Enzinger, M. Jehna, S. Fuchs, F. Fazekas, Y. Wang, and S. Ropele, "Quantitative susceptibility mapping in multiple sclerosis," *Radiology*, vol. 267, pp. 551–559, 2013.

[145] C. P. Ferri, M. Prince, C. Brayne, H. Brodaty, L. Fratiglioni, M. Ganguli, K. Hall, K. Hasegawa, H. Hendrie, Y. Huang, A. Jorm, C. Mathers, P. R. Menezes, E. Rimmer, M. Scazufca, and for Alzheimer's Disease International, "Global prevalence of dementia: a Delphi consensus study," *Lancet*, vol. 366, no. 9503, pp. 2112–2117, 2005.

[146] L. Minati, T. Edginton, M. G. Bruzzone, and G. Giaccone, "Current concepts in Alzheimer's disease: a multidisciplinary review," *Am J Alzheimers Dis Other Demen*, vol. 24, no. 2, pp. 95–121, 2009.

[147] T. Imamura, Y. Takatsuki, M. Fujimori, N. Hirono, Y. Ikejiri, T. Shimomura, M. Hashimoto, H. Yamashita, and E. Mori, "Age at onset and language disturbances in Alzheimer's disease," *Neuropsychologia*, vol. 36, no. 9, pp. 945–949, 1998.

[148] D. Jacobs, M. Sano, K. Marder, K. Bell, F. Bylsma, G. Lafleche, M. Albert, J. Brandt, and Y. Stern, "Age at onset of Alzheimer's disease: relation to pattern of cognitive dysfunction and rate of decline," *Neurology*, vol. 44, no. 7, pp. 1215–1220, 1994.

[149] E. Koss, S. Edland, G. Fillenbaum, R. Mohs, C. Clark, D. Galasko, and J. C. Morris, "Clinical and neuropsychological differences between patients with earlier and later onset of Alzheimer's disease: A CERAD analysis, Part XII," *Neurology*, vol. 46, no. 1, pp. 136–141, 1996.

[150] F. Sá, P. Pinto, C. Cunha, R. Lemos, L. Letra, M. Simões, and I. Santana, "Differences between early and late-onset Alzheimer's disease in neuropsychological tests," *Front Neurol*, vol. 3, p. 81, 2012.

[151] L. L. Smits, Y. A. L. Pijnenburg, E. L. G. E. Koedam, A. E. van der Vlies, I. E. W. Reuling, T. Koene, C. E. Teunissen, P. Scheltens, and W. M. van der Flier, "Early onset Alzheimer's disease is associated with a distinct neuropsychological profile," *J Alzheimers Dis*, vol. 30, no. 1, pp. 101–108, 2012.

[152] A. E. van der Vlies, E. L. G. E. Koedam, Y. A. L. Pijnenburg, J. W. R. Twisk, P. Scheltens, and W. M. van der Flier, "Most rapid cognitive decline in APOE ϵ4 negative Alzheimer's disease with early onset," *Psychol Med*, vol. 39, no. 11, pp. 1907–1911, 2009.

[153] M. Balasa, E. Gelpi, A. Antonell, M. J. Rey, R. Sánchez-Valle, J. L. Molinuevo, A. Lladó, and Neurological Tissue Bank/University of Barcelona/Hospital Clínic NTB/UB/HC Collaborative Group, "Clinical features and APOE genotype of pathologically proven early-onset Alzheimer disease," *Neurology*, vol. 76, no. 20, pp. 1720–1725, 2011.

[154] E. L. G. E. Koedam, V. Lauffer, A. E. van der Vlies, W. M. van der Flier, P. Scheltens, and Y. A. L. Pijnenburg, "Early-versus late-onset Alzheimer's disease: more than age alone," *J Alzheimers Dis*, vol. 19, no. 4, pp. 1401–1408, 2010.

[155] G. B. Frisoni, M. Pievani, C. Testa, F. Sabattoli, L. Bresciani, M. Bonetti, A. Beltramello, K. M. Hayashi, A. W. Toga, and P. M. Thompson, "The topography of grey matter involvement in early and late onset Alzheimer's disease," *Brain*, vol. 130, no. 3, pp. 720–730, 2007.

[156] C. Möller, H. Vrenken, L. Jiskoot, A. Versteeg, F. Barkhof, P. Scheltens, and W. M. van der Flier, "Different patterns of gray matter atrophy in early- and late-onset Alzheimer's disease," *Neurobiol Aging*, vol. 34, no. 8, pp. 2014–2022, 2013.

[157] E. J. Kim, S. S. Cho, Y. Jeong, K. C. Park, S. J. Kang, E. Kang, S. E. Kim, K. H. Lee, and D. L. Na, "Glucose metabolism in early onset versus late onset Alzheimer's disease: an SPM analysis of 120 patients," *Brain*, vol. 128, no. 8, pp. 1790–1801, 2005.

[158] R. Ossenkoppele, M. D. Zwan, N. Tolboom, D. M. E. van Assema, S. F. Adriaanse, R. W. Kloet, R. Boellaard, A. D. Windhorst, F. Barkhof, A. A. Lammertsma, P. Scheltens, W. M. van der Flier, and B. N. M. van Berckel, "Amyloid burden and metabolic function in early-onset Alzheimer's disease: parietal lobe involvement," *Brain*, vol. 135, no. 7, pp. 2115–2125, 2012.

[159] G. D. Rabinovici, A. J. Furst, A. Alkalay, C. A. Racine, J. P. O'Neil, M. Janabi, S. L. Baker, N. Agarwal, S. J. Bonasera, E. C. Mormino, M. W. Weiner, M. L. Gorno-Tempini, H. J. Rosen, B. L. Miller, and W. J. Jagust, "Increased metabolic vulnerability in early-onset Alzheimer's disease is not related to amyloid burden," *Brain*, vol. 133, no. 2, pp. 512–528, 2010.

[160] H. Cho, S. Jeon, S. J. Kang, J.-M. Lee, J.-H. Lee, G. H. Kim, J. S. Shin, C. H. Kim, Y. Noh, K. Im, S. T. Kim, J. Chin, S. W. Seo, and D. L. Na, "Longitudinal changes of cortical thickness in early-versus late-onset Alzheimer's disease," *Neurobiol Aging*, vol. 34, no. 7, pp. 1921.e9–1921.e15, 2013.

[161] N. C. Kaiser, R. J. Melrose, C. Liu, D. L. Sultzer, E. Jimenez, M. Su, L. Monserratt, and M. F. Mendez, "Neuropsychological and neuroimaging markers in early versus late-onset Alzheimer's disease," *Am J Alzheimers Dis Other Demen*, vol. 27, no. 7, pp. 520–529, 2012.

[162] E. H. Bigio, L. S. Hynan, E. Sontag, S. Satumtira, and C. L. White, "Synapse loss is greater in presenile than senile onset Alzheimer disease: implications for the cognitive reserve hypothesis," *Neuropathol Appl Neurobiol*, vol. 28, no. 3, pp. 218–227, 2002.

[163] G. J. Ho, L. A. Hansen, M. F. Alford, K. Foster, D. P. Salmon, D. Galasko, L. J. Thal, and E. Masliah, "Age at onset is associated with disease severity in lewy body variant and Alzheimer's disease," *Neuroreport*, vol. 13, no. 14, pp. 1825–1828, 2002.

[164] G. A. Marshall, L. A. Fairbanks, S. Tekin, H. V. Vinters, and J. L. Cummings, "Early-onset Alzheimer's disease is associated with greater pathologic burden," *J Geriatr Psychiatry Neurol*, vol. 20, no. 1, pp. 29–33, 2007.

[165] I. H. Choo, D. Y. Lee, J. W. Kim, E. H. Seo, D. S. Lee, Y. K. Kim, S. G. Kim, S. Y. Park, J. I. Woo, and E. J. Yoon, "Relationship of amyloid-β burden with age-at-onset in Alzheimer disease," *Am J Geriatr Psychiatry*, vol. 19, no. 7, pp. 627–634, 2011.

[166] T. Nakada, H. Matsuzawa, H. Igarashi, Y. Fujii, and I. L. Kwee, "In vivo visualization of senile-plaque-like pathology in alzheimer's disease patients by MR microscopy on a 7T system," *J Neuroimaging*, vol. 18, no. 2, pp. 125–129, 2008.

[167] N. T. Doan, S. van Rooden, M. J. Versluis, M. Buijs, A. G. Webb, J. van der Grond, M. A. van Buchem, J. H. C. Reiber, and J. Milles, "Group-wise cortical feature analysis using high field T2*-weighted MR images highlights local differences between young and elderly healthy subjects," *Neuroimage*, 2013, submitted.

[168] N. Lynöe, M. Sandlund, G. Dahlqvist, and L. Jacobsson, "Informed consent: study of quality of information given to participants in a clinical trial," *Br Med J*, vol. 303, no. 6803, pp. 610–613, 1991.

[169] G. McKhann, D. Drachman, M. Folstein, R. Katzman, D. Price, and E. M. Stadlan, "Clinical diagnosis of Alzheimer's disease: report of the nincds-adrda work group under the auspices of department of health and human services task force on Alzheimer's disease," *Neurology*, vol. 34, no. 7, pp. 939–944, 1984.

[170] M. Schär, S. Kozerke, S. E. Fischer, and P. Boesiger, "Cardiac SSFP imaging at 3 Tesla," *Magn Reson Med*, vol. 51, no. 4, pp. 799–806, 2004.

[171] E. M. Haacke, Y. Xu, Y.-C. N. Cheng, and J. R. Reichenbach, "Susceptibility weighted imaging (SWI)," *Magn Reson Med*, vol. 52, no. 3, pp. 612–618, 2004.

[172] P. Lei, S. Ayton, D. I. Finkelstein, L. Spoerri, G. D. Ciccotosto, D. K. Wright, B. X. W. Wong, P. A. Adlard, R. A. Cherny, L. Q. Lam, B. R. Roberts, I. Volitakis, G. F. Egan, C. A. McLean, R. Cappai, J. A. Duce, and A. I. Bush, "Tau deficiency induces parkinsonism with dementia by impairing app-mediated iron export," *Nat Med*, vol. 18, no. 2, pp. 291–295, 2012.

[173] M. A. Smith, P. L. Harris, L. M. Sayre, and G. Perry, "Iron accumulation in Alzheimer disease is a source of redox-generated free radicals," *Proc Natl Acad Sci U S A*, vol. 94, no. 18, pp. 9866–9868, 1997.

[174] S. van Rooden, M. L. C. Maat-Schieman, R. J. A. Nabuurs, L. van der Weerd, S. van Duijn, S. G. van Duinen, R. Natté, M. A. van Buchem, and J. van der Grond, "Cerebral amyloidosis: postmortem detection with human 7.0-T MR imaging system," *Radiology*, vol. 253, no. 3, pp. 788–796, 2009.

[175] E. M. Haacke, N. Y. C. Cheng, M. J. House, Q. Liu, J. Neelavalli, R. J. Ogg, A. Khan, M. Ayaz, W. Kirsch, and A. Obenaus, "Imaging iron stores in the brain using magnetic resonance imaging," *Magn Reson Imaging*, vol. 23, no. 1, pp. 1–25, 2005.

[176] E. M. Haacke, M. Ayaz, A. Khan, E. S. Manova, B. Krishnamurthy, L. Gollapalli, C. Ciulla, I. Kim, F. Petersen, and W. Kirsch, "Establishing a baseline phase behavior in magnetic resonance imaging to determine normal vs. abnormal iron content in the brain," *J Magn Reson Imaging*, vol. 26, no. 2, pp. 256–264, 2007.

[177] E. Canu, G. B. Frisoni, F. Agosta, M. Pievani, M. Bonetti, and M. Filippi, "Early and late onset Alzheimer's disease patients have distinct patterns of white matter damage," *Neurobiol Aging*, vol. 33, no. 6, pp. 1023–1033, 2012.

[178] K. Ishii, T. Kawachi, H. Sasaki, A. K. Kono, T. Fukuda, Y. Kojima, and E. Mori, "Voxel-based morphometric comparison between early-and late-onset mild Alzheimer's disease and assessment of diagnostic performance of z score images," *AJNR Am J Neuroradiol*, vol. 26, no. 2, pp. 333–340, 2005.

[179] G. Karas, P. Scheltens, S. Rombouts, R. van Schijndel, M. Klein, B. Jones, W. van der Flier, H. Vrenken, and F. Barkhof, "Precuneus atrophy in early-onset Alzheimer's disease: a morphometric structural MRI study," *Neuroradiology*, vol. 49, no. 12, pp. 967–976, 2007.

[180] R. Nabuurs, S. van Rooden, S. van Duijn, M. Versluis, B. Emmer, M. Liem, J. Milles, A. Webb, M. Frosch, S. van Duinen, R. Natte, J. van der Grond, L. van der Weerd, and M. van Buchem, "Detection of cortical changes in Alzheimer's disease at ultra-high field MRI," *Ann Neurol*, 2013, submitted.

[181] G. Frisoni, C. Testa, F. Sabattoli, A. Beltramello, H. Soininen, and M. Laakso, "Structural correlates of early and late onset Alzheimer's disease: voxel based morphometric study," *J Neurol Neurosurg Psychiatry*, vol. 76, no. 1, pp. 112–114, 2005.

[182] S. Sakamoto, K. Ishii, M. Sasaki, K. Hosaka, T. Mori, M. Matsui, N. Hirono, and E. Mori, "Differences in cerebral metabolic impairment between early and late onset types of Alzheimer's disease," *J Neurol Sci*, vol. 200, no. 1, pp. 27–32, 2002.

[183] W. Li, B. Wu, A. Batrachenko, V. Bancroft-Wu, R. A. Morey, V. Shashi, C. Langkammer, M. D. De Bellis, S. Ropele, A. W. Song, and C. Liu, "Differential developmental trajectories of magnetic susceptibility in human brain gray and white matter over the lifespan." *Hum Brain Mapp*, vol. 35, no. 6, pp. 2698–2713, 2014.

[184] S. Yang, W. Lu, D.-S. Zhou, and Y. Tang, "Enriched environment and white matter in aging brain," *Anat Rec (Hoboken)*, vol. 295, no. 9, pp. 1406–1414, 2012.

[185] J. H. Duyn, "Study of brain anatomy with high-field MRI: recent progress," *Magn Reson Imaging*, vol. 28, no. 8, pp. 1210–1215, 2010.

[186] E. Fornari, P. Maeder, R. Meuli, J. Ghika, and M. G. Knyazeva, "Demyelination of superficial white matter in early Alzheimer's disease: a magnetization transfer imaging study," *Neurobiol Aging*, vol. 33, no. 2, pp. 428.e7–428.e19, 2012.

[187] L. Svennerholm and C. G. Gottfries, "Membrane lipids, selectively diminished in Alzheimer brains, suggest synapse loss as a primary event in early-onset form (type I) and demyelination in late-onset form (type II)," *J Neurochem*, vol. 62, no. 3, pp. 1039–1047, 1994.

[188] P. Aljabar, K. Bhatia, M. Murgasova, J. Hajnal, J. Boardman, L. Srinivasan, M. Rutherford, L. Dyet, A. Edwards, and D. Rueckert, "Assessment of brain growth in early childhood using deformation-based morphometry," *Neuroimage*, vol. 39, no. 1, pp. 348–358, 2008.

[189] D. S. Marcus, A. F. Fotenos, J. G. Csernansky, J. C. Morris, and R. L. Buckner, "Open access series of imaging studies (OASIS): longitudinal MRI data in nondemented and demented older adults," *J Cogn Neurosci*, vol. 22, no. 12, pp. 2677–2684, 2010.

[190] D. L. Collins, A. P. Zijdenbos, V. Kollokian, J. G. Sled, N. J. Kabani, C. J. Holmes, and A. C. Evans, "Design and construction of a realistic digital brain phantom," *IEEE Trans Med Imaging*, vol. 17, no. 3, pp. 463–468, 1998.

[191] A. Rauscher, M. Barth, K.-H. Herrmann, S. Witoszynskyj, A. Deistung, and J. R. Reichenbach, "Improved elimination of phase effects from background field inhomogeneities for susceptibility weighted imaging at high magnetic field strengths," *Magn Reson Imaging*, vol. 26, no. 8, pp. 1145–1151, 2008.

[192] F. Schweser, A. Deistung, B. W. Lehr, and J. R. Reichenbach, "Quantitative imaging of intrinsic magnetic tissue properties using MRI signal phase: an approach to in vivo brain iron metabolism?" *Neuroimage*, vol. 54, no. 4, pp. 2789–2807, 2011.

[193] M. Jenkinson, "Fast, automated, N-dimensional phase-unwrapping algorithm," *Magn Reson Med*, vol. 49, no. 1, pp. 193–197, 2003.

[194] M. Pievani, M. Bocchetta, M. Boccardi, E. Cavedo, M. Bonetti, P. M. Thompson, and G. B. Frisoni, "Striatal morphology in early-onset and late-onset Alzheimer's disease: a preliminary study," *Neurobiol Aging*, vol. 34, no. 7, pp. 1728–1739, 2013.

[195] J. P. Lerch, J. C. Pruessner, A. Zijdenbos, H. Hampel, S. J. Teipel, and A. C. Evans, "Focal decline of cortical thickness in Alzheimer's disease identified by computational neuroanatomy," *Cereb Cortex*, vol. 15, no. 7, pp. 995–1001, 2005.

[196] S. M. LeVine, "Iron deposits in multiple sclerosis and Alzheimer's disease brains," *Brain Res*, vol. 760, no. 1-2, pp. 298–303, 1997.

Publications

Journal articles

N. T. Doan, S. J. A. van den Bogaard, E. M. Dumas, A. G. Webb, M. A. van Buchem, R. A. C. Roos, J. van der Grond, J. H. C. Reiber, and J. Milles, "Texture analysis of ultrahigh field T_2^*-weighted MR images of the brain: application to Huntington's disease," *Journal of Magnetic Resonance Imaging*, vol. 39, no. 3, pp. 633–640, 2014

N. T. Doan, S. van Rooden, M. J. Versluis, A. G. Webb, J. van der Grond, M. A. van Buchem, J. H. C. Reiber, and J. Milles, "Combined magnitude and phase-based segmentation of the cerebral cortex in 7T MR images of the elderly," *Journal of Magnetic Resonance Imaging*, vol. 36, no. 1, pp. 99–109, 2012.

N. T. Doan, S. van Rooden, M. J. Versluis, M. Buijs, A. G. Webb, J. van der Grond, M. A. van Buchem, J. H. C. Reiber, and J. Milles, "Group-wise cortical feature analysis using high field T_2^*-weighted MR images highlights local differences between young and elderly healthy subjects," *Submitted*

S. van Rooden[*], **N. T. Doan**[*], M. J. Versluis, J. D. C. Goos, A. G. Webb, A. M. Oleksik, W. M. van der Flier, P. Scheltens, A. W. E. Weverling – Rynsburger, F. Barkhof, G. J. Blauw, J. H. C. Reiber, M. A. van Buchem, J. Milles, and J. van der Grond, "Cortical analysis using 7T MR phase images reveals regional differences between early and late onset Alzheimer's disease," *Submitted*, [*] shared first authorship

Conference proceedings

N. T. Doan, B. van Lew, B. P. F. Lelieveldt, M. A. Van Buchem, J. H. C. Reiber, and J. Milles, "Deformation texture-based features for classification in Alzheimer's disease," in *Proc. SPIE 8669, Medical Imaging 2013: Image Processing*, 866927.

O. Soldea, **N. T. Doan**, A. Webb, M. Van Buchem, J. Milles, and R. Jasinschi, "Simultaneous brain structures segmentation combining shape and pose forces," in *Proc. Multimodal Brain Image Analysis 2011*, 143–151.

N. T. Doan, M. J. Versluis, S. van Rooden, J. van der Grond, A. Webb, M. A. van Buchem, J. H. C. Reiber, and J. Milles, "Combined magnitude and phase-based segmentation of the cerebral cortex in 7T MR images of the elderly," in *Proc. ASCI Conference 2010*.

N. T. Doan, J. Orban de Xivry, and B. Macq, "Effect of inter-subject variation on the accuracy of atlas-based segmentation applied to human brain structures," in *Proc. SPIE 7623, Medical Imaging 2010: Image Processing*, 76231S

Abstracts and presentations

S. van Rooden, **N. T. Doan**, M. J. Versluis, J. D. C. Goos, A. G. Webb, A. M. Oleksik, W. M. van der Flier, P. Scheltens, A. W. E. Weverling – Rynsburger, F. Barkhof, G. J. Blauw, J. H. C. Reiber, M. A. van Buchem, J. Milles, and J. van der Grond, "7T T_2^*-weighted MRI reveals cortical phase differences between early- and late- onset AD," *Alzheimer's Association International Conference*, Copenhagen, Denmark, 2014

M. Buijs, **N. T. Doan**, S. van Rooden, M. J. Versluis, J. Milles, J. van der Grond, and M. A. van Buchem, "Cortical phase shifts in healthy aging at 7 Tesla," *International Society for Magnetic Resonance in Medicine Annual Meeting*, Milan, Italy, 2014

N. T. Doan, S. van Rooden, M. J. Versluis, A. G. Webb, J. van der Grond, M. A. Van Buchem, J. H. C. Reiber, and J. Milles, "Quantitative comparison of the informational content of T_2^*-weighted magnitude, phase and SWI 7T MR data by means of texture analysis of the cortical ribbon in elderly subjects," *International Society for Magnetic Resonance in Medicine Annual Meeting*, Melbourne, Australia, 2012.

N. T. Doan, M. J. Versluis, S. van Rooden, J. van der Grond, A. G. Webb, and M. A. van Buchem, "Automated phase-based segmentation of the cerebral cortex in 7T MR images of the elderly," *International Society for Magnetic Resonance in Medicine Annual Meeting*, Stockholm, Sweden, 2010.

Acknowledgements

In 2009, I joined the Division of Image Processing (LKEB), Leiden University Medical Center (LUMC), Leiden, to pursuit my PhD in brain image analysis. Looking back over the last few years, I believe it was one of the best decisions that I have made, thanks to the wonderful team that I have had the privilege to be a part of and the stimulating environment that I have been exposed to. I would like to thank all of my co-authors and colleagues for their invaluable help with my work at LUMC as well as my stay in the Netherlands.

First and foremost, I would like to express my sincere thanks to my two promotors, Prof. Boudewijn P. F. Lelieveldt and Prof. Mark A. van Buchem, for their continued support and thorough supervision. Boudewijn, thank you for convincing me that I should have my thesis ready for submission before the "big event" of my life, and for helping me achieve that goal. Mark, I am grateful to you for giving me the chance to work on the fascinating 7 Tesla MR data and for the motivating discussions we had.

I would like to further express my deep gratitude to Prof. Johan H. C. Reiber for the opportunity to do a PhD at LKEB and for his supervision in the first half of my PhD period. Hans, to me, the energy and dedication you have for research and development have always been admirable.

Julien, I am deeply thankful for the opportunity to work closely with you during my PhD. As my daily supervisor, you gave me freedom in my research, yet providing me with timely guidance to keep me on track. Your continued encouragement has helped me remain motivated, and your swift response with great sense of responsibility to project-related matters has helped me go through difficult phases. From you I learned to be determined in finishing what I started. Discussion with you has not only been fruitful but also enjoyable, thanks to your openness and sense of humour. Beyond PhD research projects, you have also given me great support and advices in my career development. Thank you!

My roommates in Terminaalzaal, Ronald, Qian, Baldur, Paulien, Luca, Ece, thank you for creating such a charming and open atmosphere in our office, where share, care and help are among the dominating features. You have been so kind and cheerful to me. I appreciate all the chats, laughs, cookies, coffee, etc., which have made work a lot more fun.

Baldur, to me, you are not only a wonderful colleague but also a trustworthy and caring friend. Thank you for your great work in running the extensive image registration jobs. You have also helped me out with numerous computer-related problems and tons of non-work related issues, for which I am forever grateful. I am glad that you agreed to be my paranymph. Zhuo, I am happy to be assisted by the NIP crew in my defense, thank you for kindly agreeing to be my other paranymph. Martijn, we did not have the chance to work on the same project; nevertheless, thank you for the constructive discussions we had on my 7 Tesla work. Michèle, thanks for having done a great job in IT support. Talking with you was so much fun. Shengnan, Shan, Paulien, Oleh, Mohammed, Walid, Changgong, Jasper, Yuchuan, Marius, Jos, Rob, thank you for the enthusiasm and spirits that you brought to the LKEB football team. I think we had demonstrated that, in addition

to doing good image processing research, team sporting is yet another competence of LKEB. Vikas, thank you for kindly sharing your experiences on thesis related subjects. I would also like to thank Erna, Bertie, and Anna-Carien for the thoughtful help with the administration. To the rest of LKEB, I feel honoured to be in the same group with you, thank you!

During my PhD research, I have had the opportunity to collaborate with brilliant researchers from the CJ Gorter Center for High-field MRI, Radiology Department and Neurology Department at LUMC. I would like to express my sincere thanks to all of them, without whom the work presented in this thesis would not have been possible. Sanneke, it has been my great pleasure to work with you in several projects. I appreciate the effort you put in data collection, which is certainly a prerequisite to our analysis projects. Thank you very much, Andrew, Maarten, and Jeroen for the insightful suggestions as well as the constructive and critical comments on my work. Mathijs, thank you for the nice collaboration on the aging data. Helpful discussions with Louis and Thijs are gratefully acknowledged. Furthermore, I would like to thank Eve, Simon and Prof. Roos for the fruitful collaboration on the Huntington's disease work. My gratitude is further extended to Radu (Philips Healthcare) and Octavian for the nice collaboration during my first year.

Special thanks to all of my friends in Netherlands who have made my PhD stay an enjoyable and unforgettable experience. Thuy and Stephan, thank you for the warm and helping hands during my transition from Leiden to Oslo. Dawn, Thuy and Nhung, Dai, Thao and Ronald, thank you for your company and the fun we have had together over the last few years. Thanks to many of my Vietnamese friends in Delft for the joyful activities. Particular thanks go to members of the Vietnamese student football team in Delft and the football team at Leiden University sport centre.

I would like to express my deepest gratitude to my parents, whose love has been the strongest foundation of my academic endeavours. My heartfelt thanks go to my beloved sister and other family members for their persistent encouragement.

Bao Nam, my life has turned to a new exciting chapter since you were born, and I enjoy every bit of it.

Finally, I am greatly indebted to my wife, who offered me to take away considerable family time for my PhD work. Phuong Anh, I feel blessed to have you beside me. Thank you for your unconditional support and your patience. Your love, care, and dedication have been crucial factors to the completion of this work.

Curriculum Vitae

Nhat Trung Doan was born on the 17th of August 1983 in Tien Giang, Vietnam. He received his bachelor degree from the Faculty of Electrical and Electronics Engineering, Ho Chi Minh University of Technology (Vietnam) in 2006. From 2006 to 2007, he worked as a teaching assistant at the same faculty. Subsequently, he followed the European Master of Science in Research on Information and Communication Technologies program with an Erasmus Mundus grant: first year at Universitat Politècnica de Catalunya (Spain), second year at Université Catholique de Louvain (Belgium), and graduated with high distinction. In 2009, Nhat Trung Doan joined the Division of Image Processing, Leiden University Medical Center (the Netherlands) as a PhD student to work on quantitative analysis of ultrahigh field MR images.

He is currently working as a postdoctoral researcher at the Norwegian Center for Mental Disorders Research (NORMENT), Faculty of Medicine, University of Oslo, Norway.